Università degli Studi della Basilicata

International Ph.D. in

"Applied Biology and Environmental Safeguard,
curriculum Geo-Systems, Geo-resources and Environmental Safeguard"
at the Sciences Department of the University of Basilicata

"Crustal deformations and fluid geochemistry: Application of new approaches in some study areas of the Apennines"

GEO/08
GEOCHEMISTRY AND
VOLCANOLOGY

Coordinator

Prof. ssa **PATRIZIA FALABELLA**

Ph.D. candidate

Dott. **DARIO BUTTITTA**

Supervisors

Prof. **MICHELE PATERNOSTER**

Dott. **ANTONIO CARACAUSI**

Cycle XXXV

To my daughter
Gioia Maria

In life, one must never resign oneself, surrender to mediocrity, one must cultivate the courage to rebel.
Rita Levi Montalcini

TABLE OF CONTENTS

LIST OF FIGURES OF CHAPTER I

LIST OF TABLES OF CHAPTER I

CHAPTER II: *Analysis of variability helium outputs from the Irpinia Fault Zone, Italy*

LIST OF FIGURES OF CHAPTER II

LIST OF TABLES OF CHAPTER II

CHAPTER III: *Deep fluid degassing from the crust: a model of the gas-rock and water interactions in the Contursi hydrothermal system (southern Italy)*

LIST OF FIGURES OF CHAPTER III

LIST OF TABLES OF CHAPTER III

ACKNOWLEDGEMENTS

This Ph.D. thesis has benefited from the kindness and help of many professors and researchers that I had the pleasure to work with. Among all, I am grateful to Professor Michele Paternoster who strongly supported me during these three years and from whom I learned a lot (from the scientific, organizational and relational point of view), and to Dr. Antonio Caracausi from the INGV-Palermo for introducing me to the geochemical world and in particular noble gas tools, and for to be my co-supervisor.

I am very grateful to Professor Li Ying, for coordinating my activity at Institute of Earthquake Forecasting (IEF) of the China Earthquake Administration (CEA).

Thanks also to Professor Ray Burgess, University of Manchester, and Professor Orlando Vaselli, Università degli studi Firenze, for the kind revision of the manuscript and for their constructive suggestions that greatly improved the quality of the present dissertation.

Finally, my very special thanks go to my wife, Michela, for his mental and technical support during my whole PhD work. For his patience and sympathy, for the loneliness he tolerated during times of being grass widower when I have been on conference or field trip, and last but not least for check the format and the reference list of my thesis.

GENERAL INTRODUCTION

It has been well established in geological, geochemical and both experimental and theoretical investigations that modification of the chemistry of fluids, which are stored or move through the crust, can occur as a consequence of rock deformation and seismo-genetic processes[1–5]. Indeed, variations in the flow of volatiles as well as in the fluid chemistry of fluids and water temperatures released from springs and wells have been recorded at seismic events. Additionally, both rock fracturing and seismicity both show the formation and release of volatiles[5]. A close theoretical and experimental relationship between rock dilatancy and volatile release has also been identified[6]. In this sense, noble gases (e.g., He and Ar), as non-reactive species, are very valid tools for studying the correlations between rock deformation and volatiles in the study of earthquake physics[7]. Moreover, noble gases facilitate the identification of origin of fluids, even when not atmospheric: He isotopes, for example, allow recognition of a mantle origin of fluids even in the absence of any expression of magmatism and volcanism on the surface[8]. Noble gases are known to be powerful tracers of source and if used in association with the geochemistry of major volatiles (CO_2, CH_4) can provide a means to both identify and quantify water-gas interaction processes[9]. Given that these processes can be easily modified by crustal deformation and earthquakes, they can provide useful data for understanding the relationships between fluids and tectonics.

This PhD project is focused on the study of the fluid geochemistry emitted in some tectonically active areas along the Apennines (Italy), where a relationship between fluid degassing and seismicity is recognized[3,10]. In particular, two areas of Apennines, have been studied which differ in their geological and geodynamic setting: the Nirano Mud Volcano Field (NMVF), in the foothills of the Northern Apennines, and Irpinia region in the southern Apennines. The surface manifestations in these areas represent these differences. Indeed, the NMVF is characterized by CH_4 dominated emissions from mud volcanoes, in Irpinia instead, the fluid emissions are dominated by CO_2, which is dissolved in the groundwater or is released as free gas in Mofettes. The two sites are placed at the CO_2–CH_4 geochemical boundary along the Apennine watershed that seems to mark a boundary limit of the emergence of natural CO_2-rich gas vents[11]. There is a distinct division between the CO_2 domain in the peri-Tyrrhenian internal sector and the

CH_4 domain in the foredeep sections. Gas transfer is mainly associated with mud diapirs in the compressed region of the Apennine orogene, where methane-rich mud volcanoes are found. On the contrary, in the inner part of the Apennines where extension has caused the intrusion of several deep fluid sources (mantle and/or magmatic) CO_2 prevails. The enormous amount of CO_2 diffused in the shallower regions of the crust and produced in several stratified layers in the deeper crust dilutes methane in the peri-Tyrrhenian sector[12]. Similar reasoning may be applied to the relative total amount of helium discharged at the surface, which is lower in the Tyrrhenian sector compared to the NE Apennine CH_4-rich vents[11].

This thesis aims to define a model that can explain the origin of fluids in the different areas along the Apennine, the main processes that modify their chemistry in crustal layers and finally the relationships between deformation and fluids geochemistry in Apennines. Therefore, it involves the collection of geochemical data, which must be processed and subsequently integrated with those already collected from previous studies.
The specific targets have been:1) to evaluate the origin of fluids in the two areas; 2) to define the role of aquifers in the transfer of non-atmospheric fluids (mantles and crustal) in relation to crustal deformations and seismicity of the areas; 3) to discuss the geochemical data in relation to the tectonics and seismicity of the area in order to define a model for the transfer of fluids through to the crust and therefore can highlight any relationships between seismicity and fluid transfer and/or variations of water-gas interactions.

Summary of the activities involved for the realisation of the project

The samples taken will be analysed to define 1) the chemical composition of the gaseous mixtures emitted at the surface, 2) Carbon (C_{CO2}, C_{CH4}) and noble gas (He, Ne, Ar) isotopic composition. The analyses were carried out at the laboratories of the Palermo section of the National Institute of Geophysics and Volcanology of the Palermo section (Italy). The abundance ratios of CO_2 or CH_4 and noble gases integrated with the isotopic ratios of noble gases will make it possible to investigate a possible role of the aquifers in modifying the chemistry of the gases. These data provided a fundamental contribution to

the understanding of the relationships between fluids at depth and the seimo-genetic processes[3,13].

The data acquired had been elaborated and discussed in order to figure out a unique scenario of the origin of fluids, how water-gas-rock interactions processes modify the fluid chemistry during their transfer trough the crust and it will allow and understanding of possible variations of the geochemical parameters that are acquired at high frequency. In detail, the collected geochemical data collected was discussed and interpreted on the basis of geological-structural knowledge and seismic data in order to build a model that can explain the migration of fluids through the crust and the role of seismically active faults in the transfer of the fluids themselves. Finally, I try to define and quantify the migration of deep fluids in the areas of investigation so as to assess the depth of the tectonic discontinuities active in fluid transfer and the role of the fluids themselves in relation to the seismicity of the area, thus providing answers to questions still open.

In conclusion, the collected results are used to create a model defining the origin of the fluids emitted, their transfer through the crust, any water-gas-rock interactions and the relationships between fluids and crustal deformations and seismogenic processes. In addition, the collected data and the model were discussed and compared with the data collected within the geological, structural and seismic network created by the INGV in the Apennines in order to improve the knowledge on the deformation processes active in the study areas.

Abstract of chapters

Chapter I addresses the variability of helium degassing in continental regions, its release from rocks and emission into the atmosphere, based on a study of degassing of volatiles in a seismically active region of northern Italy at the Nirano-Regnano mud volcanic system. Helium is carried through the crust by CH_4, which dominates the released gases in the studied region. Carbon and He isotopes unequivocally indicate that crustal-derived fluids dominate these systems. A high-resolution 3-dimensional reconstruction of the gas reservoirs feeding the observed gas emissions at the surface enables an estimate to be made of the amount of He stored in the natural reservoirs. This PhD dissertation demonstrates that the in-situ production of ^4He in the crust and a long-lasting diffusion

through the crust are not the main processes that control He degassing in the region. Furthermore, in this study is demonstrated that micro-fracturing due to the field of stress that generates the local seismicity increases the release of He from the rocks and can sustain the excess of He in the natural reservoirs with respect to the steady-state diffusive degassing. These results prove that (1) the transport of volatiles through the crust can be episodic as function of rock deformation and seismicity and (2) He can be used to highlight changes in the stress field and related earth.

In the chapters II, I discuss the active roles that deep fluids play during the preparatory phases of large earthquakes and, through their chemical signature, that carry information about deep processes within the seismogenic crust. Due to its inertness and isotopic signature, He is a useful tracer for investigating the processes of storage and transfer of fluids through the crust, including those prior to hazardous earthquakes. Here we analyse a 12-year earthquake catalogue from the Irpinia Fault Zone, Italy, to compute the ^4He outputs from the seismogenetic fault zones (from 10^4 to 10^6 mol y-1 with an annual tenfold variability) and are compared with estimates of long-term helium flux.

It has been found that low-magnitude earthquakes (M<4) efficiently contribute to variations of the crustal helium output into the atmosphere which supports the impulsive nature of He degassing in tectonically active continental regions. I conclude that there is a quantitative relationship between crustal helium outputs and the volume of fault zones (damage zone plus fault core), and suggest variations in helium flux may represent a means to gauge the response of changes in the stress field that are related to the nucleation of earthquakes.

Finally, in the chapter III, the research focuses on the Contursi hydrothermal system (southern Irpinia), where both free and dissolved gases are present. The study investigates the features of innate and introduced fluids in the crust as well as the subsurface processes that can alter their geochemical fingerprint during introduction, storage, and any following migration that is necessary for geochemical monitoring of crustal fluid. This study shows how gas-rock-water interaction through simple mixing processes or more complicated secondary outgassing and precipitation processes can affect the geochemical characteristics of a fluid and how these same processes can mask the source of the deep gases (e.g., mantle). Indeed, in their migration through the crust, fluids undergo a series of complex processes and interactions so, by using the relationship between the Total Dissolved Inorganic Carbon (TDIC) and the $\delta^{13}C_{TDIC}$ in the collected groundwater is found that the processes at depth that control the carbon amount and its isotopic

composition in the fluids, to define a regional model of the deep CO_2 degassing and the gas-rock-water interaction processes occurred.

A NOTE ON THESIS STRUCTURE

The principal research Chapters of this thesis have been prepared as scientific papers for publication in three different international journals. The present status of each publication is summarized as follows:

- **Chapters I** has been published as: **Continental degassing of helium in an active tectonic setting (northern Italy): the role of seismicity**.
  Buttitta, D., Caracausi, A., Chiaraluce, L., Favara, R., Gasparo Morticelli, M., & Sulli, A. (2020). In *Scientific Reports*, *10*(1), 162. https://doi.org/10.1038/s41598-019-55678-7
  Author contributions:
  D.B., A.C. and R.F. designed the paper. A.C. collected the gases. D.B. developed all the calculations. D.B., A.C. and L.C. investigated the relationships between the earthquakes magnitudo, rock fracturation and volatiles release. A.S. and M.G.M. provided all the geological information and the 3D reconstruction of the reservoirs. All the authors contributed in elaborating the data and writing the paper.

- **Chapters II** has been published as: **Earthquakes control the impulsive nature of crustal helium degassing to the atmosphere.**
  Caracausi, A., **Buttitta, D.,** Picozzi, M., Paternoster, M., Stabile, A. T. In *Nature Comunication earth & environment.* https://doi.org/10.1038/s43247-022-00549-9

  Author contributions:
  A.C., D.B., M.P. (Matteo Picozzi), conceived the concepts and designed the study. M.P. (Matteo Picozzi) elaborated the geophysical data. A.C. and D.B. elaborated the geochemical data. A.C., D.B., M.P. (Matteo Picozzi), M.P. (Michele Paternoster) and T.A.S. contributed to the interpretation and discussion of the data and provided comments on and input to the manuscript. D.B. made all the pictures and performed the Montecarlo propagation of the data. A.C. wrote the manuscript

with contributions by D.B. and M.P. (Matteo Picozzi). All authors discussed the results and commented on the manuscript at all stages.

- **Chapters II** will be subdued as: **Deep fluid degassing from the crust: a model of the gas-rock-water interactions in the Contursi hydrothermal system (southern Italy)**

  Buttitta, D., Capasso, G., Paternoster, M., Barberio, D. M., Gori, F., Petitta, M., Caracausi, A. In *Geochimica Et Cosmochimica Acta*

  Author contributions:

  D.B., and A.C. designed the paper. D.B., A.C., M. P., D.M.B and F. G. collected the gases. D.B. developed all the model calculations, graphs and images. D. B. wrote the manuscript with contributions by A. C. and M.P. All authors discussed the results and commented on the manuscript at all stages.

REFERENCE

1. Tsunogai, U. & Wakita, H. Precursory chemical changes in ground water: kobe earthquake, Japan. *Science* **269**, 61–63 (1995).
2. Cox, S. F. The application of failure mode diagrams for exploring the roles of fluid pressure and stress states in controlling styles of fracture-controlled permeability enhancement in faults and shear zones. *Geofluids* 217–233 (2010) doi:10.1111/j.1468-8123.2010.00281.x.
3. Miller, S. a. *et al.* Aftershocks driven by a high-pressure CO2 source at depth. *Nature* **427**, 724–727 (2004).
4. Favara, R., Grassa, F., Madonia, P. & Valenza, M. Flow changes and geochemical anomalies in warm and cold springs associated with the 1992-1994 seismic sequence at Pollina, central Sicily, Italy. *Pure Appl. Geophys.* **164**, 2411–2430 (2007).
5. Caracausi, A. & Paternoster, M. Radiogenic helium degassing and rock fracturing: A case study of the southern Apennines active tectonic region. *J. Geophys. Res. [Solid Earth]* **120**, 2200–2211 (2015).
6. Torgersen, T. & O'Donnell, J. The degassing flux from the solid earth: Release by fracturing. *Geophys. Res. Lett.* **18**, 951–954 (1991).
7. Honda, M., Kurita, K., Hamano, Y. & Ozima, M. Experimental studies of He and Ar degassing during rock fracturing. *Earth Planet. Sci. Lett.* **59**, 429–436 (1982).
8. Caracausi, A. *et al.* Active geodynamics of the central Mediterranean Sea: Tensional tectonic evidences in western Sicily from mantle-derived helium. *Geophys. Res. Lett.* **32**, 1–5 (2005).
9. Ballentine, C. J., Schoell, M., Coleman, D. & Cain, B. A. 300-Myr-old magmatic CO2 in natural gas reservoirs of the west Texas Permian basin. *Nature* **409**, 327–331 (2001).
10. Chiodini, G. *et al.* Carbon dioxide Earth degassing and seismogenesis in central and southern Italy. *Geophys. Res. Lett.* **31**, (2004).
11. Minissale, A., Magro, G., Martinelli, G., Vaselli, O. & Tassi, G. F. Fluid geochemical transect in the Northern Apennines (central-northern Italy): Fluid genesis and migration and tectonic implications. *Tectonophysics* **319**, 199–222 (2000).

12. Minissale, A., Evans, W. C., Magro, G. & Vaselli, O. Multiple source components in gas manifestations from north-central Italy. *Chem. Geol.* **142**, 175–192 (1997).
13. Chiarabba, C. & Chiodini, G. Continental delamination and mantle dynamics drive topography, extension and fluid discharge in the Apennines. *Geology* **41**, 715–718 (2013).

CHAPTER I

Helium degassing and the storage in a seismically active region of northern Italy

I.1 INTRODUCTION CHAPTERE I

Large-scale vertical transport of fluids through the continental crust is not always dominated by steady-state diffusion processes but it can be also advective and episodic [1–4]. It has been recognized that in continental regions volatiles degassing mainly occurs in areas characterized by extensional tectonics and often coincides with seismically active zones [5]. This correspondence has been related to the enhanced permeability of the extensional tectonic discontinuities [6]. However, it has been also observed that variations of the volatiles degassing rate are earthquake-related, and are frequently post-seismic [7–9]. Thus, fluid geochemistry provides evidences of the episodic large-scale transport of volatiles. Even if the flux of the major natural gases (i.e., CO_2) towards the atmosphere is measured at the surface it is difficult to constrain the processes controlling its variability because fluids are often reactive (e.g. water-gas-rock interaction) and several processes work concomitantly during the fluid transfer through the crust [10]. Therefore, in order to figure out the relationships between fluids and earthquake generation processes, at the base of a possible modern earthquake forecast approach, it is fundamental to unravel the processes causing and regulating the fluids flux and chemistry. Because of their chemical properties, noble gases contribute to trace the degassing history of the Earth and the evolution of the atmosphere [11–15]. Furthermore, for investigating the mechanism controlling the transport of fluids in continental region, He, the lightest noble gas, is largely used because its sources (air, crust and mantle) are well resolvable by the use of the isotopic ratio ($^3He/^4He$) [14]. In fact, He is characterized by two isotopes: ^3He, which is a primordial component and it is mainly stored in the mantle, and ^4He that is continuously produced by the U and Th decay, so its amount stored into minerals and rocks progressively increases over geological time. Melting and volatiles release from magma are the main processes that control He outgassing from the mantle. In contrast, degassing of He produced in the crust occurs under different conditions mainly consisting of two stages acting at different scales: (a) the release of the volatiles from the mineral/rocks; (b)

their transport towards the surface [13]. It is recognized that crustal fluids are dominated by ^{4}He, on the contrary, mantle-derived fluids show an excess of ^{3}He (MORB mantle $^{3}He/^{4}He$ is 8 ± 1 Ra, where Ra is the isotopic ratio in atmosphere, $1.382 \pm 0.005 \cdot 10^{-6}$) [16,17] with respect to crustal-derived fluids. He is also found in considerable quantities in some natural-gas reservoirs, where it can remain stored for millions of years [18,19]. The continental ^{4}He degassing shows spatial and temporal variability at regional scale [1], so it is an efficient tool for evaluating the role of tectonics in enhancing the crustal scale mass transport and to decipher the mechanisms of the transfer of volatiles [1,20–23]. Changes of physical properties of rocks can modify the release and transfer of volatiles through the crust [24]. For instance, rock deformation produces new (micro) fractures enhancing the release of the trapped volatiles (e.g., He) and as a consequence the fraction of volatiles released from the rocks during deformation, increases as the rock volume changes (dilatancy processes).

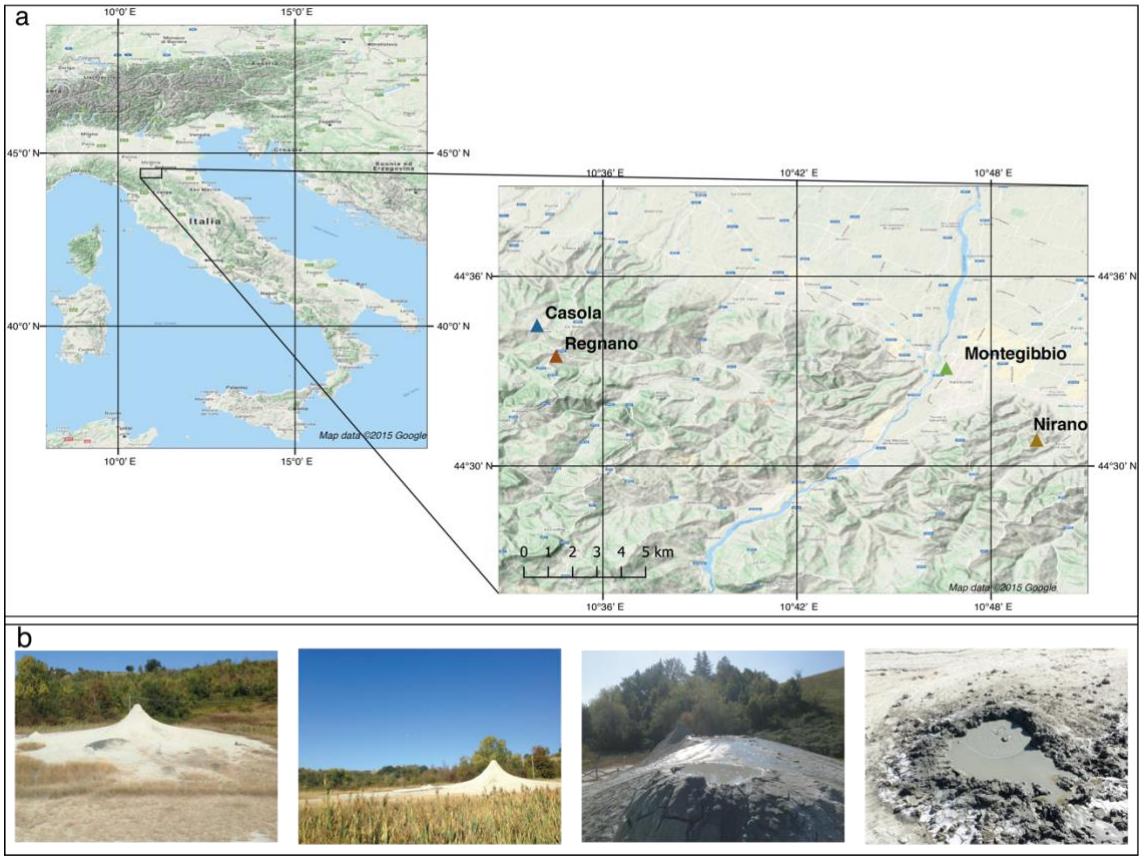

Figure I.1: Study area. (**a**) Geographical framework with sampled sites. (**b**) Some photos of Nirano and Regnano mud volcanoes during the 2018 sample campaign.

However, even if some experimental studies show the existence of a direct link between rock deformation/fracturing and the release of He [25,26], there are only a few examples of

applications in natural systems [21,27,28]. In this study, we investigated the origin and processes controlling the transfer of He through the crust in a seismically active region of the Northern Apennines (Fig. I.1), to establish the possible contribution of tectonic activity in enhancing the release of volatiles accumulated in the rock over time and more specifically, how earthquake occurrence may contribute to episodic volatiles degassing. To this end we collected fluids from mud volcanoes (Fig. I.1a, b) and we analyzed their chemical and isotopic composition (He, $\delta^{13}C$-CO_2, $\delta^{13}C$-CH_4, $\delta^{2}H$-CH_4) to figure out the origin of the outgassing volatiles and the process controlling the crustal degassing. Once verified that the volatiles comes from deep natural reservoirs, we reconstructed the reservoirs volume to estimate the total amount of He stored in these natural traps. The balance between input and output of He in the reservoirs enable us to unravel the processes that control the crustal degassing from He production until its transfer towards the surface, giving also insights to the role and modality of tectonic and seismic behaviour in the vertical transfer of fluids (diffusive vs. advective and episodic).

I.2 METHODS

I.2.1 Geological setting

The study area is characterized by the presence of two main active mud volcanos systems (Nirano and Regnano, Figure I.1 and I.2) that are located along the foothills of the Apennines on small anticlinal structures (22 km long). The presence of these structures at the top of anticlines is common because these are the structural conditions for the storage of fluids [29]. The study area develops in the external part of the NE verging Northern Apennines. It is bounded NE-wards by the Pede-Apennine thrust that separates the exposed Apennine foothills, to the southwest, from the buried chain, formed by SW dipping blind thrusts and folds, exhibiting an overall arcuate shape beneath the Po plain deposits, to the northeast. The Northern Apennines fold and thrust belt (NAFTB) formed by the deformation of the Adria continental margin since the Cretaceous. The early phase of convergence led to the subduction of the European plate below the Adria plate and the an accretionary prism resulted from the decollement of the Ligurian oceanic Units. From the Middle Eocene a change in the subduction polarity and vergence, with Adria becoming the lower plate, produced the tectonic overlapping of the accretionary prism above the Miocene siliciclastic foredeep successions (Marnoso Arenacea) deposited on

the Adria plate. The thick syntectonic sedimentary wedges developed up to the Pliocene-Quaternary, showing a maximum thickness of 7–8 km. The retreating Adria subduction

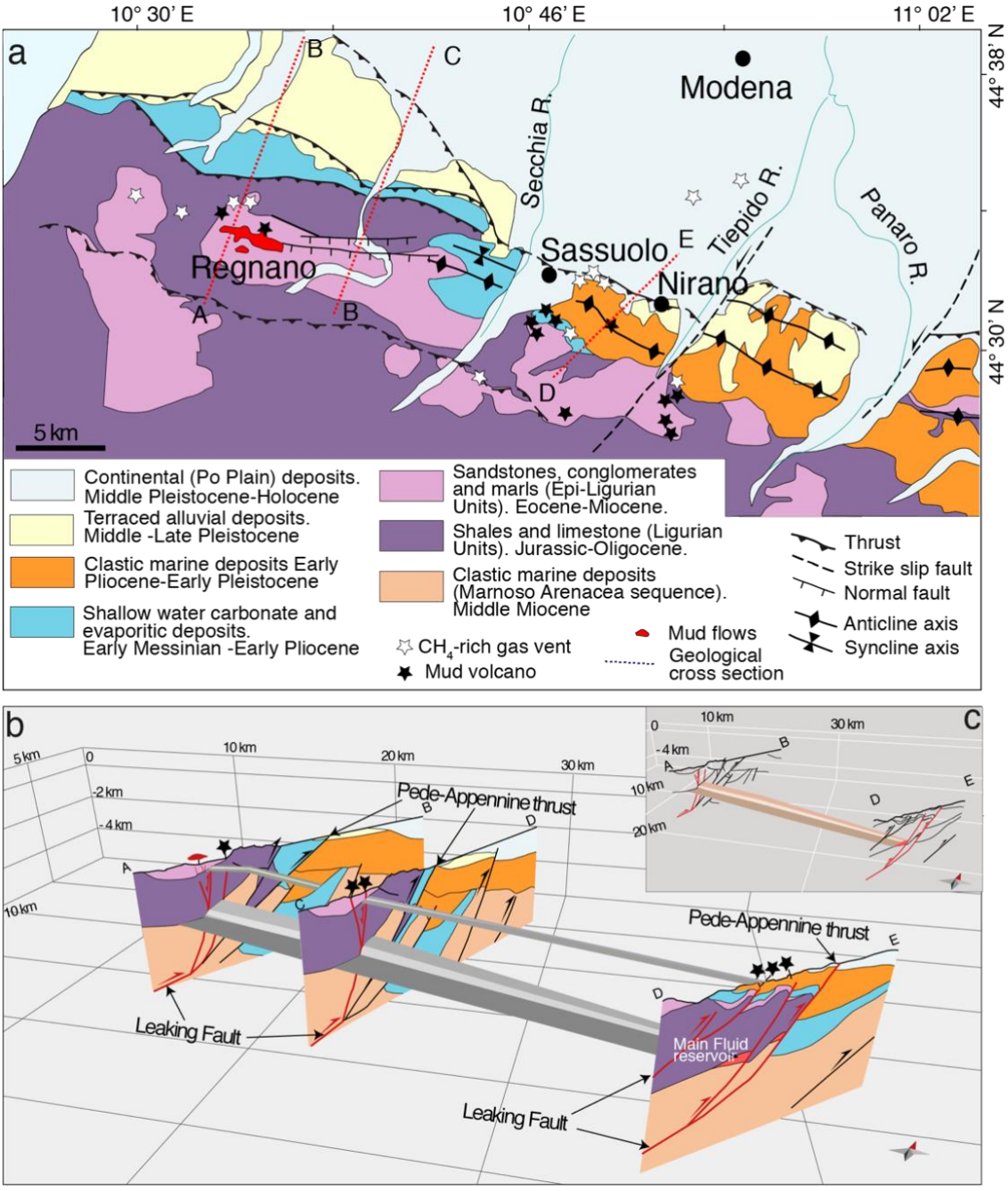

Figure I.2: A general overview of the area with the geological units of the zone of interest (a) a view of the shallow and deep reservoirs by reconstruction carried out with Move 2015.1 software (b) deep reservoir and the system of faults that crosses it (c).

led to the opening of the Ligurian-Provençal and Tyrrhenian back-arc basins. The foredeep deposits were progressively incorporated into the orogenic belt, forming structural highs, which currently form the hydrocarbon traps in the subsurface of the

Northern Apennines and Po Plain. Furthermore, satellite basins atop the Ligurian Units were filled during their emplacement by the Eocene-Pliocene Epiligurian successions. The Livorno-Sillaro Lineament separates the outcrop region of the Ligurian and Epiligurian units to the NW, from the Marnoso Arenacea area to the SE.

The main orogenetic phase of this sector of the Northern Apennines took place between the Oligocene and early Miocene, but lasted until the Messinian. During the Quaternary, the reactivation of lateral ramps of the Miocene-Pliocene thrusts caused fluid migration and accumulation. Most of the Apennine foothills are affected by recent tectonic activity. Earthquake fault plane solutions coupled with analyses of geomorphic traces of recent faulting and deformation along the Pede-Apennine margin suggest that both frontal thrusts and lateral thrust ramps are potentially seismogenic. Along the mountain front, the activity of deep thrusts deforms the whole belt, and its cover up to the Holocene continental deposits. Post-orogenic W-E high-angle normal faults, due to extensional stress field affecting shallow sequences, are the main pathways for the upward fluid migration and the formation of mud volcanoes at the surface, among which the Regnano and Nirano mud volcano fields, located meanly 5 km to the SW of the emergent NNE-verging Late Quaternary Pede-Apennine thrust (Fig. I.1). The Nirano mud volcano field develops in correspondence of a ramp anticline of Langhian to lower Pleistocene deposits. Geochemical analyses show that the greater fraction of the expelled fluids consists of formation water and methane generated in the Marnoso Arenacea sequence and are generally controlled by reverse faults, ramp anticline geometries, and associated fracture zones. Conversely, mud volcanism at Regnano can be related to SSW dipping normal faults developed on the hanging wall of the Pede-Apennine thrust, and rooted in the Marnoso Arenacea, which represent the main source layer of hydrocarbons. Fracture zone associated with the folding are expected to channel fluids to the Nirano field from a shallow mud reservoir located within the anticline core, below the lithological boundary between the impermeable clays (Argille Azzurre Formation) and the underlying more permeable sedimentary units, where the mud may fill the fracture network and achieve overpressuring. Instead, mud extrusion at Regnano field is directly controlled by a fault conduit funnelling the overpressured mud. Despite mud volcanism in Nirano and Regnano fields being controlled by different strain mechanisms, it can be considered as fed by a more or less continuous main reservoir settled in the anticline core developed in the hanging wall of the Pede-Apennine thrust (Fig. I.1). Here it is active the outgassing

methane-rich volatiles from pools and seepage in the two mud volcanoes systems since historical times [30]. Several geological studies have recognized the presence of two-layered fluid reservoirs at depth feeding the gaseous emissions from the Nirano and Regnano systems and the role of the tectonic discontinuities that work as a network of pathways through which fluids mainly migrate vertically towards the surface [29].

I.2.2 Reservoirs and tectonic structure reconstruction

In order to evaluate the volume of the reservoirs feeding the mud volcanoes we reconstructed a 3D geological model of the area between the Regnano and Nirano mud volcanoes systems (Fig. I.2b), using 2D geological cross sections from previous investigations [29–31], and processed with the software Move 2015.1 (Fig. I.2). After geo-referencing two NNE-SSW-oriented geological cross sections (Fig. I.2b) top and bottom lines of the reservoir and the faults bordering it have been preliminarily depicted; afterwards we generated the surfaces using "create surface from line-Spline Curve method" tool. In the next step, we created the volume between the top and bottom surfaces using "Create TetraVolume Between Horizons" tool and then calculated the value. The reconstructed 3D geological model highlighted the existence of two main reservoirs (Fig. I.2b). A deep one about 300-500 m thick that is located at a depth-interval of 2000-2700 m of a ramp anticline with axis of 22 to 39 km, between the Regnano and Nirano areas, with a wavelength between 9 and 13 km. It is hosted into Miocene terrigenous rocks (Marnoso-Arenacea formation) characterized by 15% of porosity. The reconstructed volume is 9.49 km^3. The geological setting of the shallow reservoir, placed in the Regnano area, is more heterogeneous. It is constituted by Jurassic-Paleogene limestones pertaining to the Liguridi unit sealed upwards and laterally by Paleogene marls (Ranzano formation) with stratigraphic and tectonic contacts, respectively. The fault confining laterally the shallow reservoir is the same geological structure affecting the deeper reservoir (Fig. I.2). In the Nirano sector, the shallow reservoir is made up of Miocene sands of the Epi-Liguride units sealed upwards by Plio-Pleistocene blue clays. In this case, the geological trap is the culmination of a ramp-anticline in the Ligurian units. The reconstructed volume of the shallow reservoir is 0.27 km^3. The volume of the shallow reservoir is one order of magnitude smaller than the deeper one, allowing us to neglect its role in the model definition. These geological traps are laterally-bordered by tectonic discontinuities, which are well recognized at depth and mapped at the surface [30]. The reconstructed geological

model highlights an extensional kinematic zone of the fault system in the Regnano sector, which could be interpreted as a reactivated system, while it represents a compressional fault (thrust) in the Nirano sector (Fig. I.2c). Moreover, they permit the transfer of fluids from the reservoirs to the surface. Brittle faults are complex volumetric zones composed of a variety of internal structures, such as slip surfaces, fault rock assemblages, and subsidiary deformation structures. The damage zone of a fault, consisting of subsidiary structures through a relatively large volume of rock surrounding the fault core, is a key factor in controlling the rock permeability and fluids flow through the crust. To investigate the control of the tectonic discontinuities to transfer volatiles trough the crust to the reservoirs and later to the surface we computed the damage zone dimension for the faults locally cutting the upper crust. It is fundamental to know the width of these zones to assess the fluid flow towards the surface. In the absence of field structural data for the main faults (such as orientation and spatial distribution of fractures in the different fault zones) [32], the evaluation of the thicknesses of the damage-zones of the faults at local scale is obtained by using the classical evolutionary models of faulting [33–44] and the scale-relationship between width of the damage zone and displacement. Generally, it is difficult to find a linear relationship between the damage zone width and a single parameter, therefore several parameters, such as lithology and associated diagenesis, depth of faulting, tectonic environment, and deformation mechanism, have been taken into account to evaluate its volume. To limit the effects of the different factors, we analyzed previous results relative to normal faults; moreover, we considered only two types of deformation features in the analysed rocks: deformation bands in porous sandstones and fractures in brittle rocks. In summary, the system of faults that crosses the deep reservoir consists of two main fault systems (Figure I.1). The first system mainly involves the geological domains in the area of Nirano, whose length is 300 m at a depth between 2000 and 2300 m, with a lateral extension of about 6300 m, with a possible damage zone between 8 and 20 m (measured on rocks with similar lithology) [32,45]. The second one, which affects the sector of Regnano, is 500 m long and is located at a depth between 2200 and 2700, has a lateral extension of about 8800 m and a possible damage zone between 8 and 20 m (measured on rocks with similar lithology) [32,45].

I.2.3 Analytical procedures

Gas samples were collected in Pyrex bottles with vacuum valves at both ends, taking care to prevent air contamination, and these were analysed in 10 days from their sampling. Gas samples have been analysed in the laboratories of the Istituto Nazionale di Geofisica e Vulcanologia, sezione di Palermo. The chemical composition of He, H_2, O_2, N_2, CO, CH_4, CO_2 and C_2H_6 has been measured by a Perkin Elmer Clarus 500 gas chromatograph equipped with a 3.5-m Carboxen 1000 column and double detector (hot-wire detector and flame ionization detector), with analytical errors of < 3%. Analytical precision for GC analyses is better than ± 5% for trace gases and ± 10% for alkanes. ^{3}He, ^{4}He and ^{20}Ne and the $^{4}He/^{20}Ne$ ratios were determined by separately admitting He and Ne into a split flight tube mass spectrometer (GVI-Helix SFT), after standard purification procedures [46]. $^{3}He/^{4}He$ ratio is expressed as R/Ra (being R the $^{3}He/^{4}He$ ratio of the sample, and Ra the $^{3}He/^{4}He$ ratio of air, $1.382 \cdot 10^{-6}$). The analytical error is generally below 0.3%. The R/Ra values were corrected for the atmospheric contamination basing on the $^{4}He/^{20}Ne$ ratio [47] and reported as Rc/Ra (Table I.1) [48]. The C isotope composition of CO_2 (expressed as $\delta^{13}C‰$ vs. V-PDB) was determined using a Thermo (Finningan) Delta Plus XP CF-IRMS, connected to a Trace GC gas chromatograph and a Thermo (Finningan) GC/C III interface [48,49]. The gas chromatograph, equipped with a Poraplot-Q column (length 30 m, i.d. 0.32 mm), kept at a constant temperature of 50 °C, uses He as the carrier gas. The analytical uncertainty was ± 0.1‰. Carbon and hydrogen isotopes of CH_4 were carried out on the same equipment. GC III combustion interface was used to produce carbon dioxide from CH_4 [50]. GC-TC interface provides on-line high-temperature methane conversion into hydrogen suitable for isotope analyses. Typical reproducibility (1σ) for $\delta^{13}C\text{-}CH_4$ and $\delta D\text{-}CH_4$ measurements is better than 0.2‰ and 2.5‰ respectively [51].

Site	Lat	Long	O_2 (%)	N_2 (%)	CH_4 (%)	CO_2 (%)	C_2H_6 (ppm)	He (ppm)	^{20}Ne (ppm)	$^4He/^{20}Ne$	(R/Ra)c	Err +/- ($\times10^{-4}$)	$\delta^{13}C$-CO_2	$\delta^{13}C$ - CH_4	$\delta^{13}D$-CH_4	C(tot)/ ^4He ($\times10^4$)
Nirano	N 44°30'49.57"	E 10°49'32.13"	0.01	0.34	98.26	0.54	381	18	0.029	636.47	0.01	1.27	18.61	-47.2	-173	5.4
Nirano 2	N 44°30'46.14"	E 10°49'16.90"	0.05	0.55	98.18	0.53	374	18	0.098	187.02	0.01	1.06	13.77	-46.2	-179	5.4
Regnano	N 44°33'28.75"	E 10°34'33.30"	0.09	0.62	97.74	1.04	1800	24	0.394	59.37	0.01	0.778	18.41	-46.7	-170	4.2
Casola	N 44°34'26.56"	E 10°33'57.94"	0.02	0.56	96.74	0.97	587	20	0.07	354.35	0.01	1.00	16.08	-45.1	-176	4.8
Montegibbio	N 44°30'58.13"	E 10°46'37.14"	bdl	1.27	97.08	0.27	135	37	0.171	215.32	0.01	0.967	n.d.	-46.2	-178	7.9

Table I.1: Chemical and isotopic composition of the venting gases from the mud volcanoes of Nirano and Regnano areas. Sampling Date 29-09-2018.

I.2.4 Gas reserves computations

The classic approach to estimate the gas reserves stored in a natural reservoir (Q) is based on a volumetric method [52] where the computed values of the gases volume are statistically considered the "best-estimate" value [53]. Here we applied this approach to compute the total amount of gas that is stored into the deep and shallow reservoirs (Table I.2). The total gas amount in the reservoir is computed by using the equation [54]:

$$Q = \frac{G.B.V. \cdot Net/Gross \cdot \phi \cdot (1 - S_w - S_o)}{Bg} \qquad \text{(eq. I.1)}$$

where: G.B.V. = Gross Bulk Volume represents the gross volume of mineralized rock (inclusive of any clayey and/ or compact horizons that do not contribute to production) ($9.5 \cdot 10^9$ m^3 and $2.7 \cdot 10^8$ m^3 the deep and the shallow gas reservoirs); Net/Gross = Ratio between the rock thickness that actually contributes to the production and the gross thickness of rock (1 for this work); ϕ= Average porosity of the reservoir (fraction, 15%); Sw = Average water saturation of the "reservoir" (fraction) o Volume fraction of porosity filled with interstitial water [55]; So=Oil saturation (between 0 and 10%); Bg = "Formation Volume Factor" that is used to express the volume of hydrocar- bons originally in place at the "standard" surface conditions, i.e. at a pressure of 1 atm and at a temperature of 20°C. The Sw it is equal to 15%, calculated with Timur 1968 [56]. Where k is the permeability, equal to 80 mD.

$$S_w = \sqrt{\frac{10^4 \cdot \phi^{4.5}}{k}} \qquad \text{(eq. I.2)}$$

The Formation Volume Factor is given by the ratio of the volume of gas to the conditions of the reservoir and the volume of the gas to the standard conditions. Mathematically:

$$Bg = \frac{Vrc}{Vsc} = \frac{Psc \cdot Trc \cdot Zrc}{Prc \cdot Tsc \cdot Zsc} \qquad \text{(eq. I.3)}$$

where, Psc, Tsc, Zsc, represent surface (pressure, temperature and compressibility factor) conditions while, Prc, Trc e Zsc, are the conditions (pressure, temperature and compressibility factor) in the reservoir. The compressibility factor, Z, is calculated by using the approach in Piper and Corredor (1993) [57]. Therefore, the inverse of the

Formation Volume Factor is equal to 1/Bg = 371.19 SCM/ResCM, i.e. 1m^3 of pore volume under the reservoir conditions contains 1/Bg m^3 of gas under standard conditions. Table I.2 shows the total gas amount in the two reservoirs, Q: (1) from $1.66 \cdot 10^{13}$ moles to $1.87 \cdot 10^{13}$ moles for the main reservoir (depth 1850–2600 m) at PrcLitho= 49 MPa, Trc = 327.15 °K and So from 0 to 10% and (2) $2.36 \cdot 10^{10}$ moles for the shallow (secondary) trap (depth 400–1000 m) at d Trc = 295.75 °K, PrcLitho= 4 MPa So = 0.0. The lithostatic pressure were calculated taking into account the mean thicknesses and densities of the crustal layers and the value of g

Calculation of the initial gas in place			
	Main		Secondary
Reservoir Conditions	Trc = 327.15 °K P_{RC}^{Litho}= 48.98 MPa		Trc*= 295.75 °K P_{RC}^{Litho*}= 4 MPa
G.B.V. in m^3	9.49×10^9		2.69×10^8
ϕ	0.15		0.50*
(1-Sw-So)	0.75/0.85		0.50*
1/Bg in SCM/RCM	371.19		42.25
Z	1.165		0.24
	So=0.10	So=0	So=0
Q(SCM)	$3.99 \cdot 10^{11}$	$4.5 \cdot 10^{11}$	$5.68 \cdot 10^{08}$
Q(mol)	$1.66 \cdot 10^{13}$	$1.9 \cdot 10^{13}$	$2.35 \cdot 10^{10}$
$Q4_{He}$ (SCM)	$8.78 \cdot 10^{06}$	$9.9 \cdot 10^{06}$	$1.19 \cdot 10^{04}$
$Q4_{He}$ (mol)	$3.64 \cdot 10^{08}$	$4.1 \cdot 10^{08}$	$4.93 \cdot 10^{05}$

Table I.2: Summary of reservoirs condition and initial gas in place into the traps calculated by volumetric method. * data from Oppo, 2012 [58].

I.2.5 Helium lost by diffusion

The helium lost by diffusion it was calculated using a one-dimensional steady-state diffusion model using the formula in Liu et al. [59]:

$$\int_0^t \frac{D}{Z} \cdot \left(\frac{22.4 \cdot Q \cdot C_t}{G.B.V. \cdot \phi \cdot K_{H_2O}} \frac{P_{NC} \cdot T_{RC}}{T_{NC}} - 4.5\ 10^{-8} \right) \cdot S \cdot dt \qquad \text{(eq. I.4)}$$

where: D is the diffusion coefficient of He ($2 \cdot 10-6$ cm^2/s) [59]; Z is the buried depth of reservoir, the middle point of deeper reservoir in this case (2225 m); Q is the total gas

amount in the reservoir is computed by using the Eq. (I.1); Ct is the ^{4}He concentration at time t in %v; P_{NC} is the normal atmosphere (1 atm); T_{NC} is normal temperature (273 °K); T_{RC} is the reservoir condition temperature (327.15 °K); G.B.V is the gross bulk volume in ($9.49 \cdot 10^{11}$ cm^3); φ s the porosity (%); K_{H2O} is the is Henry's constant calculated from the solubility model of noble gases in the water (approximately 2500) [24].

I.3 RESULTS

In the northern Apennines (Italy) the mud volcanoes are distributed along the external sector of the fold-and-thrust belt (Fig. I.1). This region is considered a reference area to study fluid venting processes in an active fold-and-thrust belt [60] and the fluids geochemistry is used as a potential indicator of impending local earthquakes [61]. The seismicity is concentrated in the crust and at local scale the maximum magnitude is 6.0 (https://emidius.mi.ingv.it). Furthermore, it is recognized that the fluid output from the mud volcanoes increased just after the earthquakes [9,62–64].

Previous investigations highlighted that the gases emitted from the mud volcanoes are CH_4-rich [65] and they are fed by two reservoirs that are strongly different in dimension and vertically separated [29]. At the regional scale, the studied mud volcanoes are localized at the top of the anticlines (Fig. I.1a), particularly in joints perpendicular to the axis of the fold, where the impermeable cover allows pore fluid pressure build-up (close to lithostatic magnitudes) [29]. Mud volcanoes are placed along active normal faults (Fig. I.2a), allowing a vertical migration of CH_4 coming from deep sources (>3–6 km) [66]. In this region mud volcanism can be potentially triggered by fault failure cycles and the overpressured fluids released during faulting [29]. Furthermore, the relatively quiescent but continuous activity of these mud volcanoes could instead reflect a short-lived leakage of overpressured fluids along permeable fractures/faults. Thus, the study sites are optimal examples for investigating the mechanisms of fluid transfer through the crust and the possible relationships between degassing of crustal fluids and rocks deformation and seismicity.

I.3.1 Fluid geochemistry

We collected gas samples from four different mud volcanoes areas (Fig. I.1): Nirano, Montegibbio, Regnano and Casola. Nirano - Montegibbio sites are located 3.5 km apart, while Regnano - Casola only 2.0 km. Hereafter, we named Nirano-Montegibbio sites as

the Nirano system and Regnano-Casola sites as the Regnano system. We analysed the fluids for defining the gas chemistry (He, H_2, O_2, N_2, CO, CH_4, CO_2 and C_2H_6) and the isotopic composition of He ($^3He/^4He$), ^{20}Ne, C of both CH_4 and CO_2 and H of CH_4 (Table I.1).

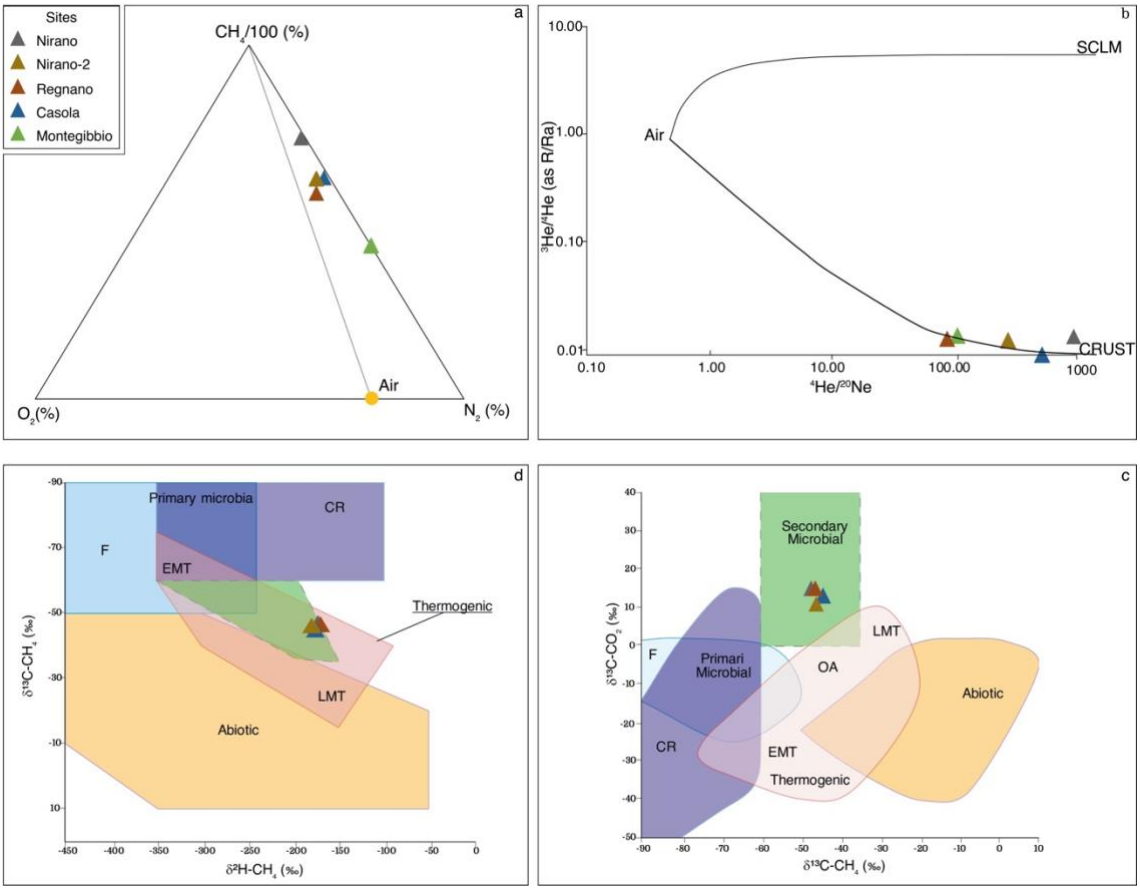

Figure I.3: O_2–N_2–CH_4/100 ternary diagram for the gas samples investigated. All the gases are CH_4-dominated and are not along the mixing line between a pure CH_4 end-member and air showing that the sampled gases are not air-contaminated. (a) A correlation diagram between the $^3He/^4He$ and $^4He/^{20}Ne$ ratios for the gas samples investigated. The whole black lines show the mixing lines between mantle-derived helium and between radiogenic helium with the Air. The mantle end-member is the Sub Continental Lithospheric Mantle (SCLM, 6.1 ± 0.9 Ra) [67]. (b) Genetic diagrams of $\delta^{13}C$-CH_4 versus $\delta^{13}C$-CO_2 (c) and methane genetic diagrams based on δ^2H-CH_4 versus $\delta^{13}C$-CH_4. (d) T – thermogenic, A – abiogenic, CR – CO2 reduction, F – fermentation, OA – oil-associated thermogenic gas, LMT – late mature thermogenic gas, EMT – early mature thermogenic gas, SM- Secondary Microbial. The gaseous hydrocarbons are a mixture of secondary biogenic methane and primary and secondary thermogenic gases. The associated oils show both early and late maturities. These evidences account for different generation and migration steps, depending on burial conditions and deformation time [31].

According to previous investigations[31,68,69] the outgassing fluids from the Nirano and Regnano systems are CH_4 dominated (96.7–98.3%). CO_2 is up to 1.04%, O_2 and N_2 up to

0.09% and 1.27% respectively; He is in traces (up to 23 ppm vol.). The low concentrations of O_2 and N_2 indicate that the collected gases suffer low amount of air contaminations (Fig. I.3a). The He isotopic ratios are 0.01–0.03 Ra, that is the typical range of the crustal radiogenic He (Fig. I.3b). The $^4He/^{20}Ne$ ratios in the collected fluids are from 59.4 to 636.5 and these values are more than 2 order of magnitude higher than the same ratio in air ($^4He/^{20}Ne_{AIR}$ = 0.318) [70] supporting the low atmospheric component in the gases from the Nirano and Regnano systems (Fig. I.3a,b). Hence, the outgassing He from the mud volcanoes systems is dominated by radiogenic ^4He that is produced by U and Th decay in the crust [70]. The C and H isotopic composition of CH_4 is in a good agreement with previous results highlighting the thermogenic nature of CH_4 (Fig. I.3c and Table I.1) [30,31,68]. Here we report the first data of C and H isotopes of CH_4 in gases from Casola and Montegibbio sites, indicating a unique origin of CH_4 emitted from these mud volcanoes systems (Fig. I.3c and Table I.1). The carbon isotopic composition of CO_2 in all the studied fluids is from + 13.8‰ to + 18.6‰ and according to Milkov and Etiope (2018) [69] these values coupled to the isotopic composition of CH_4 indicate that CO_2 is of thermogenic origin (Table I.1 and Fig. I.3c,d). These results are in a good agreement with those from previous investigations [66] that highlighted (1) the thermogenic nature of pristine methane in the deep reservoirs, (2) an origin of CH_4 in crustal layers deeper than the reservoirs (> 3–6 km) and (3) a vertical migration of CH_4 towards the surface. Considering the main component in the collected gases is CH_4 (~98%) and the average $CH_4/^4He$ ratio in the emitted gases is ~46000 we computed the amount of ^4He in the two reservoirs by using the total amount of gases into the reservoirs, between $4.00 \cdot 10^{11}$ and $4.50 \cdot 10^{11}$ standard cubic meter (SCM) for the main reservoir, and $5.68 \cdot 10^8$ SCM for the shallow reservoir (Supplementary Information: gas reserves). Thus, the amount of ^4He in the shallower and deep reservoirs are $4.90 \cdot 10^5$ moles and $3.60 \cdot 10^8$–$4.20 \cdot 10^8$ moles respectively. The amount of ^4He in the shallow reservoir is three orders of magnitude lower that the amount in the deep reservoir (lower than 1% of ^4He amount in the deep reservoir), so it can be considered negligible (Table I.2).

I.3.2 He degassing

There have been many consistent estimates of the flux of ^4He from the continental crust based on calculations of in situ production and steady-state release to the atmosphere by using the U and Th content in rocks, crustal thickness and total release of ^4He. These

calculations yield a crustal degassing flux of ^{4}He of the order 3.3 ± 0.5 ·10^{10} (atoms·m^{-2}·s^{-1}) [1,71,72]. However, experimental works highlighted that the release of volatiles increases in volume of rock in an active stress field, which implies that ^{4}He degassing through the crust can be episodic in active tectonic areas [26,73,74]. Mechanical deformation and rocks failure can break (or crack) mineral grains, causing pervasive micro-fracturing and dilation. Consequently, the rocks can increase porosities from 20% to as high as 400% prior to failure [75], open new micro-fracture surfaces, and eventually cause macroscopic failure and fracture of rocks [76]. These processes lead to a release of volatiles (e.g. He) previously trapped within mineral grains along fracture networks [77,78] and the pore fluids transport these volatiles through the crust. Here we investigate if a steady state degassing is the main process that controlled the ^{4}He flux to the reservoirs below the Regnano and Nirano systems over time.

I.3.3 He degassing: steady-state conditions

The local stratigraphy and tectonic evolution indicates that the age of formation of the anticline hosting the main gas reservoirs below the Regnano and Nirano systems goes from 1.8 to 4.5 Ma. Over a million-year timescale the flux of ^{4}He through the Earth's crust to the atmosphere is comparable to the net in situ production (in steady state condition), in 30–40 km of crustal thickness [79]. In order to assess if the ^{4}He production in the crust and the successive migration to the natural reservoirs feeding the Nirano and Regnano systems can justify the amount of He that is stored in the reservoirs, we used a mass balance approach [59]:

$$^4He = {}^4He_{Initial} + {}^4He_{Insitu} + {}^4He_{Externalflux} - {}^4He_{Leak-d} - {}^4He_{Leak-mv}$$

(eq. I.5)

where ^{4}He represents the amount of radiogenic helium (moles) in the reservoir at time t. It includes three input and two outputs terms. Among the input terms, ^{4}HeInitial is the amount of ^{4}He that is in the reservoir at time t-zero, ^{4}He Insitu the amount of radiogenic ^{4}He produced in the reservoir-rocks volume since its formation (from 1.8 to 4.5 Ma), ^{4}He External flux is the flux from the crust below the reservoirs. ^{4}He Leak− d and ^{4}HeLeak−mv are the two terms of outputs: ^{4}HeLeak−d is the He lost by diffusion from the main reservoir over time and it is from 4.37·10^5 mol to 1.09·10^6 for a t of 1.8 Ma and 4.5 Ma respectively (Methods; gas reserves). It is up to 0.36% of the total volume of He. The

second one, ^{4}HeLeak− mv, is the He leak due to advection, and we assume that is the He emitted from the mud volcanoes. We extrapolated the current He outgassing from mud volcanoes, to the past 10^4 years, in this time we have considered continuous degassing (about 95 mol/y), and the possible paroxysmal activity as follows: “normal” eruption (10 times the continuous, every year) and “strong” eruption (100 times the continuous, once every 30 years) [63,66,80]. The result is that up to $3.8 \cdot 10^7$ mol of He can by lost from mud volcanoes. Nonetheless these two outputs terms are less than about 10% of the amount of He stored in the main reservoir, and therefore, does not entail any change in the conclusions, so it is reasonable to neglect their contribution in Eq. I.5 which means an underestimaion of the He present in the reservoir.

To compute ^{4}HeInsitu and ^{4}HeExternal flux we used literature data for the abundances of U and Th and for crust thickness. Hence, we based our calculations on the U and Th amounts for a Regional Refined Reference Model and the Global Refined Reference Model (Table I.3) [81]. The in-situ production of ^{4}He is computed on the basis of the approach proposed by Zhou and Ballentine [82]:

$$^4He_{Insitu} = \rho \cdot \Lambda \cdot \alpha \cdot (1 - \phi) \cdot V \cdot t \qquad \text{(eq. I.6)}$$

where ρ is the rock density in g/cm^3 (2.21 g/cm^3), ∧ a parameter defining the efficiency of the transfer from the rock matrix into the gas phase, ϕ is the porosity of reservoir (fraction), α the source function of radioactive production of ^{4}He in the rock matrix (mol ^{4}He·grock·year^{-1}), V the volume of the gas reservoir (cm^3) and t the formation time of gas reservoirs (years). Since the process of ^{4}He released from a host mineral is short compared to the geologic age [13] ∧ can be regarded as being equal to 1. α, according to the U and Th decay equations, can be calculated using the following equation [83]:

$$\alpha = 0.2355 \cdot 10^{-12} \cdot U \cdot \left[1 + 0.123 \cdot \left(\frac{Th}{U} - 4\right)\right] \qquad \text{(eq. I.7)}$$

where U and Th represent the concentrations of U and Th in rocks that host the reservoirs and are expressed in ppm. The accumulation rate of the in situ produced ^{4}He of gas reservoirs is expressed as (cm^{3}STP/y):

$$q^{in}_{^4He} = \rho \cdot \alpha \cdot (1 - \phi) \cdot V \qquad \text{(eq. I.8)}$$

The in-situ production of ^{4}He is 0.11 ± 0.02 mol/y and 0.30 ± 0.02 mol/yr (in Regional and Global model respectively).

The external flux of ^{4}He is computed by using the method in Zhou and Ballentine [82]:

$$^4He_{Externalflux} = \frac{q^c{}_{^4He}}{S} \cdot t \quad \text{(eq. I.9)}$$

where S is the gas-bearing area of a reservoir (cm^2), t the gas reservoir formation time (years) and $q^c{}_{^4He}$ the average external crustal ^{4}He flux (mol ^{4}He/cm^2/year). $q^c{}_{^4He}$ can be calculated as:

$$q^c{}_{^4He} = \alpha \cdot \rho \cdot H \qquad \text{(eq. I.10)}$$

where ρ is the average crust density in g/cm^3 (2.80 g/cm^3) [84] and H is the crust thickness in cm (3.2·10^6 cm, Lavecchia et al. 2003) [85].

The external flux of ^{4}He to the two reservoirs is 37.53 ± 12.12 mol/y and 54.54 ± 5.86 mol/y (in Regional and Global model respectively, Fig. I.4).

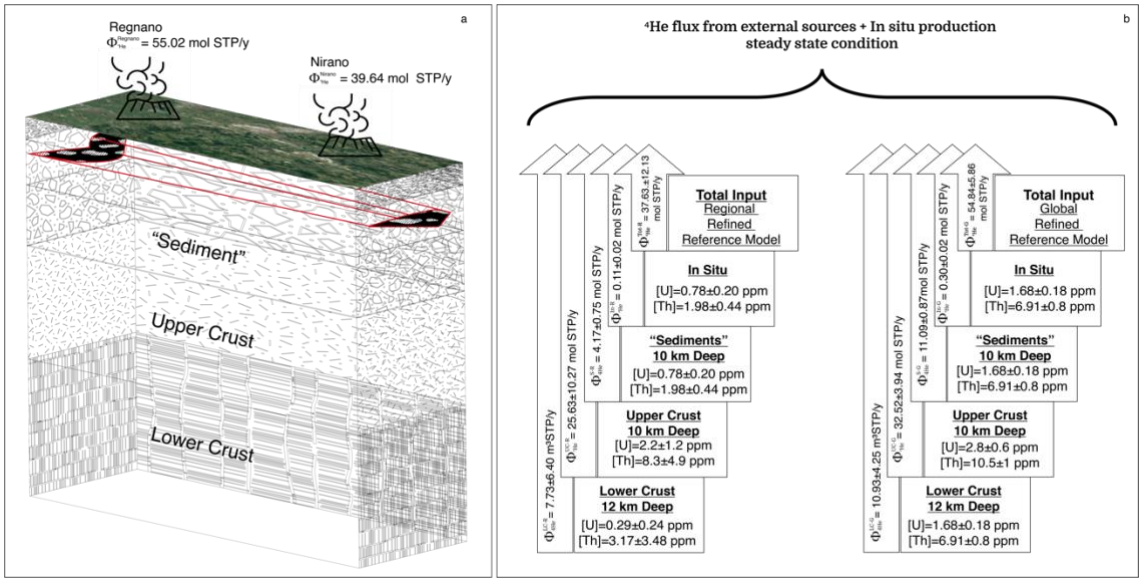

Figure I.4: A simplified model of Nirano-Regnano mud volcanoes system. (**a**) Total input of crustal ^{4}He with concentrations of Uranium and Thorium ([U] and [Th], respectively) in "Sediment", upper and lower crust. Data of [U] and [Th] contents in rocks from Coltorti *et al.* [81]. (**b**) Φ*LC−G* and Φ*LC−R* are the fluxes from the lower crust ^{4}*He* ^{4}*He UC−G UC−R* with [U] and [Th] content relative to the Regional (R) and Global (G) models. Φ^4*He* and Φ^4*He* are the fluxes from the upper crust with [U] and [Th] content relative to the Regional (R) and Global (G) models.

$\Phi S{-}G$ and $S{-}R$ $^4He\Phi^4He$ are the fluxes from the "Sediment" with [U] and [Th] relative to the Regional (R) and Global (G) models. $\Phi In{-}G$ and $\Phi In{-}R$ are the fluxes from *in situ* production with [U] and [Th] content relative to the Regional (R) ^4He ^4He $Tot{-}G$ $Tot{-}R$ and Global (G) models. Φ^4He and Φ^4He are are the total input flow that feeds the reservoir with [U] and [Th] content relative to the Regional (R) and Global (G) models. $\Phi Nirano$ and $\Phi Regnano{-}R$ are the total output flow from the mud volcanoes of Nirano and Regnano.

Considering these values of ^{4}He input in the reservoir, the total amount of ^{4}He that can be accumulated into the trap in a time going from 1.8 and 4.5 Myr, varies from $6.7{\cdot}10^7$ mol to $2.5{\cdot}10^8$ mol, respectively. These values are lower than the amount of He in the reservoir that we computed by using the volumetric method (from $3.64{\cdot}10^8$ mol to $4.12{\cdot}10^8$ mol, Table I.2). So, production of ^{4}He from the whole crust below the main reservoir and its successive transfer by diffusion processes, cannot support the amount of He stored into the reservoirs (Fig. I.5).

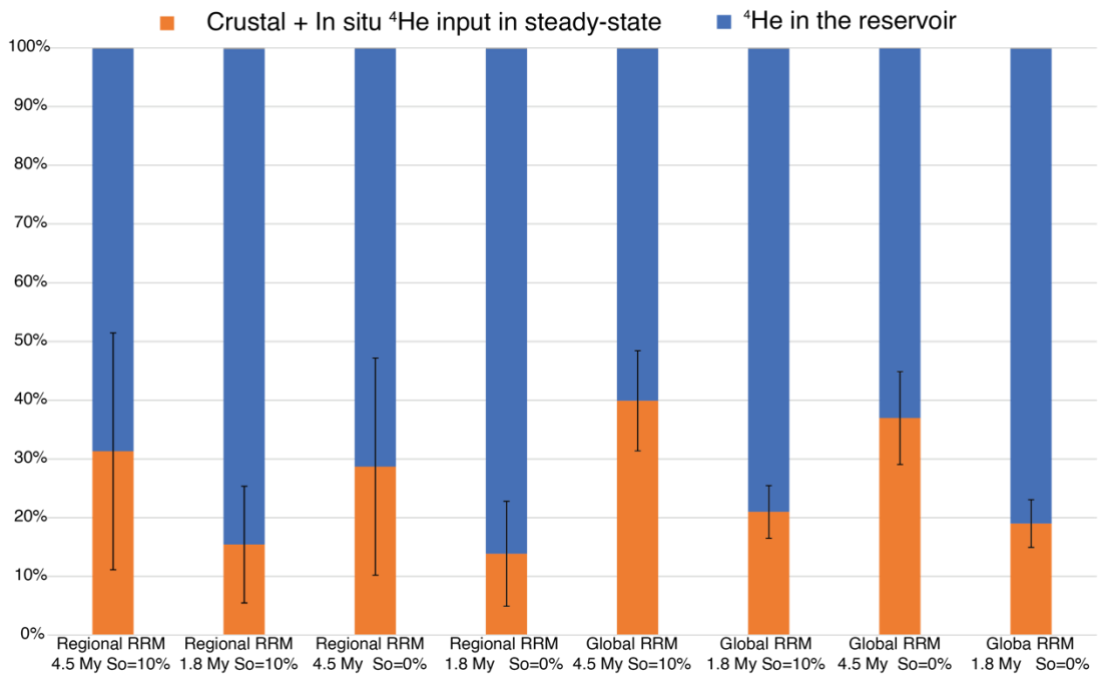

Figure I.5: The production of radiogenic He and its release in stationary state, in the age of the trap (1.8 Ma or 4.5 Ma), represents from 15% to 40% of the helium present in the main reservoir. The error bars shown are 2σ.

If we consider a steady-state diffusion model to explain the excess of ^{4}He in the two reservoirs we need to invoke a volume of ^{4}He-productive crust from 1.5 to 6.2 times larger than that below the trap (~1323 km^3). Considering that previous investigations [65] highlighted that the source of CH_4 is in deep crustal layers (> 3–6 km) and CH_4 vertically migrated towards the natural reservoirs it is reasonable that the processes of volatiles

migration different from the steady-state diffusion occurred below the investigated mud volcanoes systems.

	Thickness (km)	Density (g/cm^3)	RRM-Regional*		RRM-Global*	
			U (ppm)	Th (ppm)	U (ppm)	Th (ppm)
Sediments	10	2.21	0.78±0.20	1.98±0.44	1.68±0.2	6.91±0.8
Upper Crust	10	2.80	2.20±1.20	8.30±4.90	2.70±0.6	10.50±1.0
Lower Crust	12	2.80	0.29±0.24	3.17±3.48	0.60±0.4	3.70±2.4

Table I.3: Regional and Global suite of U and Th concentration distributed in the "Sediments", Upper Crust and Lower Crust. *data from [81].

I.3.4 ^{4}He flux: episodic degassing and active tectonic

The release of volatiles from rocks increases as the effect of dilatancy increases and in regions affected by active tectonics. Therefore, the flux of ^{4}He through the crust should be higher than that in un-deforming areas where it is reasonable to assume that a diffusive steady-state transport system is acting. Our calculations show that ^{4}He in the natural reservoirs is in excess with respect to a steady-state whole crust degassing. As a result, in the main reservoir, there are between $1.2 \cdot 10^8$ and $3.5 \cdot 10^8$ moles in excess of the ^{4}He produced in the crust below the main reservoir plus the $^4He_{Insitu}$.

Considering that the region is tectonically active and two main systems of active faults cross cut the deep reservoir (Fig. I.2c and Methods: Geological setting), here we investigate if micro-fracturing can sustain the excess of ^{4}He in the reservoirs. The release of ^{4}He from rock, which are affected by dilatancy, is from 10 to 10^4 times higher than that in un-deformed rock [26], so the release of ^{4}He from a deforming fault damage zone is significantly higher relative to a tectonically undisturbed rock volume (Figs. I.6).

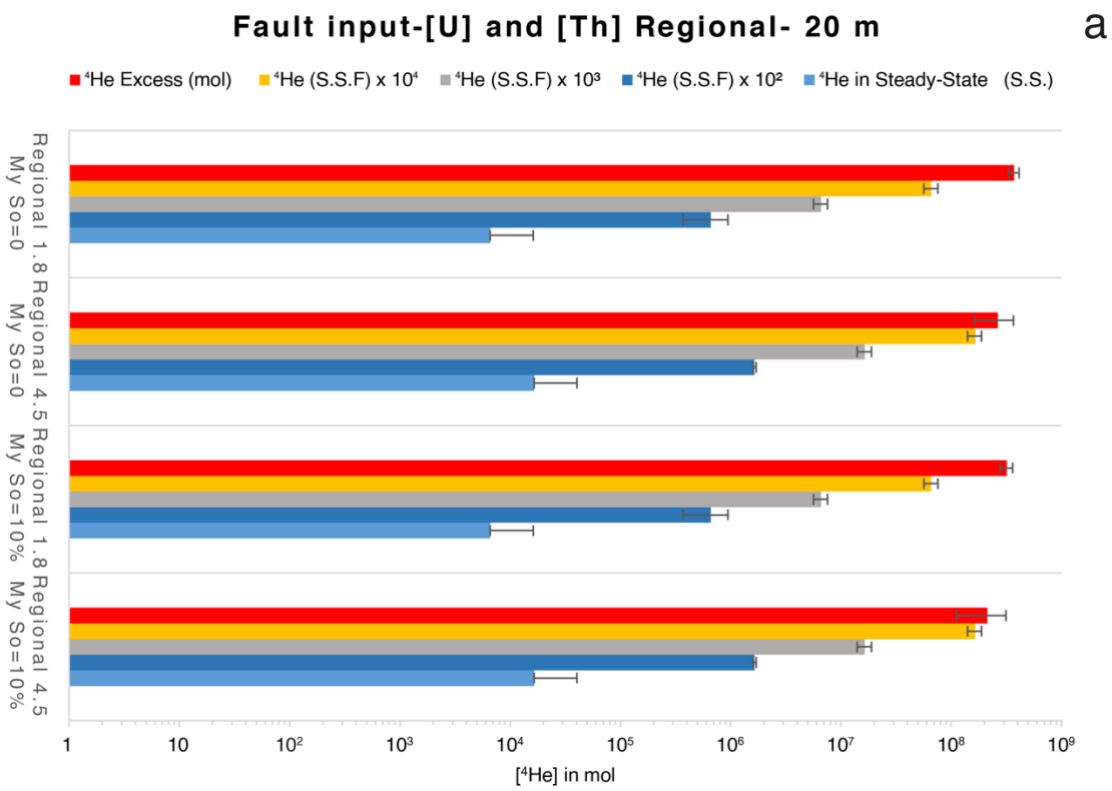

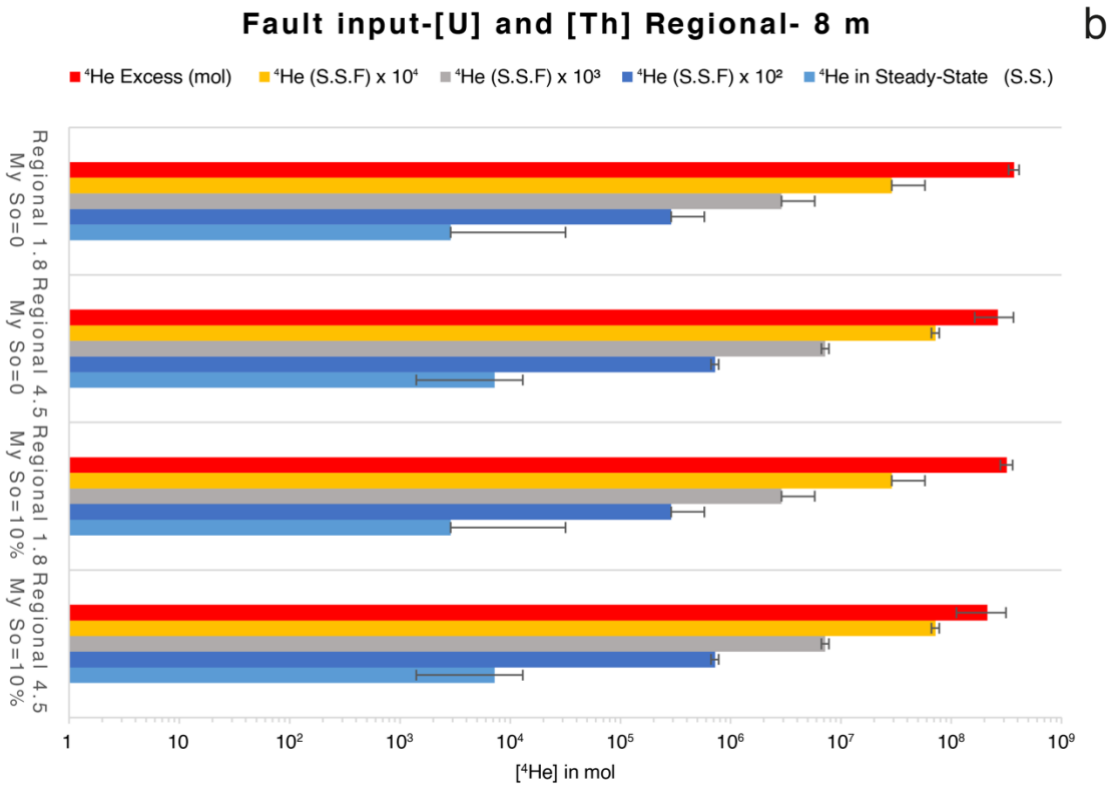

Figure I.6: Fault contribution to the release of ^{4}He. Calculated ^{4}He released in Steady-state and S.S.·10^{3}–10^{4} from faults system in Nirano (lateral extension 6250 m and length of the fault zone

300 m) and Regnano (lateral extension 8750 m and length of the fault zone 500 m) for a damage zone thickness of 20 m (**a**) and 8 m (**b**) with Regional U and Th contents.

The volume of the damage zones of the reservoir-related faults (from 0.015 km^3 to 0.088 km^3; Fig. I.2) releases an amount of He that matches the excess of He in the reservoirs if the release of ^4He is 10^4 times higher than that produces by pure diffusion process occurring within an undeformed rock volume (Figs. I.6). However, the high flux of volatiles from rocks as effect of dilatancy is not constant over time and it decreases in a scale of ka [26]. It means that in order to produce a continuous flux of volatiles high enough to justify the amount of ^4He presumed to be into the reservoirs, the stress field has to be constantly active since the reservoir formation age. This result shows that the active regional tectonic could substantially contribute to enhance the ^4He flux within the reservoir and that it can be an additional process to sustain the amount of ^4He stored in the trap (Figs. I.7). This implies that also the seismic activity has been occurring continuously since the origin of the gas traps.

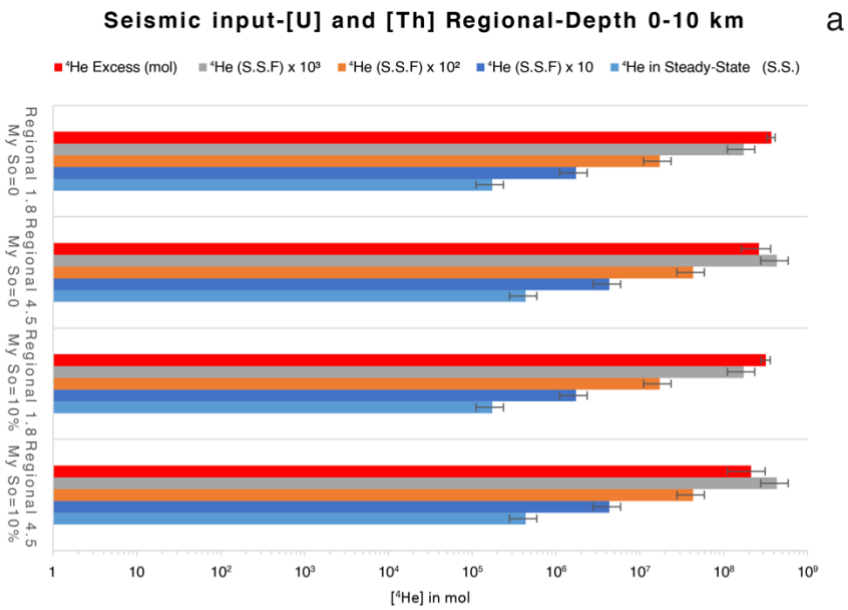
Seismic input-[U] and [Th] Regional-Depth 0-10 km
a
⁴He Excess (mol)
⁴He (S.S.F) x 10³
⁴He (S.S.F) x 10²
⁴He (S.S.F) x 10
⁴He in Steady-State (S.S.)
Regional 1-8 My So=0
Regional 4-5 My So=0
Regional 1-8 My So=10%
Regional 4-5 My So=10%
1
10
10²
10³
10⁴
10⁵
10⁶
10⁷
10⁸
10⁹
[⁴He] in mol

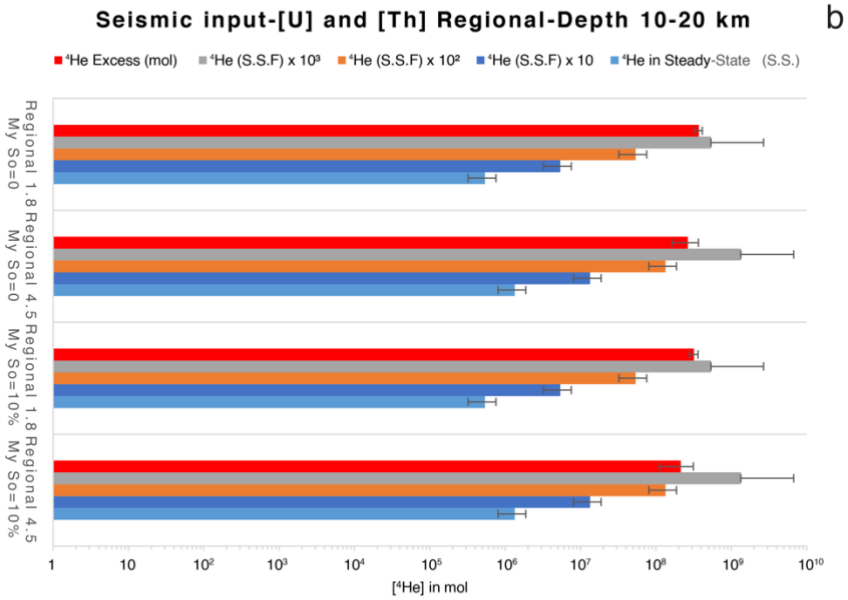
Seismic input-[U] and [Th] Regional-Depth 10-20 km
b
⁴He Excess (mol)
⁴He (S.S.F) x 10³
⁴He (S.S.F) x 10²
⁴He (S.S.F) x 10
⁴He in Steady-State (S.S.)
Regional 1-8 My So=0
Regional 4-5 My So=0
Regional 1-8 My So=10%
Regional 4-5 My So=10%
1
10
10²
10³
10⁴
10⁵
10⁶
10⁷
10⁸
10⁹
10¹⁰
[⁴He] in mol

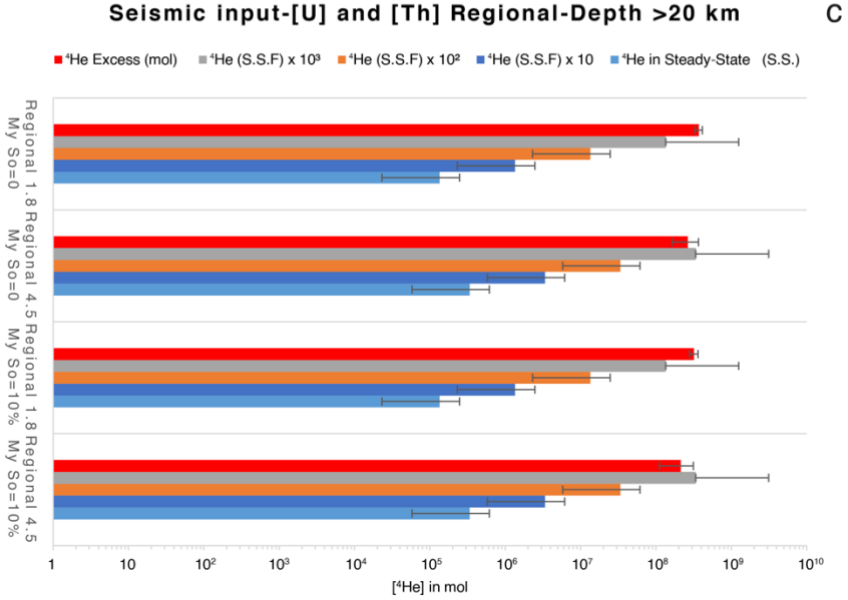
Seismic input-[U] and [Th] Regional-Depth >20 km
c
⁴He Excess (mol)
⁴He (S.S.F) x 10³
⁴He (S.S.F) x 10²
⁴He (S.S.F) x 10
⁴He in Steady-State (S.S.)
Regional 1-8 My So=0
Regional 4-5 My So=0
Regional 1-8 My So=10%
Regional 4-5 My So=10%
1
10
10²
10³
10⁴
10⁵
10⁶
10⁷
10⁸
10⁹
10¹⁰
[⁴He] in mol

Figure I.7: Seismic contribution to the release of ^{4}He. Calculated ^{4}He released in steady-state and S.S.·10^3–10^4 from deformed volume of rocks by earthquakes with average annual Mw calculated by means of estimated recurrence time after frequency-magnitude distribution by Zmap7 at 0–10 km depth (**a**) 10–20 km (**b**) and 20–32 km (**c**) for the uranium and thorium contents of the Regional suite.

I.3.5 Seismicity and degassing

We explored the hypothesis that the excess of He in the reservoirs may be due the occurrence of local earthquakes producing micro-fractures in crustal layers. Following the approach used by Sano et al. [28], which links the magnitude of an earthquake to the volume of rock affected by deformation and the related release of ^{4}He, we used the local (historical and instrumental) earthquakes activity as a proxy to calculate the amount of He released by the variation of the rock volume induced by each seismic event. We used the INGV database, covering the 1986–2018 time period (http://cnt.rm.ingv.it) for the instrumental earthquakes and the historical earthquakes catalogue (https://emidius.mi.ingv.it), covering the period 1501–1997, to compute the seismic energy released by the earthquakes located below the Nirano and Regnano systems. Moreover, we also extended the catalogue to the past (in terms of geological times), by assuming the same level of seismic energy release with time, from now up to the trap formation age. The considered events occurred at depths ranging between 5 km and 31 km and in 15 km wide sector along the axis of the anticline connecting Regnano to Nirano. We firstly converted the different types of magnitude reported in the catalogues (ML and Md) in moment magnitude (Mw). For the conversion from ML to Mw, we used the coefficients proposed by Castello et al. [86]. While we converted the Md to Mw by using the coefficients proposed by Selvaggi et al. [87]. We then computed the annual average of released energy (by using ZMAP computer code) for the analysis of seismic recurrences. The annual average of released energy is about 5.48×10^{16} ergs/y, which corresponds to one earthquake of magnitude equal to 3.3 per year. Thus, we computed the average volume of rock deformed by the earthquakes per year [28,88] by using the relationship:

$$LogV = 1.06M - 2.78 \qquad \text{(eq. I. 10)}$$

where V and M are the volume of rock affected by seismicity (km^3) and the moment magnitude, respectively. These values correspond to a volume of deformed rock of 5.13 km^3 per year that is higher than the volume of the faults damage zones. The amount of

He released from this volume are between $7.09 \cdot 10^{-2}$ and $3.58 \cdot 10^{-2}$ mol/y with a Regional or Global U and Th contents in the rock respectively. So, an increase of 3 orders of magnitude of the He released by the volume of deformed rocks, due to dilatancy [26,74], is still consistent to the amount of He estimated in the reservoirs (Figs. I.7). This result clearly indicates that the volume of deformed rock by stress field of the seismicity must be larger that the volume of the damage zone of the reservoir-related faults.

SUPPLEMENTARY FIGURES

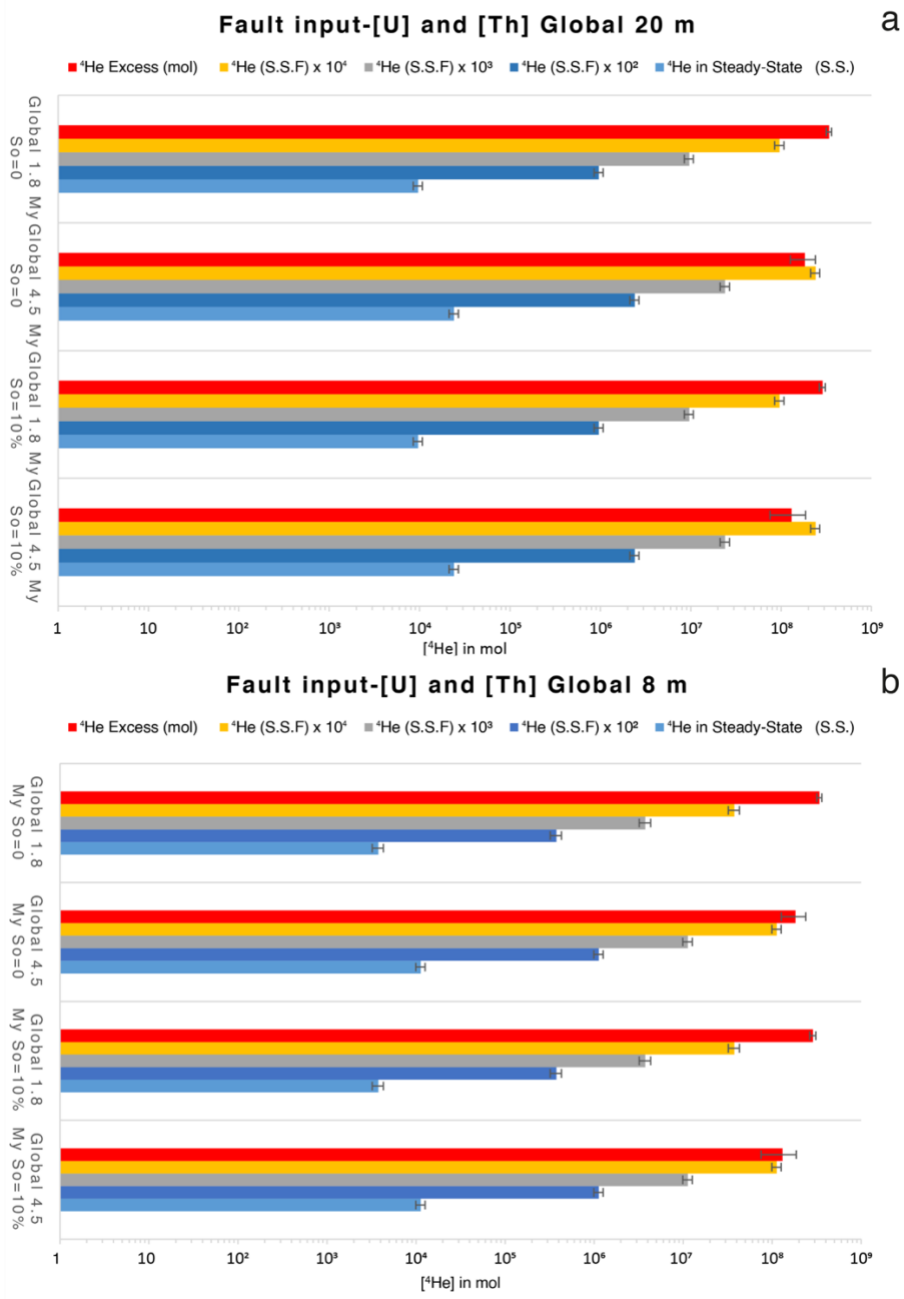

Figure. I.8: Fault contribution to the release of ^{4}He. Calculated ^{4}He released in Steady-state and S.S.·10^{2}-10^{3} from faults system in Nirano (lateral extension 6250 m and length of the fault zone 300 m) and Regnano (lateral extension 8750 m and length of the fault zone 500 m) for a damage zone thickness of 20 m (a) and 8 m (b) with Global U and Th contents.

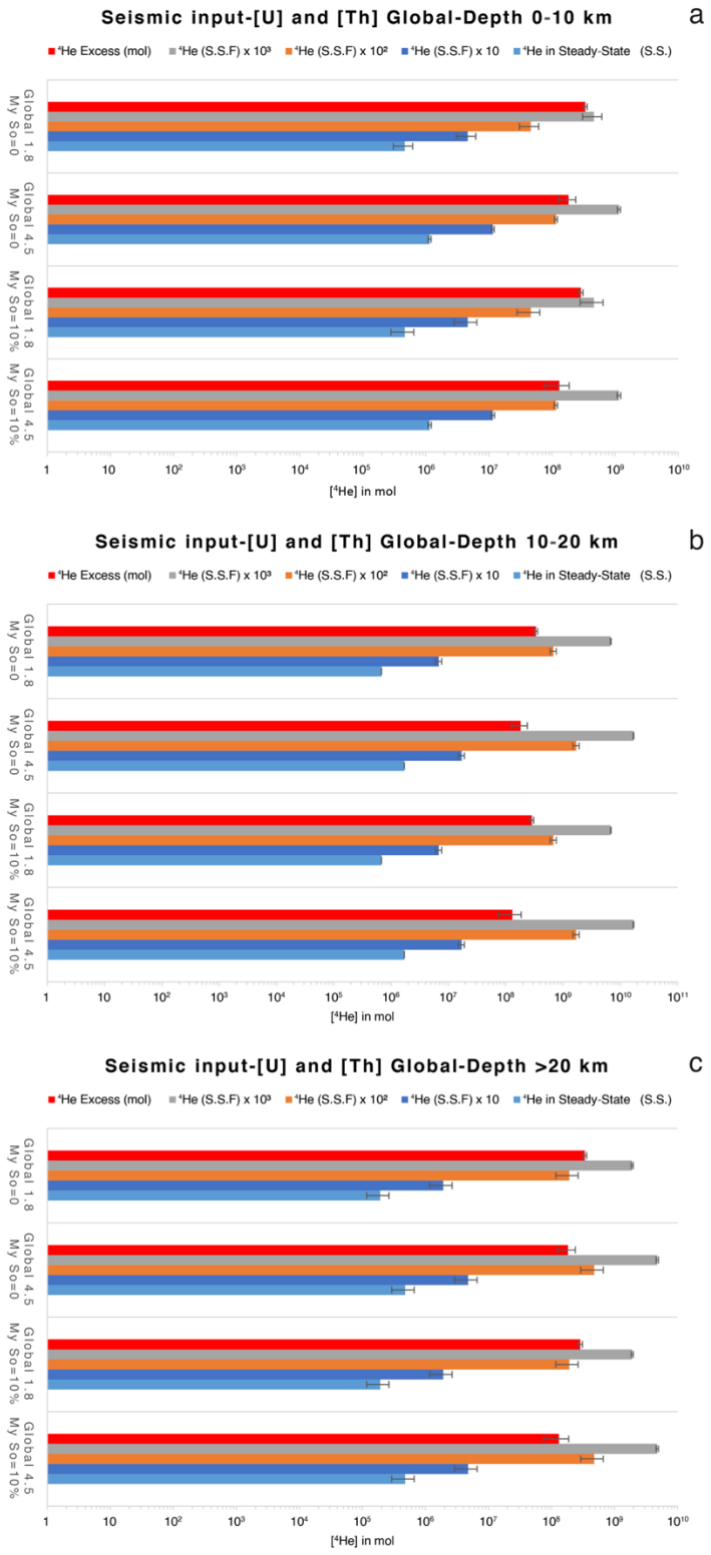

Figure I.9: Seismic contribution to the release of ^{4}He. Calculated ^{4}He released in steady-state and S.S.·10^2-10^3 from deformed volume of rocks by earthquakes with average annual Mw calculated by means of estimated recurrence time after frequency-magnitude distribution by Zmap7 at 0-10 km depth (a), 10-20 km (b) and 20-32 km (c) for the uranium and thorium contents of the Global suite.

I.4 REFERENCES

1. Torgersen, T. Continental degassing flux of4He and its variability. *Geochem. Geophys. Geosyst.* **11**, (2010).
2. Bao-jian, Jian-zhong, Wen-xuan, Zhi-long & Jie. Noble Gas Geochemistry of CO2 Gas Pool in Gaoqing-Pingnan Fault Zone,Jiyang Depression. *Geological Journal of China Universities* (2009).
3. Torgersen, T. & Clarke, W. B. Geochemical constraints on formation fluid ages, hydrothermal heat flux, and crustal mass transport mechanisms at Cajon Pass. *J. Geophys. Res.* **97**, 5031 (1992).
4. Etheridge, M. A., Wall, V. J., Cox, S. F. & Vernon, R. H. High fluid pressures during regional metamorphism and deformation: Implications for mass transport and deformation mechanisms. *J. Geophys. Res. [Solid Earth]* **89**, 4344–4358 (1984).
5. Tamburello, G., Chiodini, G., Pondrelli, S. & Rouwet, D. Global-scale correlation between CO2 earth degassing, major faults, tectonic regimes and heat flux: a review and update. in 13456 (2018).
6. Chiodini, G. *et al.* Carbon dioxide Earth degassing and seismogenesis in central and southern Italy. *Geophys. Res. Lett.* **31**, (2004).
7. Girault, F. *et al.* Persistent CO2 emissions and hydrothermal unrest following the 2015 earthquake in Nepal. *Nat. Commun.* **9**, 2956 (2018).
8. Maestrelli, D. *et al.* Dynamic Triggering of Mud Volcano Eruptions During the 2016-2017 Central Italy Seismic Sequence. *J. Geophys. Res. [Solid Earth]* **122**, 9149–9165 (2017).
9. Manga, M., Brumm, M. & Rudolph, M. L. Earthquake triggering of mud volcanoes. *Mar. Pet. Geol.* **26**, 1785–1798 (2009).
10. Holland, G. & Gilfillan, S. Application of Noble Gases to the Viability of CO2 Storage. in *The Noble Gases as Geochemical Tracers* (ed. Burnard, P.) 177–223 (Springer Berlin Heidelberg, 2013). doi:10.1007/978-3-642-28836-4_8.
11. Parai, R. & Mukhopadhyay, S. Xenon isotopic constraints on the history of volatile recycling into the mantle. *Nature* **560**, 223–227 (2018).

12. Avice, G., Marty, B. & Burgess, R. The origin and degassing history of the Earth's atmosphere revealed by Archean xenon. *Nat. Commun.* **8**, 15455 (2017).
13. Ballentine, C. J. & Burnard, P. G. Production, Release and Transport of Noble Gases in the Continental Crust. *Rev. Mineral. Geochem.* **47**, 481–538 (2002).
14. Ozima, M. & Podosek, F. A. *Noble Gas Geochemistry*. (Cambridge University Press, 2002). doi:10.1017/cbo9780511545986.
15. Mamyrin, B. A. & Tolstikhin, I. N. *Helium Isotopes in Nature*. (Elsevier, 2013).
16. Allègre, C. J., Moreira, M. & Staudacher, T. 4He/^{3}He dispersion and mantle convection. *Geophys. Res. Lett.* **22**, 2325–2328 (1995).
17. Mabry, J., Lan, T., Burnard, P. & Marty, B. High-precision helium isotope measurements in air. *J. Anal. At. Spectrom.* **28**, 1903–1910 (2013).
18. Ballentine, C. J., Schoell, M., Coleman, D. & Cain, B. A. 300-Myr-old magmatic CO2 in natural gas reservoirs of the west Texas Permian basin. *Nature* **409**, 327–331 (2001).
19. O'Nions, R. K. & Oxburgh, E. R. Helium, volatile fluxes and the development of continental crust. *Earth Planet. Sci. Lett.* **90**, 331–347 (1988).
20. Kulongoski, J. T. *et al.* Volatile fluxes through the Big Bend section of the San Andreas Fault, California: Helium and carbon-dioxide systematics. *Chem. Geol.* **339**, 92–102 (2013).
21. Caracausi, A. & Paternoster, M. Radiogenic helium degassing and rock fracturing: A case study of the southern Apennines active tectonic region. *J. Geophys. Res. [Solid Earth]* **120**, 2200–2211 (2015).
22. Kennedy, B. M. *et al.* Mantle Fluids in the San Andreas Fault System, California. *Science* **278**, 1278–1281 (1997).
23. Kennedy, B. M. & van Soest, M. C. Flow of mantle fluids through the ductile lower crust: helium isotope trends. *Science* **318**, 1433–1436 (2007).
24. Ballentine, C. J., Burgess, R. & Marty, B. Tracing Fluid Origin, Transport and Interaction in the Crust. *Rev. Mineral. Geochem.* **47**, 539–614 (2002).
25. Bräuer, K., Geissler, W. H., Kämpf, H., Niedermannn, S. & Rman, N. Helium and carbon isotope signatures of gas exhalations in the westernmost part of the Pannonian Basin (SE Austria/NE Slovenia): Evidence for active lithospheric mantle degassing. *Chem. Geol.* **422**, 60–70 (2016).
26. Torgersen, T. & O'Donnell, J. The degassing flux from the solid earth: Release by fracturing. *Geophys. Res. Lett.* **18**, 951–954 (1991).

27. Sano, Y. *et al.* Groundwater oxygen anomaly related to the 2016 Kumamoto earthquake in Southwest Japan. *Proc. Jpn. Acad. Ser. B Phys. Biol. Sci.* **96**, 322–334 (2020).
28. Sano, Y., Takahata, N., Igarashi, G., Koizumi, N. & Sturchio, N. C. Helium degassing related to the Kobe earthquake. *Chem. Geol.* **150**, 171–179 (1998).
29. Bonini, M. Interrelations of mud volcanism, fluid venting, and thrust-anticline folding: Examples from the external northern Apennines (Emilia-Romagna, Italy). *J. Geophys. Res. [Solid Earth]* **112**, 1–21 (2007).
30. Etiope, G., Martinelli, G., Caracausi, A. & Italiano, F. Methane seeps and mud volcanoes in Italy: Gas origin, fractionation and emission to the atmosphere. *Geophys. Res. Lett.* **34**, 1–5 (2007).
31. Oppo, D., Capozzi, R. & Picotti, V. A new model of the petroleum system in the Northern Apennines, Italy. *Mar. Pet. Geol.* **48**, 57–76 (2013).
32. Choi, J.-H., Edwards, P., Ko, K. & Kim, Y.-S. Definition and classification of fault damage zones: A review and a new methodological approach. *Earth-Sci. Rev.* **152**, 70–87 (2016).
33. Evans, J. P. Thickness-displacement relationships for fault zones. *J. Struct. Geol.* **12**, 1061–1065 (1990).
34. Scholz, C. H., Dawers, N. H., Yu, J.-Z., Anders, M. H. & Cowie, P. A. Fault growth and fault scaling laws: Preliminary results. *J. Geophys. Res. [Solid Earth]* **98**, 21951–21961 (1993).
35. Savage, H. M. & Brodsky, E. E. Collateral damage: Evolution with displacement of fracture distribution and secondary fault strands in fault damage zones. *J. Geophys. Res. [Solid Earth]* **116**, (2011).
36. Torabi, A. & Berg, S. S. Scaling of fault attributes: A review. *Mar. Pet. Geol.* **28**, 1444–1460 (2011).
37. Childs, C., Nicol, A., Walsh, J. J. & Watterson, J. Growth of vertically segmented normal faults. *J. Struct. Geol.* **18**, 1389–1397 (1996).
38. Knott, S. D. *et al.* Spatial and mechanical controls on normal fault populations. *J. Struct. Geol.* **18**, 359–372 (1996).
39. Vermilye, J. M. & Scholz, C. H. The process zone: A microstructural view of fault growth. *J. Geophys. Res. [Solid Earth]* **103**, 12223–12237 (1998).
40. Beach, A., Welbon, A. I., Brockbank, P. J. & McCallum, J. E. Reservoir damage around faults; outcrop examples from the Suez Rift. *Pet. Geosci.* **5**, 109–116 (1999).

41. Fossen, H. & Hesthammer, J. Possible absence of small faults in the Gullfaks Field, northern North Sea: implications for downscaling of faults in some porous sandstones. *J. Struct. Geol.* **22**, 851–863 (2000).
42. Shipton, Z. K., Soden, A. M., Kirkpatrick, J. D., Bright, A. M. & Lunn, R. J. How Thick is a Fault? Fault Displacement-Thickness Scaling Revisited. in *Earthquakes: Radiated Energy and the Physics of Faulting* 193–198 (American Geophysical Union (AGU), 2006). doi:10.1029/170GM19.
43. Mitchell, T. M. & Faulkner, D. R. The nature and origin of off-fault damage surrounding strike-slip fault zones with a wide range of displacements: A field study from the Atacama fault system, northern Chile. *J. Struct. Geol.* **31**, 802–816 (2009).
44. Faulkner, D. R., Mitchell, T. M., Jensen, E. & Cembrano, J. Scaling of fault damage zones with displacement and the implications for fault growth processes. *J. Geophys. Res. [Solid Earth]* **116**, (2011).
45. McGrath, A. G. & Davison, I. Damage zone geometry around fault tips. *J. Struct. Geol.* **17**, 1011–1024 (1995).
46. Rizzo, A. L. *et al.* New mafic magma refilling a quiescent volcano: Evidence from He-Ne-Ar isotopes during the 2011-2012 unrest at Santorini, Greece. *Geochem. Geophys. Geosyst.* **16**, 798–814 (2015).
47. Sano, Y. & Wakita, H. Geographical distribution of3He/4He ratios in Japan: Implications for arc tectonics and incipient magmatism. *J. Geophys. Res.* **90**, 8729–8741 (1985).
48. Battaglia, A. *et al.* The magmatic gas signature of pacaya volcano, with implications for the volcanic CO2Flux from Guatemala. *Geochem. Geophys. Geosyst.* **19**, 667–692 (2018).
49. Gennaro, M. E., Grassa, F., Martelli, M., Renzulli, A. & Rizzo, A. L. Carbon isotope composition of CO2-rich inclusions in cumulate-forming mantle minerals from Stromboli volcano (Italy). *J. Volcanol. Geotherm. Res.* **346**, 95–103 (2017).
50. Nuccio, P. M., Caracausi, A. & Costa, M. Mantle-derived fluids discharged at the Bradanic foredeep/Apulian foreland boundary: The Maschito geothermal gas emissions (southern Italy). *Mar. Pet. Geol.* **55**, 309–314 (2014).
51. Carapezza, M. L. *et al.* Gas blowout from shallow boreholes near Fiumicino International Airport (Rome): Gas origin and hazard assessment. *Chem. Geol.* **407–408**, 54–65 (2015).

52. Tobergte & Curtis. Assessment of Uncertainties in Oil and Gas Reserves Estimation by Various Evaluation Methods. *J. Chem. Inf. Model.* **53**, 1689–1699.
53. Demirmen, F. Reserves estimation: The challenge for the industry. *J. Pet. Technol.* **59**, 80–89 (2007).
54. Mazzei, R. Calcolo volumetrico degli idrocarburi originariamente in posto. in *Elementi di geologia e di ingegneria dei giacimenti petroliferi* vol. FASCICOL07 (2001).
55. Mireault, R. & Dean, L. *RESERVOIR ENGINEERING for Geologists*. (Fekete Associates Inc., 2012).
56. Timur, A. An Investigation Of Permeability, Porosity, & Residual Water Saturation Relationships For Sandstone Reservoirs. *The Log Analyst* **9**, 10 (1968).
57. Piper, L. D., McCain, W. D. & Corredor, J. H. Compressibility factors for naturally occurring petroleum gases. *SPE Reprint Series* 23–33 (1999) doi:10.2118/26668-MS.
58. Oppo, D. Studio dei vulcani di fango per la definizione della migrazione dei fluidi profondi. (Università di Bologna Dipartimento, 2012).
59. Liu, W. *et al.* Formation time of gas reservoir constrained by the time-accumulation effect of 4He: Case study of the Puguang gas reservoir. *Chem. Geol.* **469**, 246–251 (2017).
60. Martinelli, G. & Judd, A. Mud volcanoes of Italy. *Geol. J.* **39**, 49–61 (2004).
61. Martinelli, G., Alberto, D. & Mucciarelli, M. Radon emissions from mud volcanoes in Northern Italy: possible connection with local seismicity. *Geophys. Res. Lett.* **22**, 1989–1992 (1995).
62. Rudolph, M. L. & Manga, M. Frequency dependence of mud volcano response to earthquakes. *Geophys. Res. Lett.* **39**, 1–5 (2012).
63. Martinelli, G. & Panahi, B. *Mud Volcanoes, Geodynamics and Seismicity: Proceedings of the NATO Advanced Research Workshop on Mud Volcanism, Geodynamics and Seismicity, Baku, Azerbaijan, from 20 to 22 May 2003*. (Springer Netherlands, 2006).
64. Martinelli, G. & Dadomo, A. Mud Volcano Monitoring and Seismic Events. in *Mud Volcanoes, Geodynamics and Seismicity* (eds. Martinelli, G. & Panahi, B.) 187–199 (Springer Netherlands, 2005).
65. Etiope, G., Feyzullayev, A. & Baciu, C. L. Terrestrial methane seeps and mud volcanoes: A global perspective of gas origin. *Mar. Pet. Geol.* **26**, 333–344 (2009).

66. Capozzi, R. & Picotti, V. Fluid migration and origin of a mud volcano in the Northern Apennines (Italy): The role of deeply rooted normal faults. *Terra Nova* **14**, 363–370 (2002).
67. Gautheron, C., Moreira, M. & Allègre, C. He, Ne and Ar composition of the European lithospheric mantle. *Chem. Geol.* **217**, 97–112 (2005).
68. Sciarra, A., Cantucci, B., Ricci, T., Tomonaga, Y. & Mazzini, A. Geochemical characterization of the Nirano mud volcano, Italy. *Appl. Geochem.* **102**, 77–87 (2019).
69. Milkov, A. V. & Etiope, G. Revised genetic diagrams for natural gases based on a global dataset of >20,000 samples. *Org. Geochem.* **125**, 109–120 (2018).
70. Ozima, M. & Podosek, F. A. *Noble Gas Geochemistry: 2nd edition*. 286 (Cambridge University Press; 2 edition (December 24, 2001), 2002).
71. Mamyrin, B. A. & Tolstikhin, I. N. *Helium isotopes in nature DEVELOPMENTS IN GEOCHEMISTRY*. 249–267 (Elsevier Science Ltd, 1984). doi:10.1016/B978-0-444-42180-7.50016-8.
72. Torgersen, T. & Clarke, W. B. Helium accumulation in groundwater, I: An evaluation of sources and the continental flux of crustal4He in the Great Artesian Basin, Australia. *Geochim. Cosmochim. Acta* **49**, 1211–1218 (1985).
73. Scholz, C. H., Sykes, L. R. & Aggarwal, Y. P. Earthquake Prediction: A Physical Basis. *Science* **181**, 803 LP – 810 (1973).
74. Honda, M., Kurita, K., Hamano, Y. & Ozima, M. Experimental studies of He and Ar degassing during rock fracturing. *Earth Planet. Sci. Lett.* **59**, 429–436 (1982).
75. Thomas, D. Geochemical precursors to seismic activity. *Pure and Applied Geophysics PAGEOPH* **126**, 241–266 (1988).
76. Tapponier, P. & Brace, W. F. Development of stress induced microcracks in {W}esterly granite. *Int. J. Mech. Min. Sci. Geomech. Abstr.* **13**, 103–112 (1976).
77. Bauer. Real Time Degassing of Rock during Deformation. *No. SAND2016-1483C* (2016).
78. Bauer, S. J., Gardner, W. P., Heath, J. E., Payton Gardner, W. & Heath, J. E. Helium release during shale deformation: Experimental validation. *Geochem. Geophys. Geosyst.* **17**, 2612–2622 (2016).
79. Takahata, N. & Sano, Y. Helium flux from a sedimentary basin. *Appl. Radiat. Isot.* **52**, 985–992 (2000).

80. Bonini, M. Mud volcano eruptions and earthquakes in the Northern Apennines and Sicily, Italy. *Tectonophysics* **474**, 723–735 (2009).
81. Coltorti, M. *et al.* U and Th content in the Central Apennines continental crust: A contribution to the determination of the geo-neutrinos flux at LNGS. *Geochim. Cosmochim. Acta* **75**, 2271–2294 (2011).
82. Zhou, Z. & Ballentine, C. J. 4He dating of groundwater associated with hydrocarbon reservoirs. *Chem. Geol.* **226**, 309–327 (2006).
83. Craig, H. & Lupton, J. E. Primordial neon, helium, and hydrogen in oceanic basalts. *Earth Planet. Sci. Lett.* **31**, 369–385 (1976).
84. Rudnick, R. L. & Fountain, D. M. Nature and composition of the continental crust: A lower-crustal perspective. *Rev. Geophys.* **33**, 267–309 (1995).
85. Lavecchia, G., Boncio, P., Creati, N. & Brozzetti, F. Some Aspects Of The Italian Geology Not Fitting With A Subduction Scenario. https://www.researchgate.net/publication/250276312 doi:10.3809/jvirtex.2003.00064.
86. Castello, B., Olivieri, M. & Selvaggi, G. Local and duration magnitude determination for the Italian earthquake catalog, 1981-2002. *Bull. Seismol. Soc. Am.* **97**, 128–139 (2007).
87. Selvaggi, G., Castello, B. & Azzara, R. Spatial distribution of scalar seismic moment release in Italy (1983-1996): seismotectonics implications for the Apennines. *Annali di Geofisica* vol. 40 1565–1578 (1997).
88. Shimazu, Y. Physics of the Earth. *Shokabo Press* (1971).

CHAPTER II

Analysis of variability helium outputs from the Irpinia Fault Zone, Italy

II.1 INTRODUCTION CHAPTER II

The composition of the atmosphere and its evolution over time was mainly driven by natural degassing from the Earth interior [1] up to the industrial age. Volcanic activity fed the release of huge amounts of volatiles into atmosphere [2], making volcanoes major emitters of natural volatiles and hence controlling the budget of volatiles in the atmosphere. Considerable attention has recently been paid to the outgassing in active tectonic regions because faults are regions of enhanced permeability and porosity where fluids can migrate through the whole crust [3,4], and these latter can in turn alter the faults state of stress playing an active role in the generation of catastrophic earthquakes [5–9].

Noble gases are powerful tools for reconstructing the birth of the Earth, its interior and the evolution over time [10–13]. Their isotopic ratios are used to investigate the dynamics of natural processes such as volcanic eruptions and earthquakes [14–18]. The lightest of the noble gases is helium (hereafter He), whose low atomic mass means that it is the only one that is able to escape into space [10]. He on Earth is present as two isotopes, ^{3}He and ^{4}He, with the former being mainly primordial and stored in the mantle, and the latter continuously produced by uranium (U) and thorium (Th) decay in the Earth's interior [10]. The He flux in stable continental regions is dominated by the radiogenic ^{4}He that is produced in the crust (mantle He <1%) [19]. In contrast, the primordial ^{3}He escapes into the atmosphere mainly from volcanoes and in regions of active tectonic (from extensive to compressive), which makes the He isotopic ratio ($^{3}He/^{4}He$) a powerful tool for recognizing mantle-crust tectonics in the absence of other geological evidence [4,19,20].

On the continents, groundwater acquires crustal ^{4}He from the rocks that constitute the aquifer, and from the underlying crust during their circulation. Indeed, the large aquifers worldwide contribute strongly to the discharge of crustal ^{4}He into atmosphere [21] . However, there is strong evidence that the continental degassing is also episodic [22], and depends on large-scale metamorphism and tectonics [23–27]. The latter degassing mechanism implies large variabilities in time and space of the crustal ^{4}He outgassing to

the atmosphere and also enhanced mass transfer of fluids through the crust [22,27]. It remains a challenge to quantify how the different processes occurring at depth (e.g. metamorphism, tectonics, earthquakes) sustain the release of crustal ^{4}He and influence the impulsive nature of its degassing. In this scenario, identifying quantitative constraints of the volume of the fault zone at depth and the related capacity of rock underlying the impulsive degassing of ^{4}He would provide powerful tools for understanding Earth degassing and the natural processes that are associated with disastrous natural events such as earthquakes.

The enhancement of rock deformation due to tectonics results in the opening and development of fractures within the crust at the grain scale. Such microscale fracturing increases as an effect of dilatation until macroscopic failures occur and the strain is released. As a consequence of the dilatancy-related microscale fracturing, crustal ^{4}He stored in rocks is liberated faster from minerals and rocks [25,26,28] and it escapes towards the pore fluids and successively through the crust to the atmosphere [23]. In this framework, earthquake-related changes in volumetric strains increase the release of crustal ^{4}He from rocks [27], highlighting the direct linkage between seismicity and the impulsive nature of the crustal ^{4}He degassing. This evidence is augmented by rare observations of increases in the amounts of crustal ^{4}He in natural fluids associated with high-magnitude earthquakes, such as the Kumamoto Earthquake in 2016 (M=7.3) and the Kobe earthquake in 1995 (M=7.2) [29,30].

While brittle faults are often imagined as single planar structures, in reality they should be seen as complex volumetric fault zones composed of a variety of internal structures. A fault zone can be schematically simplified in two main structural regions (Fig. II. 1): (1) the fault core and (2) the damage zone [31]. The fault core to the volume of highly localized strain and intense shearing where most of the fault displacement is accommodated by structures as gouges, cataclasites and breccias. A damage zone is the broader volume around the fault core that exhibits second-order

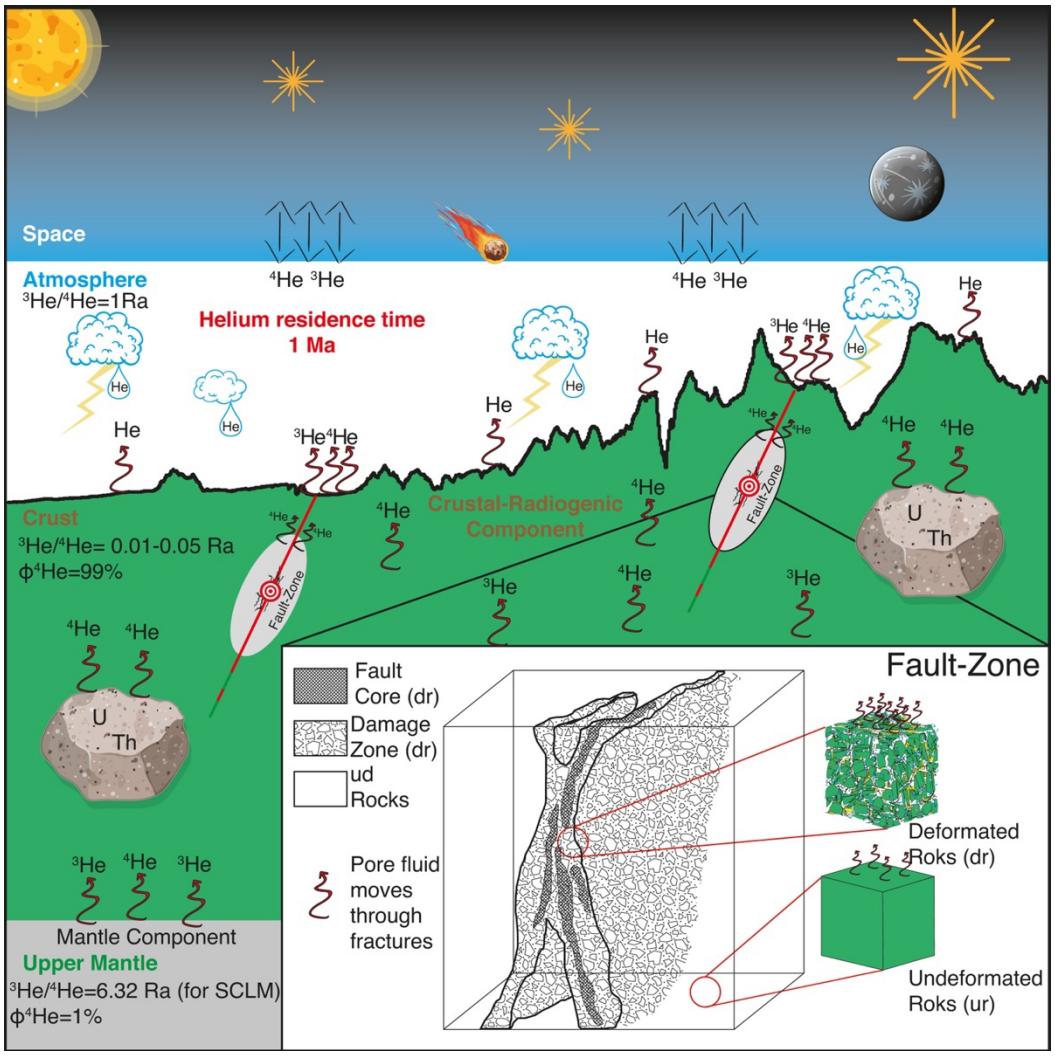

Figure II.1: Two-dimensional sketch of earth interior below continents and the atmosphere. Helium escapes from the continents to the atmosphere that exchanges it with space. In stable continental regions, the crustal radiogenic ^{4}He dominates the output of He and the mantle component is about 1% (more details are in text). In active tectonic regions, the faults are region of enhanced porosity and permeability and they are the network of pathways through which fluids preferentially transfer to the atmosphere. Furthermore, the volumes of rocks that constitute the faults zones (damage zone plus fault core) are extensively deformed and fractured enhancing the release of crustal ^{4}He because of the volumetric stress change. The insert shows a zoomed schematic representation of the fault zones as fault core plus the damage zone and the adjacent un-deformed rocks.

structures (e.g., subsidiary faults, fractures, and veins), whose long-term evolution represents a key factor for strain distribution, earthquake rupture propagation, and fluid circulation in the crust. These regions represent the primary crustal volumes contributing to the enhanced release of crustal ^{4}He. Its release from the rock increases with fracture development, with the ^{4}He output reaching up to 10^4 times the crustal ^{4}He steady-state flux [23,32] that mainly dominates ^{4}He degassing in old stable continental regions [22].

In this framework, it must be considered that both the damage zone and the fault core can host large amounts of fluids of different origins and compositions (e.g. H_2O, CO_2) [33,34] which play a fundamental role as a carrier of ^4He that migrates through the crust. In a conceptual model (Fig. II. 1) where deformation and the related seismicity can result in ^4He escaping from the minerals and rocks in which it was produced and accumulated, the fault zones thus represent (1) the zone of enhanced release of crustal ^4He and (2) the networks of pathways through which fluids preferentially transfer crustal ^4He through the crust towards the atmosphere (Fig. II. 1).

Several fieldwork and laboratory studies have investigated the volumetric changes and evolution of the fault core and damage zone due to tectonics [31,35], as well as the relationship between the nature of the damage zone and earthquake characteristics [36,37]. However, damage zone width is generally defined by studies of exhumed structures. Inconsistencies in calculation of damage zone width (e.g., due to subjectivity or ambiguity of definition and measures) makes it difficult to assess the volume of rocks at depth associated with faults where crustal ^4He release is enhanced. Microearthquakes can revolutionize our approach to the study of crustal phenomena. In recent decades the development of dense seismic networks worldwide has generated rich, long-term earthquake catalogues, and microearthquakes can now be used as beacons for observing crustal processes down to tens of kilometers depth.

Microearthquakes indeed occur in damage zones and, hence, they allow determining the detailed structure of seismogenic fault zones at depth, to inquire about the relationships between earthquake nucleation, rock types and the presence of fluids in the fault zone [38]. The outcomes of such analyses provide new opportunities to decipher the effects of seismicity on Earth degassing and provide fundamental new insight for reconciling the dichotomy between the steady-state model and the impulsive nature of Earth degassing.

II. 2 **METHODS**

II. 2.1 **Whole crust He degassing in steady-state conditions**

On a 1-Ma timescale, the flux of ^4He from the Earth's crust to the atmosphere is comparable to the net in situ production by alpha decay of U- and Th-series elements at

the 30-40 km depth of the crust [39], suggesting that the ^{4}He flux exists in the crust and eventually reaches the atmosphere with a steady flux Liu et al (2017) [40].

The rate of ^{4}He production (and release in S.S. conditions) due to α-decay of U and Th throughout the crust beneath the study area (Q_C He in moles per year) is equivalent to [24]:

$$Q_{c,y} = \frac{M_{c,y}}{N_A} \cdot \alpha = \delta_c \cdot (S_{c,y} \cdot H_c) \cdot \alpha \quad \text{(eq. II.1)}$$

where Mc,y is the annual mass of crust beneath the IRPZ in grams, calculated as the product of the density and volume of the crust beneath the study area, which is calculated as the product of the annual surface area (Sc,y) and the crustal thickness, and where this latter is given by the sum of carbonate, middle crust and lower crust thicknesses ($HC=Hc+H_{MC}+H_{LC}$). N_A is the Avogadro constant and α is the crustal production of ^{4}He in molgrams per year. In turn [23]

$$\alpha = (3.115 \times 10^6 + 1.272 \times 10^5) \cdot [U] + 7.710 \times 10^5 \cdot [Th] \quad \text{(eq. II. 2)}$$

where [U] and [Th] are respectively the concentrations of U and Th in the crust in parts per million by weight respectively [23,24].

To compute Qc, we used literature data for the abundances of U and Th and crust thickness (Table II. 1). In particular, we use three sets of U and Th concentrations for estimating the Steady-State level for area. Regarding the first and second set, we base our analysis on the U and Th amounts for a Regional Refined Reference Model and the Global Refined Reference Model proposed by Coltorti et al. (2011) [41]. For the third set, we refer to the values proposed by O'Nions and Oxburgh 1983) [19].

Y	Qc			Qfc	Qdz		
	Regional S.S.	Global S.S.	Global O-O S.S.		Median	Q1	Q3
2008	$1.75 \cdot 10^{03}$	$4.13 \cdot 10^{03}$	$1.75 \cdot 10^{04}$	$3.88 \cdot 10^{-10}$	0.07	$3.70 \cdot 10^{-02}$	$1.18 \cdot 10^{-01}$
2009	$1.73 \cdot 10^{03}$	$4.08 \cdot 10^{03}$	$1.73 \cdot 10^{04}$	$6.01 \cdot 10^{-10}$	0.16	$9.33 \cdot 10^{-02}$	$2.78 \cdot 10^{-01}$
2010	$1.65 \cdot 10^{03}$	$3.91 \cdot 10^{03}$	$1.66 \cdot 10^{04}$	$1.41 \cdot 10^{-09}$	0.23	$1.33 \cdot 10^{-01}$	$4.01 \cdot 10^{-01}$
2011	$1.62 \cdot 10^{03}$	$3.84 \cdot 10^{03}$	$1.63 \cdot 10^{04}$	$6.94 \cdot 10^{-10}$	0.43	$2.36 \cdot 10^{-01}$	$7.30 \cdot 10^{-01}$
2012	$2.04 \cdot 10^{03}$	$4.81 \cdot 10^{03}$	$2.04 \cdot 10^{04}$	$4.80 \cdot 10^{-09}$	0.78	$4.96 \cdot 10^{-01}$	$1.20 \cdot 10^{00}$
2013	$1.72 \cdot 10^{03}$	$4.07 \cdot 10^{03}$	$1.72 \cdot 10^{04}$	$1.12 \cdot 10^{-09}$	0.22	$1.08 \cdot 10^{-01}$	$4.34 \cdot 10^{-01}$
2014	$2.03 \cdot 10^{03}$	$4.81 \cdot 10^{03}$	$2.04 \cdot 10^{04}$	$5.68 \cdot 10^{-09}$	0.17	$9.79 \cdot 10^{-02}$	$3.13 \cdot 10^{-01}$
2015	$1.54 \cdot 10^{03}$	$3.64 \cdot 10^{03}$	$1.54 \cdot 10^{04}$	$4.27 \cdot 10^{-10}$	0.09	$4.14 \cdot 10^{-02}$	$1.68 \cdot 10^{-01}$
2016	$1.55 \cdot 10^{03}$	$3.67 \cdot 10^{03}$	$1.56 \cdot 10^{04}$	$1.11 \cdot 10^{-09}$	0.08	$4.74 \cdot 10^{-02}$	$1.27 \cdot 10^{-01}$
2017	$1.24 \cdot 10^{03}$	$2.94 \cdot 10^{03}$	$1.24 \cdot 10^{04}$	$1.26 \cdot 10^{-09}$	0.09	$5.05 \cdot 10^{-02}$	$1.78 \cdot 10^{-01}$
2018	$1.58 \cdot 10^{03}$	$3.74 \cdot 10^{03}$	$1.59 \cdot 10^{04}$	$1.10 \cdot 10^{-09}$	0.08	$4.89 \cdot 10^{-02}$	$1.42 \cdot 10^{-01}$
2019	$1.72 \cdot 10^{03}$	$4.06 \cdot 10^{03}$	$1.72 \cdot 10^{04}$	$1.47 \cdot 10^{-08}$	0.91	$5.31 \cdot 10^{-01}$	$1.49 \cdot 10^{00}$

Table II.1: Rate of ^{4}He in mol y^{-1}. Rate of ^{4}He for Regional, global and global O-O configuration steady state and also to a rate of fault zone distinguished in fault core and damage zone in undeformed conditions.

Thereafter, we will refer to the result of these three configurations as the Regional, global and O-O steady-state, respectively. In addition, in the regional case, we considered granites and gabbro as alternatives in place of carbonates (see Table II. 2 for U and Th abundance and Figs. II. 2 and II. 3 result).

	Regional			Gloabal			Gloabal O-O			H	density
	U	Th	ref	U	Th	ref	U	Th/U	ref	km	g km^{-3}
Carbonates	0.33	0.19	(47)	1.68	6.91	(47)					$2.50 \cdot 10^{15}$
Granites	4	52	(49)							15.00	$2.64 \cdot 10^{15}$
Gabbro	1	3.5	(49)				6.00	3.80	(23)		$3.03 \cdot 10^{15}$
MC	1.6	6.1	(47)	1.3	6.50	(47)				6.00	$2.82 \cdot 10^{15}$
LC	0.29	3.17	(47)	0.6	3.70	(47)				6.00	$2.98 \cdot 10^{15}$

Table II. 2: Abundances of U and Th (in ppm), crust thickness and density used for calculations of ^{4}He production.

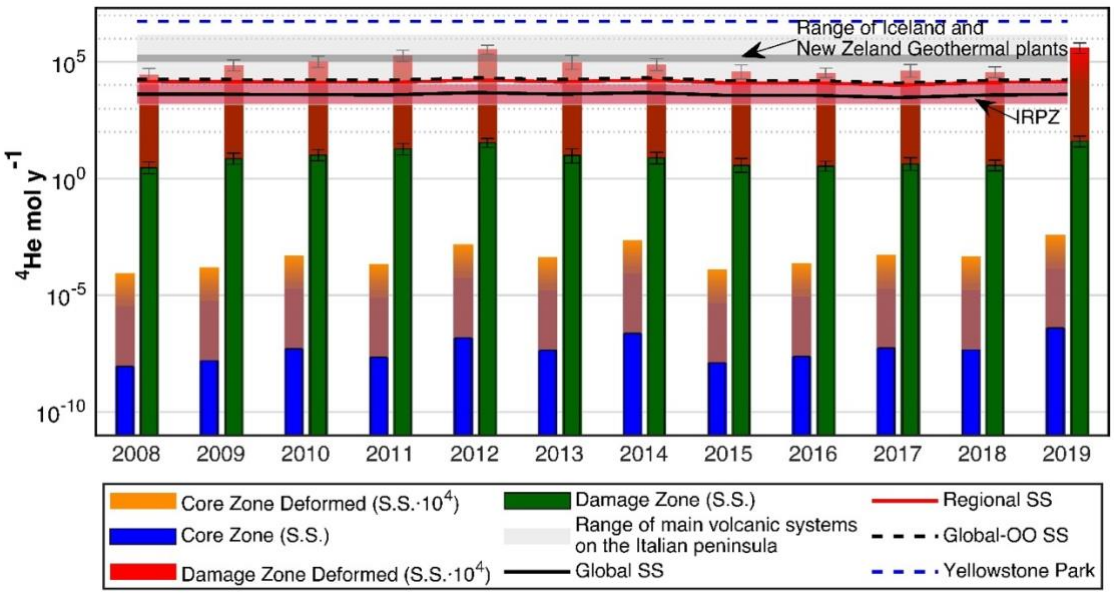

Figure II. 2: Variability of the crustal ^{4}He outputs in Granite. Output of crustal ^{4}He from faults cores and damage zones in granite whose volumes coincide with those in IRPZ. This lithology contains high amount of U and Th (up to 4 ppm vol and 52 ppm vol respectively, see Table II. 2).

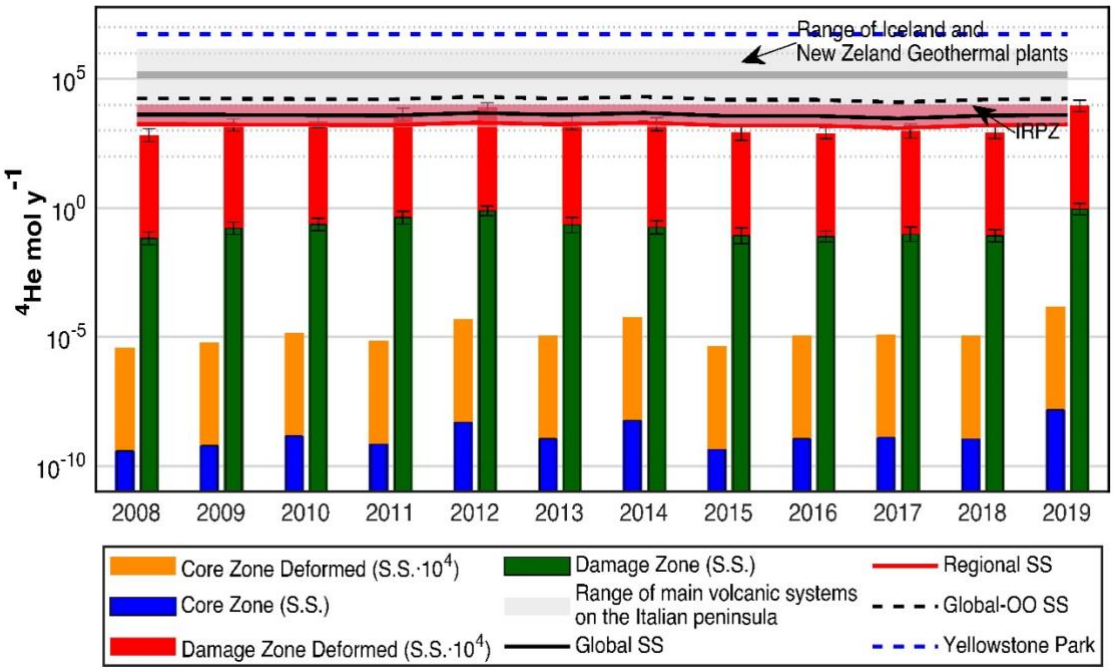

Figure II. 3: Variability of the crustal ^{4}He outputs in Gabbro. Output of crustal ^{4}He from faults cores and damage zones in gabbro whose volumes coincide with those in IRPZ. This lithology contains high amount of U and Th (up to 1 ppm vol and 3.5 ppm vol respectively, see Table II. 2).

II. 2.2 ^{4}He degassing in Non-Steady-State conditions

To estimate the crustal ^{4}He episodic release due to seismic activity, we applied eq. II. 2 to the volume related to the fault core and the damage zone (obtained from eq. II. 1 and eq. II. 2 respectively), by which we obtain the rate of ^{4}He release from fault core (Qfc,y) and damage zone (Qdz,y) (Table II. 1). Volatile release from the rock increases as a consequence of dilatancy, and in regions affected by active tectonics the flux of ^{4}He through the crust should be higher than in volume of rocks without deformation, where only a steady-state transport system is expected to act [27]. So, the release of ^{4}He from rock, which is affected by dilatancy, is from 10 to 10^4 times higher than that in un-deformed rock [32] (i.e., of Qfc,y and Qdz,y values, see Table II. 3).

Y	Qfc·10^4	Qdz·10^4		
		Median	Q1	Q3
2008	$3.88\cdot10^{-06}$	661.26	$3.70\cdot10^{02}$	$1.18\cdot10^{03}$
2009	$6.01\cdot10^{-06}$	1612.48	$9.33\cdot10^{02}$	$2.78\cdot10^{03}$
2010	$1.41\cdot10^{-05}$	2312.05	$1.33\cdot10^{03}$	$4.01\cdot10^{03}$
2011	$6.94\cdot10^{-06}$	4318.01	$2.36\cdot10^{03}$	$7.30\cdot10^{03}$
2012	$4.80\cdot10^{-05}$	7781.29	$4.96\cdot10^{03}$	$1.20\cdot10^{04}$
2013	$1.12\cdot10^{-05}$	2218.81	$1.08\cdot10^{03}$	$4.34\cdot10^{03}$
2014	$5.68\cdot10^{-05}$	1747.88	$9.79\cdot10^{02}$	$3.13\cdot10^{03}$
2015	$4.27\cdot10^{-06}$	853.47	$4.14\cdot10^{02}$	$1.68\cdot10^{03}$
2016	$1.11\cdot10^{-05}$	776.22	$4.74\cdot10^{02}$	$1.27\cdot10^{03}$
2017	$1.26\cdot10^{-05}$	947.47	$5.05\cdot10^{02}$	$1.78\cdot10^{03}$
2018	$1.10\cdot10^{-05}$	833.71	$4.89\cdot10^{02}$	$1.42\cdot10^{03}$
2019	$1.47\cdot10^{-04}$	9107.57	$5.31\cdot10^{03}$	$1.49\cdot10^{04}$

Table II. 3: Rate of ^{4}He in deformed volumes. Increased rate of ^{4}He (mol y^{-1}) from deformed fault core and rock damage zone volume.

II. 2.3 The Irpinia Seismic Network and Structural Setting

The Irpinia fault zone hosts a Near Fault Observatory, which is made up of a dense, high-dynamic range seismic network (the Irpinia Seismic Network, ISNet) constituted of 31 seismic stations installed along the Campania-Lucania Apennine chain and surrounding the fault system that generated the 1980, M 6.9, Irpinia earthquake (Fig. II. 4).

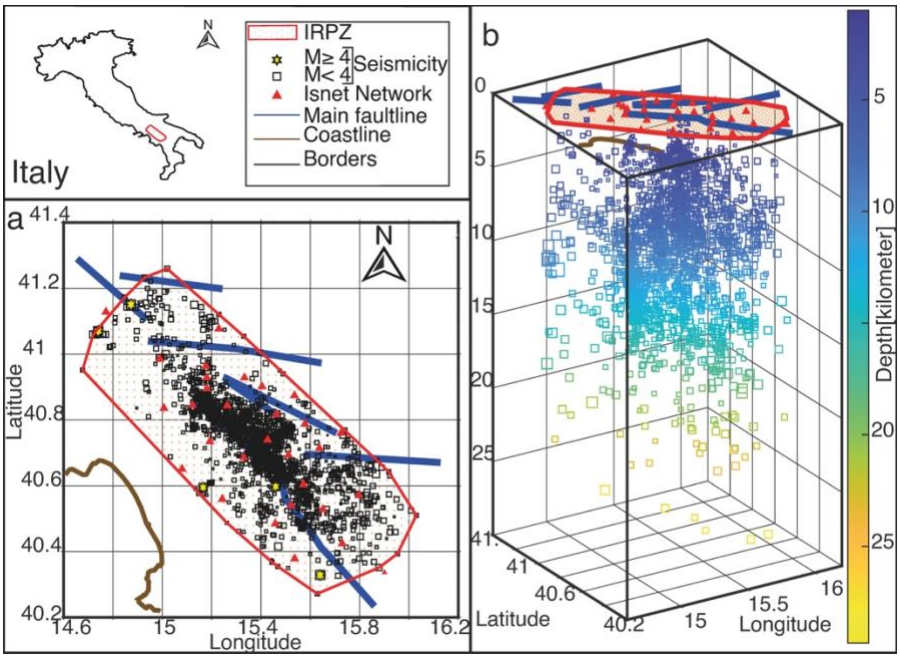

Figure II. 4: Seismic dataset recorded by ISNet seismic network in the IRPZ area (southern Italy). Distribution of earthquakes represented in map (a) and in 3D (b) with size varying according to magnitude and coloured per hypocentral depth. Historical events with larger magnitudes (M up to 7.0; Rovida et al., 2020[42]) are represented as yellow stars. ISNet seismic stations are shown as red triangles. Normal faults from the Database of Individual Seismogenic Sources (http://diss.rm.ingv.it/diss/) are shown as blue lines. The area considered in this study is limited by a red line.

ISNet is installed over an area of about 100 km x 70 km and it represents a natural laboratory for studying the faults evolution and rupture processes. The normal faults in Irpinia have a NW-SE strike and regulate the active tectonics in the thrust belt accommodating a regional extension of about 3 mm y^{-1} to 5 mm y^{-1} [43].

The structure of Southern Apennines is related to the Meso-Cenozoic tectonic processes that involved the African and European plates and which consisted of different phases of rifting, drifting and shortening that deformed the Corsica-Sardinia and Adriatic-Apulian forelands [40]. The Meso-Cenozoic succession of Adriatic-Apulian-African passive margin deposited as carbonate platforms with interposed pelagic basins that were involved in folding and thrusting according to imbricated structural units detached from their crystalline basement [44].

The geological units can be grouped according to their lithostratigraphic relationships as: 1) post-orogenic intra-mountain basin units of marine, terrestrial and volcanic origin, deposited during Plio-Pleistocene or Holocene in the Adriatic-Bradanic foredeep; 2) syntectonic top-thrust basin successions formed during the progressive shortening toward east; 3) orogenic wedge tectonic units involved in the NE-verging overthrusting from upper, internal domains (Tethyan oceanic crust or Adriatic-Apulian continental crust) to

the lower, external domains (Apennine carbonate platforms with inter-basins pelagic units); 4) Apulian carbonates, buried, deformed and over-thrusted in the inner belt and undeformed in the outcropping foreland [45]. Then, the Southern Apennine thrust belt was dissected during the Quaternary by NW-SE oriented normal faults that accommodated an extensional tectonic phase, according to a stress field with the axis of maximum extension coaxial to the axis of maximum compression of Apennines belt [46].

The hypocenters of the present-day earthquakes are distributed over a range of depths between about 2 km and about 20 km, with the higher density of events between around 7 km and 12 km, and laterally result confined within a 15 km to 20 km wide block, which is bounded by SW-NE boundary faults and includes the fault segments along which enucleated the M 6.9, 1980 earthquake.

II. 2.4 **Source parameters from a spectral decomposition approach**

During recent years, different studies investigated the source properties of microseismicity occurring the in Irpinia region [34,38,47–51]. Picozzi et al. (2019) studied the spatial distribution and temporal evolution of the apparent stress (τa)[34] considering near 2300 earthquakes. Here, we use the results obtained by Picozzi et al. (2021)[34], which have estimated the source parameters corner frequency, fc, seismic moment, M_0, stress drop, $\Delta\sigma$, and average slip $\widehat{D}$ by applying a generalized inversion technique[52] (GIT) for a set of about 3000 earthquakes with local magnitude between M 0 and M 4.2 occurred in the Irpinia region since the 2008. For the sake of readability, we refer mainly to Picozzi et al. (2017) [53] for the description of the analysis procedure and to Picozzi et al. (2021) [34] for details on the data processing and source spectra inversion results.

II. 2.5 **Fault Core volume calculation**

We consider the empirical relationship between fault displacement and the core thickness proposed by Torabi et al. (2019) [35] for carbonate rocks to compute a volume of fault core combining the two values in the following formula:

$$Vfc=\pi R^2 \cdot t \cdot 10^{-9} \text{ (in km}^3\text{)} \qquad \text{(eq. II. 3)}$$

Where R is the source radius, under the usual point source approximation where circular ruptures are assumed and t is the core thickness.

This value was calculated for each event and then, Matlab's retime function was applied to calculate the yearly sum and the results are reported in Table II. 5 and also shown in Fig. II. 5.

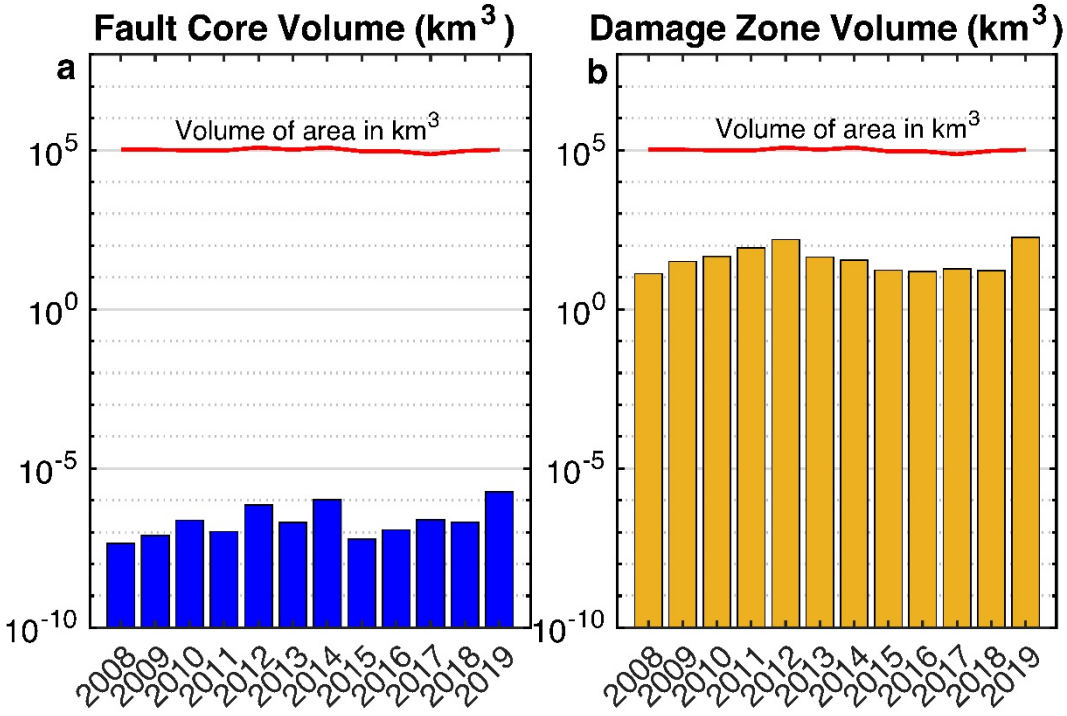

Figure II. 5: Volumes of the faults zone and IRPZ. a-2008-2019 year by year volumes of the faults core in IRPZ. **b**-2008-2019 year by year volumes of the damage zone in IRPZ. All the data and details of the calculations to compute these volumes are in section II. 2.5.

II. 2.6 Rock Damage zone volume calculation

We follow Jamtveit et al. (2018) [36] to estimate the total volume of rock damage associated to the microseismicity occurred in the Irpinia region during the period 2009 to 2019. Therefore, we implement the model proposed by Jamtveit et al. (2018) [36]. To this purpose, we consider the seismicity occurred each year and we compute the required parameters each one with mean and related standard deviation value (Table II. 4). In particular, we model the magnitude frequency distribution of the events through the Gutenberg and Richter relationship [54] and we estimate the *a* and *b* values (Table II. 4) using the maximum likelihood approach [55]. We use the source parameters information derived by Picozzi et al. (2021)[34] to estimate the coefficients *d* and *e* of a scaling relationship between the seismic potency and magnitude, as suggested by Ben-Zion and Zhu (2002) [56]. Moreover, relying on the rigidity modulus, μ, at the hypocenter location extracted from the 1D crustal model proposed for the Irpinia area [57], we estimate the uniform strain drop $\Delta\varepsilon$ (Ben-Zion,

2008) . All these parameters are finally used to compute Vdz and are reported in the Table II. 4.

Y	Magnitude (M)		a		b		Δ ε			e		d
	min	max	mean	σ	mean	σ	mean	σ	mean	σ	mean	σ
2008	0.9	3.5	2.66	0.5	-0.90	0.20	$8.74 \cdot 10^{-05}$	$6.70 \cdot 10^{-01}$	-1.44	$1.86 \cdot 10^{-03}$	1.49	$8.90 \cdot 10^{-04}$
2009	0.5	3.4	3.699	0.4	-0.90	0.20	$4.21 \cdot 10^{-05}$	$6.30 \cdot 10^{-01}$	-1.44	$1.86 \cdot 10^{-03}$	1.49	$8.90 \cdot 10^{-04}$
2010	0.8	4	6.269	0.5	-1.00	0.20	$5.17 \cdot 10^{-05}$	$5.40 \cdot 10^{-01}$	-1.44	$1.86 \cdot 10^{-03}$	1.49	$8.90 \cdot 10^{-04}$
2011	0.6	3.7	3.516	0.3	-0.80	0.10	$4.52 \cdot 10^{-05}$	$7.70 \cdot 10^{-01}$	-1.44	$1.86 \cdot 10^{-03}$	1.49	$8.90 \cdot 10^{-04}$
2012	0.8	4.4	2.78	0.3	-0.80	0.10	$6.48 \cdot 10^{-05}$	$5.50 \cdot 10^{-01}$	-1.44	$1.86 \cdot 10^{-03}$	1.49	$8.90 \cdot 10^{-04}$
2013	1.1	3.6	6.062	0.7	-0.90	0.30	$7.71 \cdot 10^{-05}$	$5.50 \cdot 10^{-01}$	-1.44	$1.86 \cdot 10^{-03}$	1.49	$8.90 \cdot 10^{-04}$
2014	0.9	4	5.639	0.5	-1.00	0.20	$7.71 \cdot 10^{-05}$	$6.10 \cdot 10^{-01}$	-1.44	$1.86 \cdot 10^{-03}$	1.49	$8.90 \cdot 10^{-04}$
2015	1	3.7	5.476	0.8	-1.00	0.30	$9.39 \cdot 10^{-05}$	$5.60 \cdot 10^{-01}$	-1.44	$1.86 \cdot 10^{-03}$	1.49	$8.90 \cdot 10^{-04}$
2016	1	3.6	8.011	0.4	-1.00	0.20	$1.07 \cdot 10^{-04}$	$4.80 \cdot 10^{-01}$	-1.44	$1.86 \cdot 10^{-03}$	1.49	$8.90 \cdot 10^{-04}$
2017	0.9	4.3	3.777	0.5	-1.00	0.20	$8.67 \cdot 10^{-05}$	$6.60 \cdot 10^{-01}$	-1.44	$1.86 \cdot 10^{-03}$	1.49	$8.90 \cdot 10^{-04}$
2018	0.8	3.8	5.583	0.5	-1.00	0.20	$9.47 \cdot 10^{-05}$	$5.40 \cdot 10^{-01}$	-1.44	$1.86 \cdot 10^{-03}$	1.49	$8.90 \cdot 10^{-04}$
2019	0.9	4.4	1.302	0.2	-0.70	0.10	$5.74 \cdot 10^{-05}$	$6.70 \cdot 10^{-01}$	-1.44	$1.86 \cdot 10^{-03}$	1.49	$8.90 \cdot 10^{-04}$

Table II. 4: Seismic parameters. Moment Magnitude (min and max yearly value) and Seismic parameters (mean value and standard deviation) are reported.

Therefore, we used the relationship proposed by Jamteviet et al., (2018) [3616] exspressed in the following formula to calculate the rock damage volume produced by crustal earthquakes in the magnitude range Mmin,y <M<Mmax,y (Jamtveit et al. 2018) [36], modified:

$$Vdz, y = Sy \cdot (\pi\gamma \left[\frac{7\cdot10^{-5}}{16\Delta\varepsilon}\right] 10^{a} \int_{M_{min,y}}^{M_{max,y}} 10^{(d-b)M+e} dM) \text{ in km}^3\text{ y}^{-1} \qquad \text{(eq. II. 4)}$$

where Sy is a surface of the area for the year y, Mmin,y and Mmax,y are the minimum and maximum magnitudes in the same year, respectively, and γ is a ratio of damage zone thickness to rupture radius (γ= 0.002) [36]. To consider the uncertainty of the parameters, the error has been propagated using a Monte Carlo approach and the median, first and third quartile are reported in Table II. 5.

Y	Fault Core	Damage Zone (km^3)			Surface of Area	Volume of Area
	km^3	Q1	Median	Q3	km^2	km^3
2008	$4.36\cdot10^{-08}$	7.32	13.09	23.29	$3.85\cdot10^{03}$	$1.04\cdot10^{05}$
2009	$7.99\cdot10^{-08}$	18.47	31.93	55.06	$3.80\cdot10^{03}$	$1.03\cdot10^{05}$
2010	$2.37\cdot10^{-07}$	26.31	45.78	79.33	$3.64\cdot10^{03}$	$9.84\cdot10^{04}$
2011	$1.05\cdot10^{-07}$	46.68	85.51	144.48	$3.58\cdot10^{03}$	$9.66\cdot10^{04}$
2012	$7.04\cdot10^{-07}$	98.17	154.09	236.79	$4.48\cdot10^{03}$	$1.21\cdot10^{05}$
2013	$2.03\cdot10^{-07}$	21.31	43.94	86.01	$3.79\cdot10^{03}$	$1.02\cdot10^{05}$
2014	$1.06\cdot10^{-06}$	19.39	34.61	62.02	$4.48\cdot10^{03}$	$1.21\cdot10^{05}$
2015	$5.97\cdot10^{-08}$	8.19	16.90	33.30	$3.39\cdot10^{03}$	$9.16\cdot10^{04}$
2016	$1.18\cdot10^{-07}$	9.39	15.37	25.14	$3.42\cdot10^{03}$	$9.24\cdot10^{04}$
2017	$2.47\cdot10^{-07}$	10.00	18.76	35.29	$2.74\cdot10^{03}$	$7.39\cdot10^{04}$
2018	$2.07\cdot10^{-07}$	9.68	16.51	28.19	$3.49\cdot10^{03}$	$9.42\cdot10^{04}$
2019	$1.88\cdot10^{-06}$	105.21	180.35	294.39	$3.78\cdot10^{03}$	$1.02\cdot10^{05}$

Table II. 5: Surface of Area of study and fault zone volume. Yearly value of surface of study area has been calculated by wrap events polygon tools in ZMAP toolbox [55] in Matlab, then the corresponding volume was obtained by multiplying for the regional crustal thickness (see Results and Discussion and Methods in the main text). Fault core (sum per year) and rock damage zone (median and interquartile range per year) has been calculated by Torabi et al. (2019) [35] and Jamtveit et al. (2018) [36] approach, respectively.

II. 2.7 **He isotopic signatures in IRPS's sites of Mefite D'Ansanto and San Sisto**

With the aim of studying the variability of He isotopic ratios, we processed data from the Mefite D'Ansanto and San Sisto sites covering samplings performed over 22 and 7 years, respectively (Table II. 6). A summary of the main statistical parameters is given in Table II. 7. The Fig. II. 6 shows how the values are essentially within the standard deviations. In addition, Dixon's outlier detection test confirms that the value remaining constant in observed time windows.

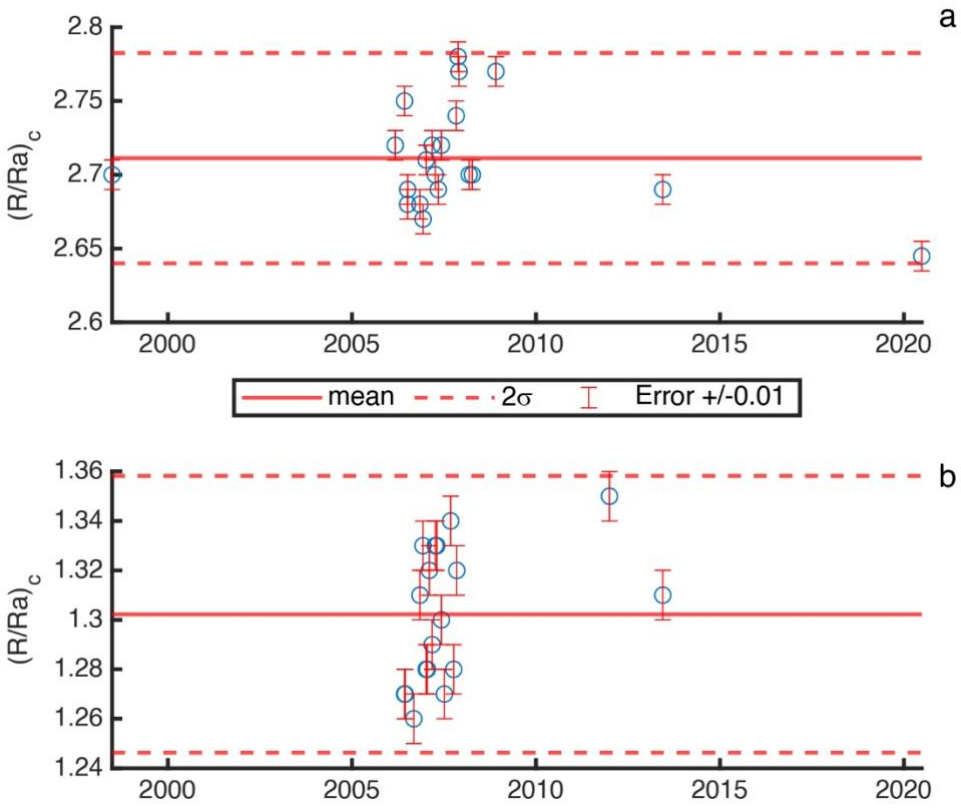

Figure II. 6: (R/Ra)c signature in IRPZ. Corrected R/Ra values in Mefite D'Ansanto (a) and San Sisto (b) In close to 20 years of observations.

Mefite D'Ansanto			San Sisto		
data	**(R/Ra)c**	**References**	**data**	**(R/Ra)c**	**References**
26/06/98	2.70	(22)	06/06/06	1.27	(23)
06/03/06	2.72	(23)	13/06/06	1.27	(23)
06/06/06	2.75	(23)	06/09/06	1.26	(23)
06/07/06	2.68	(23)	06/11/06	1.31	(23)
06/11/06	2.68	(23)	06/12/06	1.33	(23)
07/12/06	2.67	(23)	07/01/07	1.28	(23)
07/01/07	2.71	(23)	18/01/07	1.28	(23)
07/03/07	2.72	(23)	07/02/07	1.32	(23)
07/04/07	2.70	(23)	07/03/07	1.29	(23)
07/05/07	2.69	(23)	07/04/07	1.33	(23)
07/06/07	2.72	(23)	23/04/07	1.33	(23)
07/07/06	2.69	(23)	07/06/07	1.30	(23)
01/11/07	2.74	(23)	07/07/07	1.27	(23)
20/11/07	2.78	(23)	07/09/07	1.34	(23)
29/11/07	2.77	(23)	07/10/07	1.28	(23)
09/03/08	2.70	(23)	07/11/07	1.32	(23)
09/04/08	2.70	(23)	01/01/12	1.35	(24)
29/11/08	2.77	(23)	13/06/13	1.31	(23)
13/06/13	2.69	(23)			
26/06/20	2.64	this work			

Table II.6: Corrected R/Ra of Mefite D'Ansanto and San Sisto. Nearly 20 years observations of values of (R/Ra)c in the gases emitted from the two high flux CO_2 natural gas emissions in IRPZ, Mefite D'Ansanto and San Sisto sites respectively. Notes: (R/Ra)c is the He isotopic ratio, as R/Ra, corrected atmospheric contamination. All the analytical procedures and instrumentation of the analysis of the Mefite D'Ansanto single sample from this study are the same those in Buttitta et al (2020) [27].

Statistics	Mefite (R/Ra)c	San Sisto (R/Ra)c
No. of observations	20	18
Minimum	2.645	1.260
Maximum	2.780	1.350
1st Quartile	2.690	1.280
Median	2.700	1.305
3rd Quartile	2.725	1.328
Mean	2.711	1.302
Variance (n-1)	0.001	0.001
Standard deviation (n-1)	0.036	0.028
Dixon's test output		
***p*-value (bilateral)**	0.675	0.942
99% confidence interval *p*-value:	]0.673; 0.676[	] 0.941; 0.943 [

Table II. 7: Descriptive statistics and Dixon's test output of corrected R/Ra data. Statistical summary of (R/Ra)c data of Mefite D'Ansanto and San Sisto.

II. 3 RESULTS AND DISCUSSION

Here, we exploit the role of low magnitude earthquakes (M<4) on He degassing in continental regions by computing the variability of the crustal ^{4}He output over time for the seismogenic volumes of rock associated with a 12-year-long earthquake catalogue.

This study considered the Irpinia fault zone (hereafter IRPZ) in central-southern Apennine (Italy) (Fig. II. 4), a region affected by major deformational processes in terms of active displacements and seismogenic processes that have led to high-magnitude disastrous earthquakes (i.e. M=6.4 in 1561, M=6.9 in 1694, M=5.7 in 1826, M=5.9 in 1853, M=7.0 in 1857), with the most recent being the M=6.9 Irpinia earthquake in 1980 [58], which occurred along NW-SE trending normal faults. This latter large event occurred as a complex rupture process involving multiple segments (mostly with dip ~60° eastward) [58]. Due to the complexity of the tectonics[40] and the occurrence of strong earthquakes, the IRPZ can be considered one of the most hazardous seismic areas in the Mediterranean region.

During the last 10 years, seismicity in the IRPZ has been monitored in real time by the Irpinia Near Fault Observatory (https://www.epos-eu.org/tcs/near-fault-observatories), which also includes the Irpinia Seismic Network (ISNet; http://isnet.fisica.unina.it). The ISNet represents a natural laboratory for studying fault evolution and rupture processes.

In this study we analysed a 12-year-long earthquake catalogue (from 2008 to 2019) of distributed seismicity in an area of approximately 3,700 km^2 (ca. 80 km × 46 km). The larger magnitude events during this 12-year-period have ranged from M=3.4 (in 2009) to M=4.4 (in 2012 and 2019).

The hypocentres of the present-day earthquakes appear to be spread over a large crustal volume around the fault segments that generated the M=6.9 Irpinia earthquake in 1980, spanning depths from 2 to 20 km (Fig. II. 4), with a higher density of events at around 7 km and 12 km in carbonate lithology (Fig. II. 4).

This sector of central-southern Apennine that coincides with the IRPZ is characterized by the outgassing of volatiles of deep origin, and CO_2 is the dominant gaseous species [59–61]. Notwithstanding that the region is far from active volcanism (>70 km), the He isotopic ratio ($^3He/^4He$) in the high-flux CO_2 emissions is extremely variable, and peaks at 2.9 Ra (Ra is the $^3He/^4He$ value in the atmosphere) [61–63]. The contribution of the air-derived He is negligible in all these gas emissions in IRPZ. This peak value (2.9 Ra) is lower than the typical mantle He isotopic signature (6.3 Ra for subcontinental lithospheric mantle) [64] and is markedly higher than the typical crustal radiogenic signature (0.01–0.05 Ra) [65], which clearly indicates the presence of mantle-derived He in the IRPZ that is diluted by variable contributions of crust-derived ^4He. Furthermore, high crustal radiogenic ^4He outputs have also been computed for the IRPZ (up to 3.74×10^4 mol y^{-1}) [65] that cannot be explained using the steady-state model of the whole-crust production and release, the latter being up to 4 orders of magnitude lower. This evidence clearly implies that tectonics control the transfer of the volatiles in this seismically active sector of central-southern Italy [61,62,65], where they play an active role in regional seismicity [8], making this region ideal for investigating the relationship between earthquakes and He degassing. Furthermore, the He isotopic signatures in natural fluids here have been constant over about 20 years of observations, indicating that the mixing of mantle-crust fluids is not perturbed during long interseismic period (section II. 2.7)

At the global scale, the crustal ^4He flux from continental regions is 3×10^{10} atoms m^{-2} s^{-1}, with a variability of a factor 2X [22]. We computed the year-by-year steady-state degassing in the IRPZ (section II. 2.1) assuming (1) U and Th contents in the rocks of the whole crust in the IRPZ of 0.3–1.6 and 0.2–6.1 ppm, respectively [41] (Table II. 2) and (2) a regional crustal thickness of 27 km [66]. The annual crustal steady-state ^4He flux in the IRPZ ranges from 8.7×10^9 to 2.5×10^{10} atoms m^{-2} s^{-1}, where the highest value overlaps

the range of the worldwide continental flux (3×10^{10} atoms m^{-2} s^{-1}, with a twofold variability) [22]. The corresponding annual output from the whole crust in the IRPZ ranges from 1.2×10^{3} to 4.8×10^{3} mol y^{-1} (Table II. 1).

We also focused on faults that nucleate earthquakes in the IRPZ. We computed the volumes of both the fault cores and the damage zones of the seismogenic faults, starting from the catalogue of the earthquake source parameters obtained [34] for the ~2300 earthquakes that occurred during 2008–2019 (section II. 2.5). The volume of the fault core (Vfc) was calculated for each event, and then the annual sum was computed, which yielded Vfc values ranging from 4.4×10^{-8} km^3 (sum of Vfc in 2008) to 1.9×10^{-6} km^3 (sum of Vfc in 2019). These values are orders of magnitude lower that the annual whole-crust volume of the IRPZ (the volume that contains all the hypocentres of the annual seismicity), which ranged from 7.4×10^{4} km^3 in 2018 to 1.2×10^{5} km^3 in 2012 (Fig. II. 5). The steady-state degassing in the core zone varies over two orders of magnitude, being between 3.9×10^{-10} and 1.5×10^{-8} mol y^{-1} (Fig. II. 7). However, this is 11–13 orders of magnitudes lower than the steady-state values in the IRPZ (1.2×10^{3} to 4.8×10^{3} mol y^{-1}; Fig. II. 7). Considering that the amount of ^{4}He released from a deformed volume of rock is up to 10^4 times higher than the steady-state value for the same volume of rock [23,32], even if the fault core is intensely deformed, the contribution of the fault-core crustal ^{4}He to its regional degassing is still negligible, at up to 1.5×10^{-4} mol y^{-1} (Fig. II. 7).

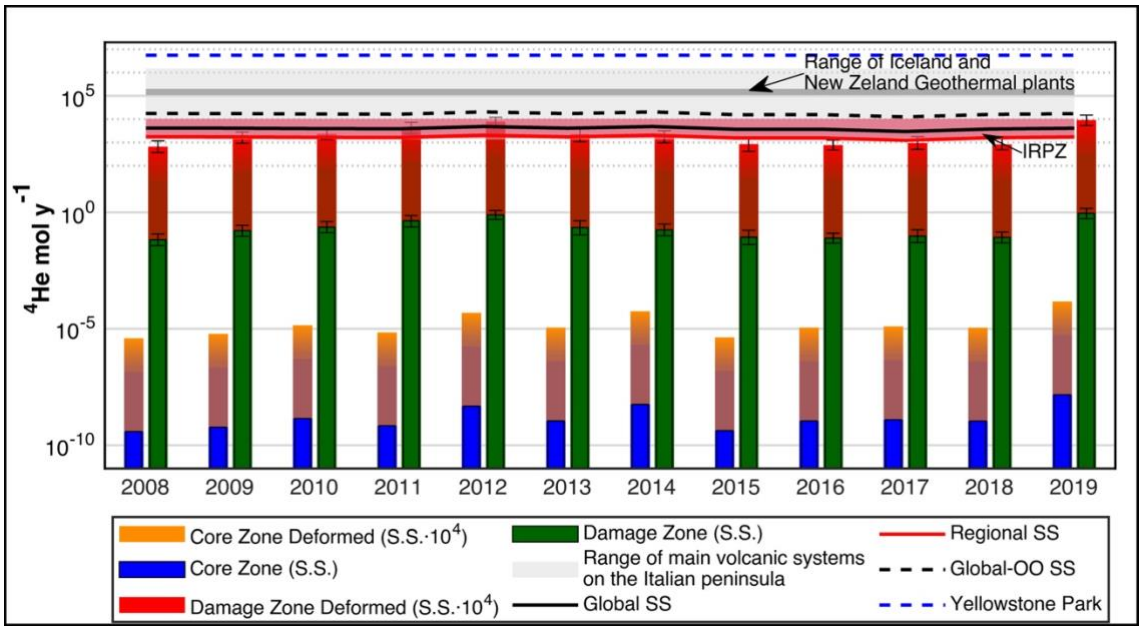

Figure II. 7: Variability of the crustal ^{4}He outputs Annual output (2008-2019) of the crustal ^{4}He output (steady state) across the surfaces defined by earthquakes epicentres in IRPZ. These values of the crustal ^{4}He output are computed by using 1) the U and Th concentrations in the regional lithology, 2) the areas of the annual epicentres and 3) the crustal thickness below IRPZ (all the data and the equations used in the computations are in sections II. 2.3 to II. 2.6). For comparison, we also computed the annual steady state output (2008-2019) of the crustal ^{4}He in IRPZ by using the typical range of the U and Th concentrations in the continental crust (Table II. 2). The blue columns represent the steady state annual output of crustal ^{4}He from the volumes of rocks that characterize the IRPZ faults cores. Here we used the U and Th concentrations of the lithology that constitute the faults cores (Table II. 2). The orange columns are the maximum annual output (up to 10^4 the steady state values) from the same volume of rocks that constitute the faults cores. The green columns represent the annual steady-state output of crustal ^{4}He from the IRPZ damage zones. Here we used the U and Th concentrations of the lithology that constitute the damage zones (Table II. 2). The red columns are the maximum annual output from the same volume of rocks that constitute the damage zones (up to 10^4 the steady state values). The ^{4}He output at the Yellowstone Park are from Lowenstern et al., (2014) [24]. The mantle ^{4}He output the New Zealand and Iceland volcanic-related geothermal fields and the Italian volcanic systems are computed by the CO_2 outputs [42], the mantle C/^{3}He ratios [40], and the ^{3}He/^{4}He ratio of these area [62,67–69].

In contrast, the estimated volume of the IRPZ damage zone ranges from 13.1 to 1.8×10^2 km^3, which is up to seven orders of magnitude higher than that of the fault core (Fig. II. 5). The steady-state output of crustal ^{4}He from the IRPZ damage zone varies from 0.1 to 0.9 mol y^{-1}(Table II. 2), which is even lower than the regional steady-state whole-crust IRPZ degassing rate (1.2 to 2.0×10^3 mol y^{-1}) (Fig. II. 7). It is worth noting that annually there is a tenfold variability in the absence of high-magnitude earthquakes (M<4.4), supporting the impulsive nature of crustal ^{4}He degassing associated with the nucleation of earthquakes even in absence of high-magnitude

earthquakes in the IRPZ. Furthermore, considering the maximum release of ^{4}He from the volume of the damage zone due to rock deformation (up to 10^4 times the steady-state release) [23,32], the annual degassing rate between 2008 and 2019 for the damage zone is up to 0.9×10^4 mol y^{-1}. This value is equal to or higher than the regional steady-state degassing rate from the whole non-deformed crust in the IRPZ (Fig. II.7). Hence, it should be noted that seismicity in the IRPZ is mainly concentrated within the limestones, which are U- and Th-poor lithology (Table II. 2). Therefore, notwithstanding (1) a low crustal ^{4}He production due to the low amount of U and Th in the seismogenic volume of rocks and (2) an absence of high-magnitude earthquakes, the degassing rate of crustal ^{4}He from the seismogenic IRPZ crust, which is so high because of the intense deformation of the rock that increase the release of ^{4}He from the rock, (Fig. II. 7) can be at least equal to that due to the whole and undeformed IRPZ continental crust (Fig. II.7).

Considering a damage zone involving U- and Th-rich rocks, such as granite and gabbro that are typical in continental regions (4 and 52 ppm U and 1 and 3.5 ppm Th) [70], and assuming a volumetric expansion of the damage zone as for the IRPZ, the output of crustal ^{4}He would be up to ~10^6 and ~10^5 mol y-1, respectively (Figs. II. 2 and II. 3). Therefore, a volume of granitic crust in a strongly deformed state can degas up to ~10^7 moles of crustal ^{4}He over 10 years. This amount of outgassing would correspond to ~56% of the crustal ^{4}He degassed during the disastrous earthquake in Kobe in 1995 (1.8×10^7 mol) and to ~1.8% of the worldwide steady-state global degassing (5.4×10^8mol y^{-1}) [29].

It is worth noting that the values of crustal ^{4}He released from a damage zone in granitic rock overlap the high value of crustal ^{4}He output from the large high-temperature geothermal systems worldwide (e.g. Iceland, New Zealand) and the active volcanoes of the systems of the southern of Italy (Fig. II. 7). However, these values are still lower than the prodigious emission of crustal ^{4}He at Yellowstone National Park, where crustal metamorphism induced by a deep hotspot liberates the ^{4}He that has accumulated over more than 2.5 billion years [24]. This evidence strongly reinforces the present finding that earthquake nucleation plays an active role in the impulsive nature of crustal ^{4}He degassing even in the absence of high-magnitude earthquakes.

In this scenario, crustal ^{4}He from the seismogenic rock volumes (Fig. II. 7) strongly contributes to diluting the mantle-derived He that has been recognized in worldwide regions associated with high-magnitude earthquakes (e.g. San Andreas fault, USA; southwest Japan; Anatolian fault, Turkey; Belice valley, Italy) [20,30,71–73]. According to our

results, the contribution from earthquake-related crustal ^{4}He varies over time and is dependent upon the extension of fault zones, their lithology and the earthquake magnitude. These findings highlight that seismicity plays an active role in the high variability of the He isotopic signature in seismic zones, and they contribute quantitatively to explaining this variability over short distances along different sectors of faults [4,20,61,73]. Hence, our results clearly indicate that an increase of the crustal ^{4}He component over time can shift the He isotopic signature in the natural fluids released in seismic regions towards a radiogenic endmember (0.01–0.05 Ra), which is indicative of changes in the crustal stress, and hence provides hints about the preparatory phases of large earthquakes.

II. 4 REFERENCES

1. Ozima, M., Korenaga, J. & Yin, Q.-Z. *The Earth: Its Birth and Growth*. (Cambridge University Press, 2012).
2. Fischer, T. P. & Aiuppa, A. AGU centennial grand challenge: Volcanoes and deep carbon global CO 2 emissions from subaerial volcanism—recent progress and future challenges. *Geochem. Geophys. Geosyst.* **21**, e2019GC008690 (2020).
3. Tamburello, G., Pondrelli, S., Chiodini, G. & Rouwet, D. Global-scale control of extensional tectonics on CO 2 earth degassing. *Nat. Commun.* **9**, 4608 (2018).
4. Caracausi, A. & Sulli, A. Outgassing of Mantle Volatiles in Compressional Tectonic Regime Away From Volcanism: The Role of Continental Delamination. *Geochem. Geophys. Geosyst.* **20**, 2007–2020 (2019).
5. Miller, S. a. *et al.* Aftershocks driven by a high-pressure CO2 source at depth. *Nature* **427**, 724–727 (2004).
6. Girault, F. *et al.* Persistent CO2 emissions and hydrothermal unrest following the 2015 earthquake in Nepal. *Nat. Commun.* **9**, 1–10 (2018).
7. Luccio, F. D. *et al.* Seismic signature of active intrusions in mountain chains. *Science Advances* **4**, 1–10 (2018).
8. Chiodini, G. *et al.* Carbon dioxide Earth degassing and seismogenesis in central and southern Italy. *Geophys. Res. Lett.* **31**, (2004).
9. Chiodini, G. *et al.* Correlation between tectonic CO2 Earth degassing and seismicity is revealed by a 10-year record in the Apennines, Italy. *Science Advances* **6**, eabc2938 (2020).
10. Ozima, M. & Podosek, F. A. *Noble Gas Geochemistry: 2nd edition*. 286 (Cambridge University Press; 2 edition (December 24, 2001), 2002).
11. Mukhopadhyay, S. Early differentiation and volatile accretion recorded in deep-mantle neon and xenon. *Nature* **486**, 101–104 (2012).
12. Caracausi, A., Avice, G., Burnard, P. G., Füri, E. & Marty, B. Chondritic xenon in the Earth's mantle. *Nature* **533**, 82–85 (2016).
13. Broadley, M. W. *et al.* Identification of chondritic krypton and xenon in Yellowstone gases and the timing of terrestrial volatile accretion. *Proc. Natl. Acad. Sci. U. S. A.* **117**, 13997–14004 (2020).

14. Italiano, F., Martinelli, G., Bonfanti, P. & Caracausi, A. Long-term (1997-2007) geochemical monitoring of gases from the Umbria-Marche region. *Tectonophysics* **476**, 282–296 (2009).
15. Paonita, A., Caracausi, A., Iacono-Marziano, G., Martelli, M. & Rizzo, A. Geochemical evidence for mixing between fluids exsolved at different depths in the magmatic system of Mt Etna (Italy). *Geochim. Cosmochim. Acta* **84**, 380–394 (2012).
16. Paonita, A. *et al.* Intense overpressurization at basaltic open-conduit volcanoes as inferred by geochemical signals: The case of the Mt. Etna December 2018 eruption. *Science Advances* **7**, eabg6297 (2021).
17. Sano, Y. *et al.* Helium anomalies suggest a fluid pathway from mantle to trench during the 2011 Tohoku-Oki earthquake. *Nat. Commun.* **5**, 1–6 (2014).
18. Sano, Y. *et al.* Ten-year helium anomaly prior to the 2014 Mt Ontake eruption. *Sci. Rep.* **5**, 13069 (2015).
19. O'Nions, R. K. & Oxburgh, E. R. Heat and helium in the earth. *Nature* **306**, 429–431 (1983).
20. Boles, J. R., Garven, G., Camacho, H. & Lupton, J. E. Mantle helium along the Newport-Inglewood fault zone, Los Angeles basin, California: A leaking paleo-subduction zone. *Geochem. Geophys. Geosyst.* **16**, 2364–2381 (2015).
21. Aggarwal, P. K. *et al.* Continental degassing of 4He by surficial discharge of deep groundwater. *Nat. Geosci.* **8**, 35–39 (2015).
22. Torgersen, T. Continental degassing flux of 4He and its variability. *Geochem. Geophys. Geosyst.* **11**, 1–15 (2010).
23. Ballentine, C. J. & Burnard, P. G. Production, Release and Transport of Noble Gases in the Continental Crust. *Rev. Mineral. Geochem.* **47**, 481–538 (2002).
24. Lowenstern, J. B., Evans, W. C., Bergfeld, D. & Hunt, A. G. Prodigious degassing of a billion years of accumulated radiogenic helium at Yellowstone. *Nature* **506**, 355–358 (2014).
25. Bauer, S. J., Gardner, W. P. & Lee, H. Release of radiogenic noble gases as a new signal of rock deformation. *Geophys. Res. Lett.* **43**, 10,688-10,694 (2016).
26. Bauer, S. J., Gardner, W. P., Heath, J. E., Payton Gardner, W. & Heath, J. E. Helium release during shale deformation: Experimental validation. *Geochem. Geophys. Geosyst.* **17**, 2612–2622 (2016).

27. Buttitta, D. *et al.* Continental degassing of helium in an active tectonic setting (northern Italy): the role of seismicity. *Sci. Rep.* **10**, 162 (2020).
28. Honda, M., Kurita, K., Hamano, Y. & Ozima, M. Experimental studies of He and Ar degassing during rock fracturing. *Earth Planet. Sci. Lett.* **59**, 429–436 (1982).
29. Sano, Y., Takahata, N., Igarashi, G., Koizumi, N. & Sturchio, N. C. Helium degassing related to the Kobe earthquake. *Chem. Geol.* **150**, 171–179 (1998).
30. Sano, Y. *et al.* Groundwater helium anomaly reflects strain change during the 2016 Kumamoto earthquake in Southwest Japan. *Sci. Rep.* **6**, 37939 (2016).
31. Billi, A., Salvini, F. & Storti, F. The damage zone-fault core transition in carbonate rocks: implications for fault growth, structure and permeability. *J. Struct. Geol.* **25**, 1779–1794 (2003).
32. Torgersen, T. & O'Donnell, J. The degassing flux from the solid earth: Release by fracturing. *Geophys. Res. Lett.* **18**, 951–954 (1991).
33. Collettini, C. *et al.* Fault weakening due to CO_2 degassing in the Northern Apennines: short- and long-term processes. *Geological Society, London, Special Publications* **299**, 175–194 (2008).
34. Picozzi, M. *et al.* Spatiotemporal Evolution of Microseismicity Seismic Source Properties at the Irpinia Near-Fault Observatory, Southern Italy. *Bull. Seismol. Soc. Am.* **112**, 226–242 (2022).
35. Torabi, A., Johannessen, M. U. & Ellingsen, T. S. S. Fault Core Thickness: Insights from Siliciclastic and Carbonate Rocks. *Geofluids* **2019**, (2019).
36. Jamtveit, B., Ben-Zion, Y., Renard, F. & Austrheim, H. Earthquake-induced transformation of the lower crust. *Nature* **556**, 487–491 (2018).
37. Thakur, P., Huang, Y. & Kaneko, Y. Effects of low-velocity fault damage zones on long-term earthquake behaviors on mature strike-slip faults. *J. Geophys. Res. [Solid Earth]* **125**, (2020).
38. Picozzi, M., Bindi, D., Zollo, A., Festa, G. & Spallarossa, D. Detecting long-lasting transients of earthquake activity on a fault system by monitoring apparent stress, ground motion and clustering. *Sci. Rep.* **9**, 16268 (2019).
39. Rovida, A. *et al.* CPTI15, the 2015 version of the Parametric Catalogue of Italian Earthquakes. Istituto Nazionale di Geofisica e Vulcanologia. doi:http://doi.org/10.6092/ingv.it-cpti15. (2016).

40. Liu, W. *et al.* Formation time of gas reservoir constrained by the time-accumulation effect of 4He: Case study of the Puguang gas reservoir. *Chem. Geol.* **469**, 246–251 (2017).
41. Coltorti, M. *et al.* U and Th content in the Central Apennines continental crust: A contribution to the determination of the geo-neutrinos flux at LNGS. *Geochim. Cosmochim. Acta* **75**, 2271–2294 (2011).
42. Rovida, A., Locati, M., Camassi, R., Lolli, B. & Gasperini, P. The Italian earthquake catalogue CPTI15. *Bull. Earthquake Eng.* **18**, 2953–2984 (2020).
43. Active tectonics of the Adriatic region from GPS and earthquake slip vectors. doi:10.1029/2008JB005860.
44. Merlini & Mostardini. Appennino centro-meridionale: sesioni geologiche e proposta di modello strutturale. *Geologia dell'Italia centrale* (1986).
45. Ghisetti, F. & Vezzani, L. Normal faulting, transcrustal permeability and seismogenesis in the Apennines (Italy). *Tectonophysics* **348**, 155–168 (2002).
46. Doglioni, C. Geological remarks on the relationships between extension and convergent geodynamic settings. *Tectonophysics* **252**, 253–267 (1995).
47. Cantore, L., Oth, A., Parolai, S. & Bindi, D. Attenuation, source parameters and site effects in the Irpinia–Basilicata region (southern Apennines, Italy). *J. Seismol.* **15**, 375–389 (2011).
48. Stabile, T. A., Satriano, C., Orefice, A., Festa, G. & Zollo, A. Anatomy of a microearthquake sequence on an active normal fault. *Sci. Rep.* **2**, 410 (2012).
49. Zollo, A., Orefice, A. & Convertito, V. Source parameter scaling and radiation efficiency of microearthquakes along the Irpinia fault zone in southern Apennines, Italy. *J. Geophys. Res. [Solid Earth]* **119**, 3256–3275 (2014).
50. Festa, G. *et al.* Insights into Mechanical Properties of the 1980 Irpinia Fault System from the Analysis of a Seismic Sequence. *Geosci. J.* **11**, 28 (2021).
51. Wyss, M. & Brune, J. N. Seismic moment, stress, and source dimensions for earthquakes in the California-Nevada region. *J. Geophys. Res.* **73**, 4681–4694 (1968).
52. Castro, R. R., Anderson, J. G. & Singh, S. K. Site response, attenuation and source spectra of S waves along the Guerrero, Mexico, subduction zone. *Bull. Seismol. Soc. Am.* **80**, 1481–1503 (1990).
53. Picozzi, M., Oth, A., Parolai, S. & Bindi, D. Accurate estimation of seismic source parameters of induced seismicity by a combined approach of generalized inversion

and genetic algorithm: Application to The …. *Journal of* (2017) doi:10.1002/2016JB013690.

54. Gutenberg, B. & Richter, C. F. Earthquake magnitude, intensity, energy, and acceleration. *Bull. Seismol. Soc. Am.* **32**, 163–191 (1942).
55. Wiemer, S. A software package to analyze seismicity: ZMAP. *Seismol. Res. Lett.* **72**, 373–382 (2001).
56. Ben-Zion & Zhu. Potency-magnitude scaling relations for southern California earthquakes with 1.0<ML<7.0. *Geophys. J. Int.* (2002).
57. Ben-Zion, Y. Collective behavior of earthquakes and faults: Continuum-discrete transitions, progressive evolutionary changes, and different dynamic regimes. *Rev. Geophys.* **46**, (2008).
58. Bernard, P. & Zollo, A. The Irpinia (Italy) 1980 earthquake: Detailed analysis of a complex normal faulting. *J. Geophys. Res.* **94**, 1631 (1989).
59. Di Luccio, F. *et al.* Seismic signature of active intrusions in mountain chains. *Sci Adv* **4**, e1701825 (2018).
60. Improta, L., De Gori, P. & Chiarabba, C. New insights into crustal structure, Cenozoic magmatism, CO2degassing, and seismogenesis in the southern Apennines and Irpinia region from local earthquake tomography: seismic tomography of Apennines. *J. Geophys. Res. [Solid Earth]* **119**, 8283–8311 (2014).
61. Italiano, F., Martelli, M., Martinelli, G. & Nuccio, P. M. Geochemical evidence of melt intrusions along lithospheric faults of the Southern Apennines, Italy: Geodynamic and seismogenic implications. *J. Geophys. Res. [Solid Earth]* **105**, 13569–13578 (2000).
62. Caracausi, A., Martelli, M., Nuccio, P. M., Paternoster, M. & Stuart, F. M. Active degassing of mantle-derived fluid: A geochemical study along the Vulture line, southern Apennines (Italy). *J. Volcanol. Geotherm. Res.* **253**, 65–74 (2013).
63. Nuccio, P. M., Caracausi, A. & Costa, M. Mantle-derived fluids discharged at the Bradanic foredeep/Apulian foreland boundary: The Maschito geothermal gas emissions (southern Italy). *Mar. Pet. Geol.* **55**, 309–314 (2014).
64. Gautheron, C., Moreira, M. & Allègre, C. He, Ne and Ar composition of the European lithospheric mantle. *Chem. Geol.* **217**, 97–112 (2005).
65. Caracausi, A. & Paternoster, M. Radiogenic helium degassing and rock fracturing: A case study of the southern Apennines active tectonic region. *J. Geophys. Res. [Solid Earth]* **120**, 2200–2211 (2015).

66. Di Stefano, R., Bianchi, I., Ciaccio, M. G., Carrara, G. & Kissling, E. Three-dimensional Moho topography in Italy: New constraints from receiver functions and controlled source seismology. *Geochem. Geophys. Geosyst.* **12**, (2011).
67. Cardellini, C. *et al.* Monitoring diffuse volcanic degassing during volcanic unrests: the case of Campi Flegrei (Italy). *Sci. Rep.* **7**, 6757 (2017).
68. Marty, B. *et al.* An evaluation of the C/N ratio of the mantle from natural CO2-rich gas analysis: Geochemical and cosmochemical implications. *Earth Planet. Sci. Lett.* **551**, 116574 (2020).
69. Martelli, M. *et al.* Helium-strontium isotope constraints on mantle evolution beneath the Roman Comagmatic Province, Italy. *Earth Planet. Sci. Lett.* **224**, 295–308 (2004).
70. Schön, J. *Physical Properties of Rocks: A Workbook*. (Elsevier, 2011).
71. Doğan, T. *et al.* Adjacent releases of mantle helium and soil CO2from active faults: Observations from the Marmara region of the North Anatolian Fault zone, Turkey. *Geochem. Geophys. Geosyst.* **10**, (2009).
72. Caracausi, A. *et al.* Active geodynamics of the central Mediterranean Sea: Tensional tectonic evidences in western Sicily from mantle-derived helium. *Geophys. Res. Lett.* **32**, 1–5 (2005).
73. Kulongoski, J. T. *et al.* Volatile fluxes through the Big Bend section of the San Andreas Fault, California: Helium and carbon-dioxide systematics. *Chem. Geol.* **339**, 92–102 (2013).

CHAPTER III: *Deep fluid degassing from the crust: a model of the gas-rock and water interactions in the Contursi hydrothermal system (southern Italy)*

III.1 INTRODUCTION CHAPTER III

Deep sourced volatiles (e.g., He, CO_2) outgas extensively in active tectonic areas[1–8]. The latter process can be explained by considering that tectonic discontinuities are regions of enhanced porosity and permeability.[9,10]. Overpressure of volatiles along fault planes has been observed to play a crucial role in the nucleation of earthquakes[7,11]. At the same time, the physicochemical processes during earthquake nucleation are recorded and transferred to the surface by fluids migrating through the fault core[12,13].

Large changes in fluid migration can result from tiny alterations in rock characteristics, like small-scale heterogeneities[14]. In particular, the contrast in grain sizes can limit migration rates and increase trapped volumes by 10-10^2 times[14].

Likewise, the stability of the lower crust and during periods when internal reworking predominates, it is possible that the deep crustal carbon's source may have changed over time[15].

Consequently, the geochemical monitoring of natural fluids in seismic regions can be also crucial for understanding processes leading to catastrophic earthquakes and as well to constraints on budget of volatiles in atmosphere[9,16–18].

Nevertheless, it must be considered that in shallow crustal layers (e.g., aquifer and fault zones) groundwater intercepts the deep volatiles (crustal vs. mantle) migrating to the atmosphere[19,20]. Some of the latter (the non-reactive noble gases) are directly transported to the surface[21], while others (the reactive; e.g., CO_2), once dissolved within the water, can interact with solutes and aquifer-rocks modifying their abundances and pristine isotopic compositions[8,22,23] before to reach the surface. In this scenario, the emerging groundwater carries a memory of processes at depth (e.g., mixing, water-gas-rock interaction). Hence, to figure out the processes at depth that control the chemistry of the fluids, it is crucial to reconstruct local and regional models based on different geochemical tools (e.g., volatiles outputs, water chemistry, dissolved gases in water, isotopic geochemistry). Some of the processes controlling the chemistry of fluids can be

influenced by the earthquake nucleation, as for instance variations in permeability that modify the mixing of fluids of different origin (crustal vs mantle) or the flux of deep volatiles (CO_2) to the aquifers.

Two decades of geochemical investigations along the Apennines in Italy[1–3,6,7,17,19,24–27]have highlighted a relationship between the transfer of fluids through the crust and seismicity at regional scales. This is also supported by geophysical investigations along the Apennines that recognize 1) the presence of fluids in correspondence of the fault planes of seismogenetic faults[28] 2) the overpressure of fluids at depth able to generate aftershocks[11] and 3) the role of the groundwater recharge in modulating crustal deformation and seismicity[29]. These evidences pose great attention to the paleo-fluids trapped in minerals and veins along the faults[10,13,30] to investigate the physic-chemical processes occurring at microscale along the fault planes and the adjacent regions (e.g., the damage zones) and to infer the characteristics of processes controlling the chemistry of fluids along faults prone to generate high magnitude earthquakes.

Here we present results of a detailed study of gas-water and rock interaction in the thermal basin of Contursi and the surrounding area (Fig. III. 1, south of Italy) based on the TDIC vs $\delta^{13}C_{TDIC}$ relationship. This sector of the Apennine is dominated by extensional tectonic and characterized by high output of deep CO_2[7] coupled to mantle derived helium[26,31,32]. Within a 30 km radius degassing site of Mefite D'Ansanto , the largest no-volcanic emission of CO_2 (2000 tons day^{-1} [33]) occurs where the He isotopic signature overlaps those at Vesuvio and Phlegrean Fields[26], the two active volcanic systems close to Naples.

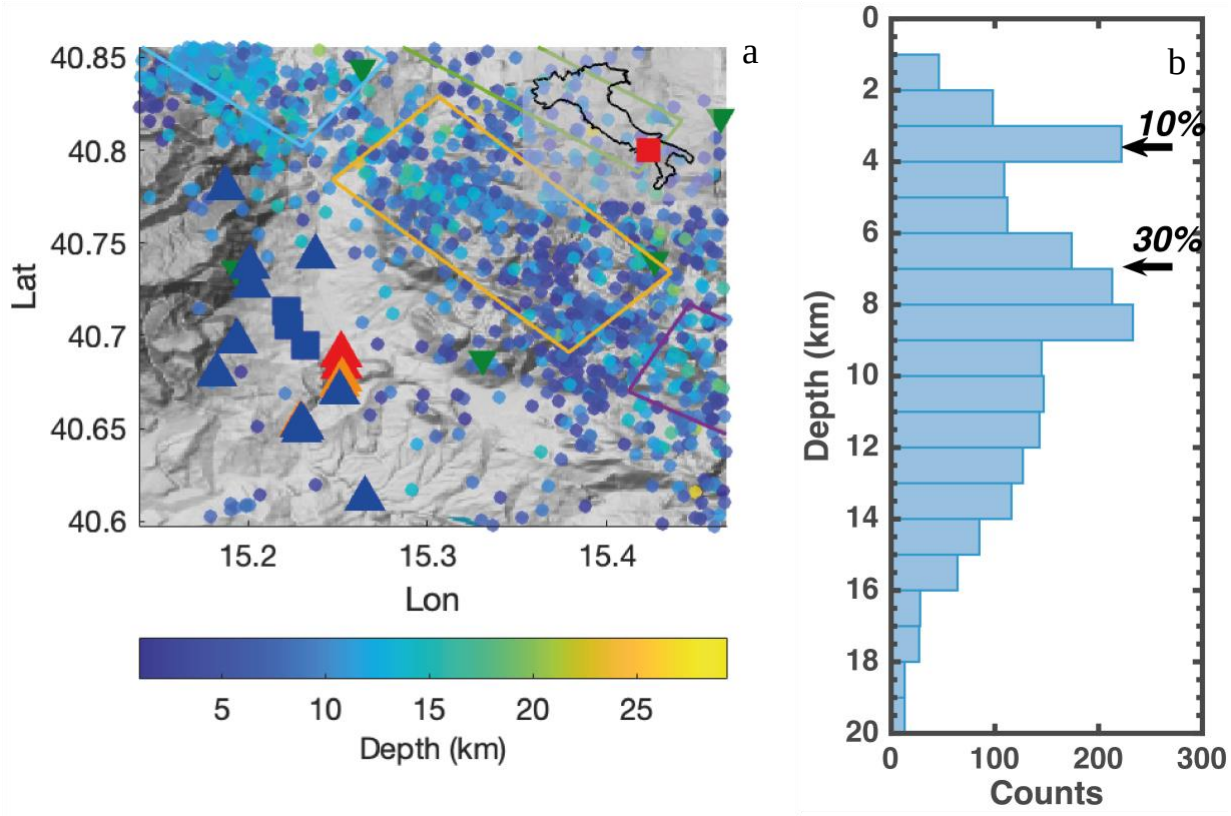

Figure III. 1: Sampling sites and distribution of seismicity in Irpinia fault zone (southern Italy). (a) Location of sampled cold waters (blue triangles), thermal and ipotermal water (red and orange triangles respectively) and free gases (blue squares) in Contursi area and seismicity recorded by ISNet (inverted green triangles) during the years 2009 through 2019 (http://isnet-bulletin.fisica.unina.it/cgi-bin/isnet-events/isnet.cgi). Normal faults from the Database of Individual Seismogenic Sources (http://diss.rm.ingv.it/diss/) are shown as blue lines. (b) Bimodal distribution of n° of earthquakes. In the Irpinia fault zone the 10% of seismicity is located between 3 to 4 km, roughly the bottom of shallow reservoir, and the 30% of seismicity is located between 6 to 9 km, roughly the top of deeper reservoir. (c) Shallow seismicity is characterized by M<=3, while the most intensive seismicity in the area (4<=M<=4.4) is located between 6 to 12 km coinciding with the as-pressurized rock volumes developed under the Apulia Platform.

Furthermore, in 1980 a catastrophic earthquake occurred in the region (M=6.9), the recent seismicity is generally M≤4.4 and multidisciplinary studies of the regional seismicity are in the context of the Irpinia Near Fault Observatory (https://www.epos-eu.org/tcs/near-fault-observatories).

In our study, we investigate the origin of the deep CO_2 at regional scale and the gas-water-rock interaction that control the carbon abundances and isotopic composition in the groundwater. We also model the Carbon (C) sinks (e.g., C-mineral precipitation, CO_2 exsolution) and we quantify the leakage of C from the groundwater, in order to compute the deep carbon outputs associated with the groundwater. We propose a simple model that describes the behaviour of the deep inorganic carbon from its source to the atmosphere, which can help to choose the parameters to be monitored in a future regional

geochemical surveillance and to provide a geochemical model for interpreting possible geochemical variation related to local high magnitude earthquakes.

III. 2 STRUCTURAL SETTING OF SOUTHERN APENNINES AND SEISMICITY

The structure of the Southern Apennines is related with the Meso-Cenozoic tectonic processes that involved African and European plates. The different tectonic phases of rifting, drifting, and shortening that occurred with time, lead the backbone of the Apennines to have a E-NE verging, duplexes geometries and out-of-sequence thrusting, mainly due to orogenic contraction that was active since upper Eocene-Oligocene Miocene up to late Pliocene[34].

From the lithostratigraphic point of view, the Irpinia region is characterized, from top to bottom, by: (1) post-orogenic intramountain basin units of marine, terrestrial, and volcanic origin, deposited during Plio-Pleistocene or Holocene in the Adriatic-Bradanic foredeep; (2) syntectonic top-thrust basin successions formed during the progressive shortening toward east; (3) orogenic wedge tectonic units involved in a NE-verging overthrusting from upper, internal domains (Tethyan oceanic crust or Adriatic-Apulian continental crust) to the lower, external domains (Apennine carbonate platforms with inter-basins pelagic units); (4) Apulian carbonates, buried, deformed, and overthrusted in the inner belt and undeformed in the outcropping foreland[35,36].

Since Quaternary, the southern Apennine thrust belt is dissected by NW-SE oriented normal faults that accommodate extensional tectonic (i.e., 3–5 mm•yr^{-1}) as evidenced by surface geology, borehole breakout, and available fault plane solutions of earthquakes[37].

In the past, southern Apennines were hit by earthquakes up to X-XI MCS intensity, making them one of the highest seismic hazard region in the Mediterranean, with segmented, seismogenic structures capable of generating up to M 7 earthquakes. Large earthquakes nucleate here within the first 10–15 km of the crust and have typically recurrence periods ≥1000 yr.

It is worth noting that normal faults dissecting the Apennines show evolutionary trends from young, high-angle planar faults, seated in the upper crust and characterized by small extensional strains, to mature, listric faults reaching the crystalline basal detachment with high amount of extensional strain[38]. Furthermore, the origin of large earthquakes within

this tectonic context is believed being associated with the presence of fluids within the crust that can reach over-pressure conditions at depths around 10 km depths due to the low permeability of the rock formations that inhibit their circulation[39].

The 1980, Ms 6.9, Irpinia earthquake occurred along NW-SE trending normal faults, and it was the most destructive, instrumentally recorded earthquake of the Southern Apennines. This earthquake was characterized by a complex rupture process involving multiple fault segments[40].

After the 1980 event, no large earthquakes have again struck the area. The present-day seismicity is characterized by low-magnitude seismicity (Ml <3.5) with hypocentral depth mostly limited within the first 15 km. Fault plane solutions show normal and normal-strike slip kinematics (Festa et al., 2021), confirming the dominant SW–NE extensional regime. The background low magnitude seismicity appears to be spread into a large volume (Figure III. 1), and the related stress field is closely linked with the major fault segments activated during the 1980 Irpinia earthquake. In addition, microseismicity seems to be controlled by high pore pressure of water-saturated Apulian carbonates within a fault-bounded crustal volume[29,41,42]. The presence of crustal fluids represent a fundamental issue to be considered in hazard studies, considering the strong relationship that emerged between seismicity and high-fluid pressure during the recent strong earthquakes in the Apennines (e.g., the Mw 6.0, 1997 Colfiorito earthquake and the Mw 6.3, 2009 L'Aquila earthquake).

In the Irpinia area, tomographic images reveal two kinds of reservoirs[39]. A low-Vp/Vs dome-shaped body, 20 km long and 15 km wide, is located between 6 km and 11 km depth underneath Mount Forcuso, in the northern part of Irpinia. This geophysical evidence is interpreted as a deep, pressurized CO_2-rich rock volume, filled below the Apulian platform carbonates by fluid-rich mantle melts intruded into the crust[39]. This anomaly correlates with high heat flow values (100–215 mW/m2) observed along the Mount Forcuso antiform and with geochemical data. Active faults in Irpinia region control the gas leakage from the crust, influencing also the leakage areas distribution at the surface. Significant nonvolcanic CO_2-rich gas emission principal expression is observed at Mefite d'Ansanto degassing site, where deep, mantle-related fluids are released through the active faults[33].

In the central portion of the Irpinia area (i.e., approximately within the Marzano segment in which the 1980 earthquake nucleated), tomographic images[39,43] show a high Vp/Vs

broad region between 4 km and 6 km which is interpreted as fractured, fluid-saturated carbonates.

The physical modeling of 3D velocity images[44] lead to estimate a porosity of carbonates in the Marzano segment around 4%-5% and a fluid composition consisting of brine–CO_2 and/or CH_4 –CO_2. The occurrence of pressure changes in fluid-filled cracks within carbonates is considered one of the main trigger mechanisms of microearthquakes in the Irpinia region.

The Contursi hydrothermal system is placed within the Sele river valley, between the two fault segments of Marzano (where the 1980 earthquake nucleated) and the Cervialto one. The reconstruction of the rupture evolution occurred during the 1980 Irpinia earthquake proposed a gap in the slip distribution exactly in correspondence of the Sele Valley[45]. Furthermore, Picozzi et al. (2022)[41] observed for the Sele river valley sector high b-value of the Gutenberg-Richter frequency magnitude distribution, suggesting the presence of fluids capable of influencing the occurrence of microseismicity. This sector might play as extensional transfer zone between the Marzano and Cervialto fault segments, a tectonic issue still under investigation but that well agrees with the presence of the Contursi hydrothermal system.

3 SAMPLING AND ANALYTICAL PROCEDURES

We collected hot and cold waters in natural springs and wells in the thermal basin of Contursi and the surrounding areas between 2021 and 2022. Moreover, we also collected free gases in high flux CO_2 gas emissions (Figs. III.1a, III. 2 and Table III.1). Among the studied emissions, all the springs have gas bubbling in water, S. Sisto and Oliveto Citra 1-2, are dry mofettes. Gaseous samples were collected in pyrex bottles with vacuum valves at both ends, taking care to prevent air contamination, by using a steel funnel and a three-direction valve and a syringe.

Gaseous samples were collected in pyrex bottles with vacuum valves at both ends, taking care to prevent air contamination, by using a steel funnel and a three-direction valve and a syringe (Figure III. 2).

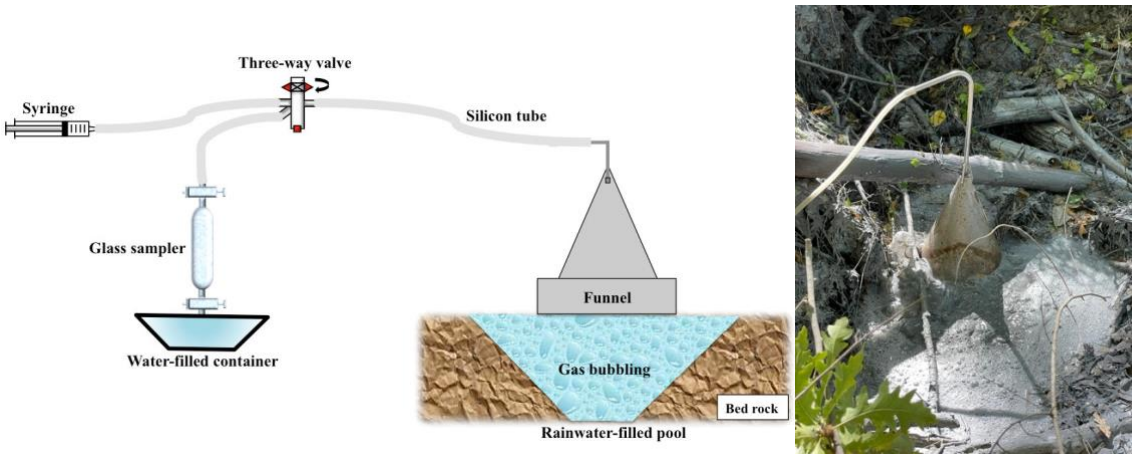

Figure III. 2: Schematic illustration showing the sampling system used for collecting the free gaseous manifestations

Free and dissolved gases in water were analysed for their chemical (O_2, N_2, CH_4, He, and CO_2) and isotopic composition ($^3He/^4He$, $\delta^{13}C_{CO2}$). Chemical and isotopic analyses of fluids were performed at Istituto Nazionale di Geofisica e Vulcanologia (INGV—Palermo). Dissolved and free gases were analysed by a double detector (TCD-FID) Perkin Elmer Autosystem XL gas chromatograph using Ar as carrier gas and a 4 m Carboxen 1000 column. Dissolved gases were analysed according to the method proposed by Capasso and Inguaggiato (1998)[46].

The chemical and isotopic ($^3He/^4He$, $\delta^{13}C_{CO2}$) analyses are reported in Table III. 2. The $^3He/^4He$ were measured in a split-flight-tube mass spectrometer (GVI Helix SFT). Ion beams of ^3He and ^4He were simultaneously detected by a double collector system that yielded isotopic ratio precision within ±0.5%. Purified atmospheric helium was used as a running standard. A multicollector Thermo-Helix MC Plus mass spectrometer was used to measure ^{20}Ne and after the gas mixture was purified according to standard practices utilizing cryogenic traps, the $^{13}C/^{12}C$ ratios of CO_2 (expressed as $^{13}\delta C\text{-}CO_2$ in ‰ versus the V-PDB standard) were measured with a Finnigan Delta S mass spectrometer with a precision of ±0.1‰.

III. 4 RESULTS AND DISCUSSION

In total, measurements were made on twenty-three spring samples and two free gas samples. The sample's location, temperature, pH, measurements, and principal element

are reported in Table III. 1. The bulk gas composition, $\delta^{13}(CO_2)$ values, helium, neon, and argon concentrations, as well as their isotope ratios, are all detailed in Table III. 2.

III. 4.1 Bulk gas concentrations, $\delta^{13}(CO_2)$ water measurements and Noble gas data

All Thermal (T water between 34.3 and 49 °C) an Ipothermal (Temperature water between 17.3 and 26.4 °C) spring gas samples are CO_2 dominant with less amount of N_2 (range from 1.10 to 8.66 ccSTP/L) and O_2 (range from 0.04 to 0.16 ccSTP/L) and trace of CH_3 (from $4.63 \cdot 10^{-5}$ to $8.56 \cdot 10^{-2}$ ccSTP/L), CO (up to $2.63 \cdot 10^{-4}$ ccSTP/L) and the remaining percentage was made up of noble gases. In the cold spring (T<15 °C) the CO_2 up to 141.02 ccSTP/L, only in PSA site the N_2 is the major constituent (8.52 ccSTP/L). pH ranges from 6.1 to 8.4. Total dissolved solids (TDS) values range from 3.46 to 71.04 mm/L (Table III. 3), in the cold water we find the lowest value (up to 28.57 mm/L). The concentration of CO_2 in the free gases sites (OV1-2 and SST) range

	Sample Name	Sample ID	Date	Latitude	Longitude	T (°C)	EC (mS/cm)	pH	Eh (mV)	Q (L/s)	Na (mmol/L)	K (mmol/L)	Mg (mmol/L)	Ca (mmol/L)	NO_3 (mmol/L)	F (mmol/L)	Cl (mmol/L)	SO_4 (mmol/L)	HCO_3 (mmol/L)
Cold Waters	Acquara ponticchio	AQP	03/05/21	15.188	40.780	7.8	354	7.8	272.4	100	0.17	0.04	0.30	1.96	0.02	0.00	0.16	0.03	4.10
	Piceglia Alta	PSA	03/05/21	15.201	40.737	7.9	300	7.7	252.7	-	0.14	0.03	0.42	1.38	0.02	0.00	0.14	0.03	3.75
	fiumicello	FIU	03/05/21	15.202	40.727	9.7	298	8.4	206.5	40	0.17	0.04	0.50	1.20	0.02	0.00	0.16	0.03	3.50
	S Oronzo	SRON	03/05/21	15.194	40.697	10.1	352	7.8	301.8	20	0.21	0.04	0.35	1.85	0.03	0.00	0.19	0.04	4.05
	Senerchiella	SEN	03/05/21	15.238	40.742	10.5	518	7.4	298.7	2000	0.26	0.05	0.61	2.31	0.04	0.01	0.22	0.06	5.85
			24/01/22	15.238	40.742	10.6	514	7.4											
	Magliana	MAG	03/05/21	15.182	40.679	12.1	398	7.5	178.3	10	0.33	0.04	0.08	2.42	0.07	0.00	0.27	0.06	4.50
	Sorgente la regina (basso tanagro)	REG	03/05/21	15.265	40.612	12.8	664	7.2	299.0	5590	0.56	0.08	0.72	3.03	0.07	0.01	0.52	0.12	7.10
			24/01/22	15.265	40.612	12.9	680	7.2											7.10
	Acetosella	ACT	03/05/21	15.231	40.650	13.8	1054	6.8	198.0	5	0.95	0.14	1.04	5.98	0.05	0.01	0.82	0.17	12.55
	DonCarlo	DC	03/05/21	15.230	40.649	14.1	1090	6.5	85.8	50	0.94	0.14	0.94	6.07	0.05	0.01	0.81	0.17	12.65
	Fontana Prete	FP	03/05/21	15.251	40.670	14.3	613	7.5	166.3	0.1	0.59	0.03	0.23	3.31	0.01	0.01	0.55	0.15	6.35
	CantaniMix	CAM	03/05/21	15.229	40.651	14.4	1298	6.6	213.6	70	1.32	0.17	1.06	7.37	0.03	0.01	1.14	0.22	14.90
	Ferrata	FR	04/05/21	15.229	40.652	14.7	1435	6.5	228.9	0.7	1.80	0.20	1.27	8.23	0.03	0.01	1.48	0.27	16.41
Ipothermal waters	Cantani solfurea	CAS	04/05/21	15.228	40.653	17.3	1981	6.1	-197.3	100	3.83	0.34	1.97	11.34	0.00	0.02	2.88	0.42	22.76
	Forlenza	FOR	05/05/21	15.230	40.652	18.5	1924	6.3	-147.8	500	4.88	0.42	2.04	10.17	0.01	0.01	3.86	0.54	20.76
	Tufaro	TUF	04/05/21	15.251	40.674	24.8	2770	6.2	-197.5	-	9.74	1.04	1.83	11.36	-	0.06	11.20	2.48	23.71
	Cappetta Nuova	CAN	04/05/21	15.252	40.676	26.4	2560	6.3	-219.2	-	9.13	0.79	3.55	21.98	0.01	0.08	9.04	4.21	23.51
	Cappetta Vecchia	CAV	04/05/21	15.252	40.676	26.4	2570	6.3	-224.5	50	8.96	1.08	1.66	10.68	0.00	0.06	7.11	1.69	22.71
Thermal waters	CapassoVenere	VEN	05/05/21	15.251	40.690	34.3	5240	6.2	-273.9	-	26.84	2.53	3.52	15.95	-	0.10	28.97	4.99	36.01
	RosaPepe Fredda	RSF	04/05/21	15.185	40.683	36.8	4460	6.2	-273.2	60	19.07	2.33	3.88	6.21	0.04	0.03	22.44	2.77	23.51
	RosaPepe Calda	RSC	04/05/21	15.185	40.683	37.5	4640	6.3	-258.5	40	19.33	1.93	3.23	15.19	0.07	0.08	21.70	2.65	36.46
			24/01/22	15.185	40.683	38.4	4640	6.2											
	CapassoGeyser	GEY	04/05/21	15.251	40.690	46.4	6380	6.4	-285.0	13	43.30	3.98	5.47	7.20	-	0.07	47.79	3.35	26.11
			24/01/22	15.251	40.690	48.4	6520	6.4											
	CapassoErcole	ERC	05/05/21	15.252	40.690	47	6470	6.4	-263.0	-	46.22	3.90	5.24	14.92	-	0.09	41.92	4.05	38.51
			24/01/22	15.252	40.690	49	6430	4.4											38.51

Table III.1: Physical data and chemical compositions of the sprins

Sample Name	Sample ID	Date	Gas Type	He (ccSTP/L)	H_2 (ccSTP/L)	O2 (ccSTP/L)	N_2 (ccSTP/L)	CO (ccSTP/L)	CH4 (ccSTP/L)	CO2 (ccSTP/L)	$\delta^{13}C_{TDIC}$	$^4He/^{20}Ne$	R/Ra	(R/Ra)c
Acquara ponticchio	AQP	03/05/21	Dissolved								-11.44			
Piceglia Alta	PSA	03/05/21	Dissolved	b.d.l.	1.51E-03	8.52	19.93	3.54E-05	6.55E-05	2.28	-10.42			
fiumicello	FIU	03/05/21	Dissolved								-			
S Oronzo	SRON	03/05/21	Dissolved								-			
Senerchiella	SEN	03/05/21	Dissolved	2.22E-04	1.35E-04	7.19	17.37	2.06E-05	1.25E-05	14.90	-5.65			
		24/01/22		2.27E-04	1.87E-03	5.76	12.05	0.00E+00	0.00E+00	14.03		1.07	1.40	-
Magliana	MAG	03/05/21	Dissolved								-			
Sorgente la regina (basso tanagro)	REG	03/05/21	Dissolved	4.45E-04	0.00E+00	5.10	19.16	0.00E+00	3.29E-05	25.44	-4.72			
		24/01/22		9.70E-04	1.90E-03	3.86	14.44	0.00E+00	4.53E-05	27.61		3.53	1.32	-
Acetosella	ACT	03/05/21	Dissolved								-			
DonCarlo	DC	03/05/21	Dissolved	1.71E-04	1.94E-04	4.09	10.07	2.08E-05	2.42E-05	141.02	-1.74			
Fontana Prete	FP	03/05/21	Dissolved	b.d.l.	1.64E-04	4.38	15.63	2.63E-05	2.61E-04	21.58	-14.71			
CantaniMix	CAM	03/05/21	Dissolved								-			
Ferrata	FR	04/05/21	Dissolved								-			
Cantani solfurea	CAS	04/05/21	Dissolved	2.91E-04	b.d.l.	0.07	8.66	0.00E+00	8.56E-02	557.93	0.47	1.51	1.07	-
Forlenza	FOR	05/05/21	Dissolved	b.d.l.	b.d.l.	0.04	2.87	0.00E+00	8.58E-03	546.70	1.52			
Tufaro	TUF	04/05/21	Dissolved	b.d.l.	b.d.l.	0.06	2.27	0.00E+00	1.33E-02	595.07	2.02			
Cappetta Nuova	CAN	04/05/21	Dissolved	b.d.l.	b.d.l.	0.09	4.59	1.73E-05	3.70E-03	471.26	2.18	0.49	0.87	-
Cappetta Vecchia	CAV	04/05/21	Dissolved								-			
CapassoVenere	VEN	05/05/21	Dissolved	b.d.l.	b.d.l.	0.06	1.87	2.63E-04	7.94E-04	578.22	3.67			
RosaPepe Fredda	RSF	04/05/21	Dissolved	b.d.l.	1.32E-04	0.10	4.81	4.71E-05	2.87E-04	403.60	3.63	0.63	0.64	-
RosaPepe Calda	RSC	04/05/21	Dissolved	b.d.l.	3.21E-04	0.12	1.60	0.00E+00	1.46E-03	1096.29	-			
		24/01/22		2.57E-05								0.53	0.91	-
CapassoGeyser	GEY	04/05/21	Dissolved	b.d.l.	5.60E-04	0.10	3.02	5.10E-05	1.73E-03	459.47	3.55	0.42	0.95	-
		24/01/22		3.88E-05	9.33E-04	0.16	2.80	0.00E+00	1.51E-03	951.96		0.51	0.90	-
CapassoErcole	ERC	05/05/21	Dissolved	b.d.l.	7.78E-04	0.12	4.22	0.00E+00	1.43E-04	492.44	3.02			
		24/01/22		b.d.l.	1.20E-03	0.15	1.10	1.44E-04	4.63E-05	1007.87		0.53	0.84	-

		Date		He (ppm)	H2 (ppm)	O2 (%)	N2 (%)	CO (ppm)	CH4 (ppm)	CO2 (%)	$\delta^{13}C_{CO2}$	$^4He/^{20}Ne$	R/Ra	(R/Ra)c
Oliveto Citra-1	OV1	24/01/22	Free	22.55	3.1	0.1	3.35	0.5	0.3699	95.32	0.86	215.16	1.27	1.27 (0.008)
			Free	25.00		0.15	3.31		0.3871	94.86		263.68	1.28	1.28 (0.007)
Oliveto Citra-2	OV2	24/01/22	Free	21.00	381	0.0203	2.68	3245	0.3245	94.87				
			Free	20.00	92	0.0397	2.39	10	0.3345	95.69		284.44	1.28	1.28 (0.007)
San Sisto	SST		Free	17.30	98.00	0.12	2.65		0.29	96.92	0.70	48.66	1.41	1.41 (0.008)

Table III.2: Chemical and isotopic composition ($\delta^{13}C$ and $^3He/^4He$) of the dissolved and free gases. The analytical uncertainty was <3% for chemical analysis, below 0.3% for He and Ne and 0.1% for C isotope composition. In the free gase samples, He isotopic ratio is corrected for the contribution of atmospheric He and reported as Rc/Ra, by using the approach proposed by Sano et al., (1987). The Rc/Ra of free gas sites range from 1.27± 0.01 (OV1) to 1.41 ± 0.01 (SST). In water samples (both cold and hot), the elementary ratio $^4He/^{20}Ne$ is less than 3. In this case, the Rc/Ra differ significantly from the measured $^3He/^4He$ ratios which would make the correction erroneous (according to Sano et al., 2006[47]) therefore its $^3He/^4He$ values are reported uncorrected and range from 0.64 (RSF) to 1.40 (SEN) Ra.

from 94.86 to 96.92 %, with the remainder of gas predominately constituting of N_2 (up to 3.5 %), O_2 (up to 0.15 %), and traces of CH_4 and CO, 0.4 and 3245 ppm respectively.

The $\delta^{13}C_{TDIC}$ value in the cool water range from -14.71 to -1.74‰. In the thermal and ipothermal water this value is positive and range from 0.47 to 3.67‰.

The elemental and isotopic compositions of noble gases (e.g., He, Ne and Ar) constitute a set of non-reactive geochemical tracers. The inert nature, low terrestrial abundance, and well-characterized isotopic composition of noble gases in the mantle, crust, hydrosphere, and atmosphere enhance their utility as geochemical tracers of crustal fluids[48,49]. For twelve sites, we determined the abundances of elemental and isotopic ratios of He, Ar and Ne. The noble gases in our samples varies according to the type of site. In cold and isothermal water, the He range from $1.71 \cdot 10^{-04}$ to $9.70 \cdot 10^{-04}$ ccSTP/L, in thermal water range from $2.57 \cdot 10^{-05}$ to $3.88 \cdot 10^{-05}$ ccSTP/L (about an order less than cold and isothermal water) and in the free gases range from 17.30 to 25.00 ppm. (Table III. 2).

The noble gas composition in natural fluids is derived from three primary sources: the mantle, atmosphere and crust[49]. A very useful tool for discriminating the contributions of the different sources of He in natural fluids is analysing the correlation between the $^3He/^4He$ and $^4He/^{20}Ne$ ratios, using the approach proposed by Sano and Wakita (1985)[50]. Because mantle and crust-derived gases contain less neon than the atmosphere, the $^4He/^{20}Ne$ serves as a sensitive proxy for distinguishing contributions originating in the mantle or crust (i.e. He) from those entrained through groundwater and/or air mixing (e.g. ^{20}Ne)[51].

In the free gas samples, the $^4He/^{20}Ne$ ratios range from 48.66, in San Sisto site, to 284.44, in Oliveto Citra site (see Table III. 2). These values greatly exceed (by 153–892 times) the $^4He/^{20}Ne$ expected for atmospheric value (0.319)[52]indicating negligible atmospheric helium (less than 0.6%). In contrast, the highest $^4He/^{20}Ne$ ratio in the dissolved gases in water is 3.54, which is 12 time the ratio in air-saturated water ASW= 0.285 at 25°C[52]. The low $^4He/^{20}Ne$ of the dissolved gases (Fig. III. 3) indicate they are dominated by the atmospheric component, in fact the $^4He/^{20}Ne$ ratios are not resolvable from atmospheric ratios. It is noteworthy that the lowest $^4He/^{20}Ne$ ratios are in thermal water samples (RSF, RSC, GEY, ERC). The free gas in the area, San Sito and Oliveto Citra1-2, are characterised by a strong crustal component, about 80%, and only the remaining 20% is related to the mantle component. A high concentration of radiogenic He does not necessarily indicate a shallow crust origin. In fact, as in some active tectonic sectors of the central Italy, the local seismicity can induce an excess of crustal He flux, which can be higher than the flux due to a steady-state degassing[25,26] and thus act as a masking effect with regard to

the contribution of mantle-derived Helium. Unfortunately, the elevated atmospheric contamination of He in the groundwater does not allow realistic assumptions to be made about the origin of He and the associated dissolved gases in these waters.

The He isotopic ratios $^3He/^4He$ are reported normalised to the value of air (where 1 Ra is the atmospheric ratio of $1.382 \pm 0.005 \cdot 10^{-6}$ [53]). In our samples, it ranges from 0.64 (RSF) to 1.41 (SEN) Ra, consistent with atmospheric origin of the `noble gases.

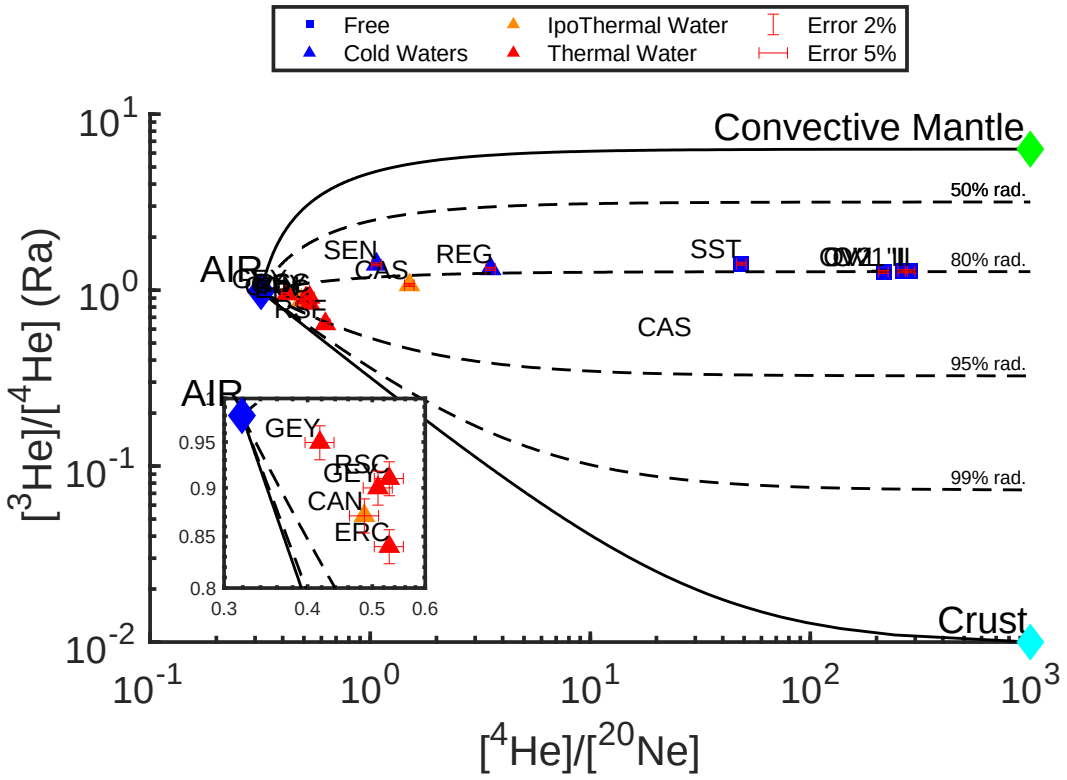

Figure III.3: A correlation diagram between the $^3He/^4He$ and $^4He/^{20}Ne$ ratios for the springs and free gases investigated. Solid lines depict binary mixing between air ($^3He/^4He$ = 1Ra, $^4He/^{20}Ne$=0.319[52]) the Sub Continental Lithospheric Mantle (SCLM, $^3He/^4He$= 6.32 ± 0.39 Ra[54], $^4He/^{20}Ne$>10^3 [50]), crustal end-member ($^3He/^4He$=0.01-0.05 Ra[55], $^4He/^{20}Ne$>10^3 [50]). In the main figure the errors are smaller than the symbols.

The combination of the amount of CO_2, its carbon isotopes ($\delta^{13}C_{CO2}$) and He in natural fluids is commonly used to identify the presence of mantle volatiles even far from active and quiescent volcanic systems[8,18]. ^3He is not produced in significant amounts in the crust, so low $^3He/^4He$ ratios (typically 0.01 or 0.02 Ra) and associated $CO^2/^4He$ ratios greater than $1.4 \cdot 10^2$ are usually associated with a crustal CO_2 source[56]. In a $CO_2/^4He$ vs R/Ra plot (Fig. III. 4), our samples are fitted along a mixing line between the SCLM and a local crustal end-member and their low dispersion is probably due to the negligibility of effects such as loss of CO_2 or assimilation of crustal ^4He (shift to the left) and/or addition of crustal CO_2 or degassing in open system (shift to the right)[8,22].

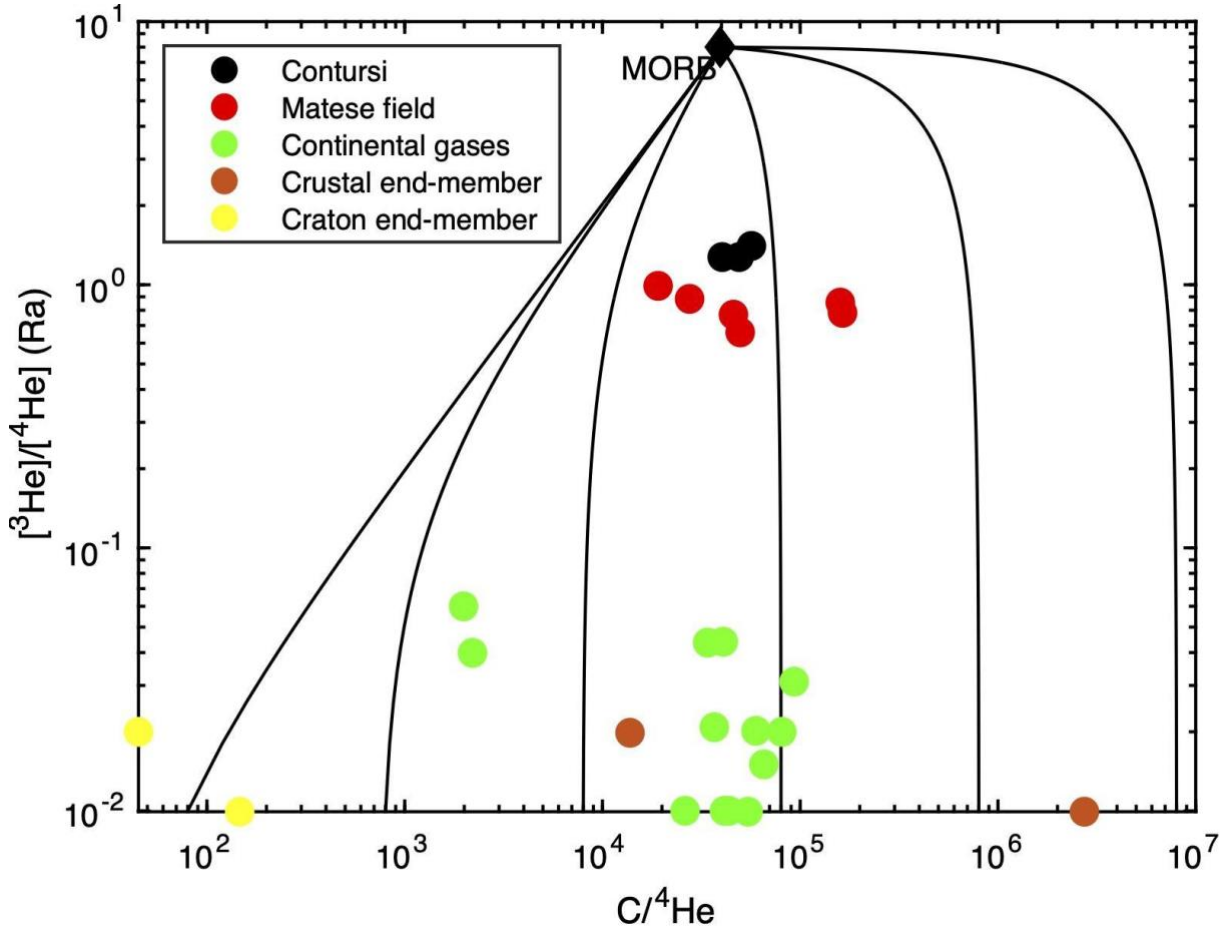

Figure III. 4: Binary mixing plot between Mantle ($^3He/^4He$= 8 RA, $CO_2/^4He$=3.94·10^4)[57] and various crustal end-members ($CO_2/^4He$=80-8·10^6). The additional data are from INGV internal database.

III. 4.2.1 Carbon mass balance of the aquifers as a simple mixing process

The classic simplified approach to determine the exogenous CO_2 who interacted and was transported by groundwater is based on a mixing process between of an arbitrary number of sources (such as dissolution of carbonate minerals, input of deeply derived CO_2, oxidation of organic material) combining the total inorganic carbon with the $\delta^{13}C_{TDIC}$.

Here, we calculated the total carbon dissolved in groundwater (C_{tot} or TDIC) concentration, saturation indices for calcite, dolomite, anhydrite, and gypsum, and partial pressure of CO_2 gas for the springs combining their chemical (pH, HCO_3, temperature), and isotopic composition. These calculations were done using the PHREEQ computer code[58] (Table III. 3).

In detail, according to Chiodini et al., (1999, 2000)[19,59], the total carbon (C_{tot}) that moved through carbonate-aquifer is due to both carbonate dissolution inside the aquifer (C_{carb}) and contributions from sources exterior to the aquifer (C_{ext}). We compute C_{ext} and $\delta^{13}C_{ext}$ for each sample using

the following carbon mass balance equations to quantify the contribution of the different carbon sources and to characterize their isotopic composition:

$$C_{tot}=C_{carb}+C_{ext} \qquad (1)$$

and

$$\delta^{13}C_{tot}\ C_{tot}=\delta^{13}C_{ext}\ C_{ext}+\delta^{13}C_{carb}\ C_{carb} \qquad (2)$$

where C_{tot} and $\delta^{13}C_{tot}$ are analytically determined (corresponding to the Total Dissolved Inorganic Carbon, TDIC, and $\delta^{13}C_{TDIC}$ respectively); C_{carb}, is calculated as the sum of [Ca]+[Mg] considering the dissolution of carbonate minerals (i.e., calcite and dolomite) and eventually of gypsum/anhydrite (from [SO_4]) if present, setting the isotopic composition of the aquifer carbon from carbonate mineral dissolution (δ^{13}Ccarb) at 2.21 ‰ ± 0.66‰ (vs. PDB) assumed in the Apennine aquifer[7]. According to the approach proposed by Chiodini et al., (2020)[17], by using the equations (1) and (2) , we computed the Cext and δ^{13}Cext for each sampled waters (Table III. 4). Because of isotopic fractionation during carbon sinks from the solution, the utilized equations underestimate Cext and enriching δ^{13}Cext, if the water is significantly changed by CO_2 degassing and/or carbonate minerals precipitation[7]. These uncertainties are assumed to be negligible in samples with TDIC<40 mmol/l, equivalent to 30 mmol/l of Cext (Chiodini et al., 2011). Below this "CO_2 degassing threshold", the system can be assumed conservative for carbon species, so the dissolved carbon and its isotopic composition can be considered the result of mixing between different carbon sources[6].

Sample ID	$SI_{Calcite}$	$SI_{Dolomite}$	SI_{Gypsum}	$SI_{CO2(g)}$	TDIC (mmol/L)
AQP	0.38	-0.20	-2.95	-2.50	4.26
PSA	0.16	-0.33	-3.19	-2.49	3.92
FIU	0.77	1.06	-3.17	-3.21	3.46
SRON	0.35	-0.10	-2.94	-2.46	4.21
SEN	0.21	-0.24	-2.69	-1.93	6.46
	0.23	-0.21	-2.69	-1.95	6.37
MAG	0.27	-1.01	-2.68	-2.14	4.85
REG	0.24	-0.18	-2.32	-1.66	8.15
	0.24	-0.19	-2.32	-1.66	8.16
ACT	0.31	-0.16	-2.03	-1.02	17.10
DC	0.03	-0.78	-2.04	-0.71	21.84
FP	0.58	-0.02	-2.17	-2.02	6.76
CAM	0.22	-0.43	-1.89	-0.70	24.10
FR	0.21	-0.41	-1.78	-0.58	28.57
CAS	0.08	-0.56	-1.57	-0.06	59.80
FOR	0.20	-0.25	-1.49	-0.26	43.05
TUF	0.32	-0.03	-0.87	-0.16	47.02
CAN	0.34	0.03	-0.94	-0.16	46.00
CAV	0.32	-0.02	-1.03	-0.17	44.68
VEN	0.60	0.78	-0.61	0.10	69.68
RSF	0.14	0.32	-1.11	-0.04	46.61
RSC	0.76	1.10	-0.87	0.03	63.23
	0.68	0.94	-0.87	0.15	71.04
GEY	0.50	1.16	-1.10	-0.14	40.84
	0.52	1.21	-1.10	-0.13	40.61
ERC	0.93	1.70	-0.80	0.01	59.29
	0.95	1.75	-0.80	0.03	59.19

Table III.3: Results of aqueous speciation calculations and dissolved carbon. Calculated saturation indices for calcite, dolomite, anhydrite and gypsum and partial pressure of CO_2 gas, given as 10^{SI} atm.

In turn, C_{ext} is given by carbon content of infiltrating waters (C_{inf}; i.e. atmospheric CO_2 plus carbon from biogenic sources active in the soils during infiltration) and the carbon content of deep sources (C_{deep})[60]:

$$C_{ext}=C_{inf}+C_{deep} \quad (3)$$

from which result the following mass balance:

$$\delta^{13}C_{ext} = \frac{\delta^{13}C_{inf}\cdot C_{inf}+\delta^{13}C_{deep}\cdot C_{deep}}{C_{ext}} \quad (4)$$

Where $\delta^{13}C_{deep} \equiv \delta^{13}C_{TDIC}$.

For the choice of deep endmember, in the classical approach, values of $\delta^{13}C_{deep}$ between -1‰, is representative of a typical mantle source in Appenine, and +1‰ (or more positive values, up to 4), typical of carbonates in Appenine, are usually used. However, this approach considers the CO_2 signature unaffected by the gas-rock-water interaction outcome. In the following sections,

we will consider the reworking undergone by mantle CO_2 in the deep reservoir due to the interaction with dolomite and the subsequent water-rock interaction of the shallow reservoir.

III. 4.2.2 Deep CO_2-rocks interactions

However, the conventional mixing model that we examined in the prior session assumes that the outcome of the gas-rock-water interaction has no impact on the CO_2 signature. Now, we will consider the reworking undergone by deep CO_2 in the deep reservoir due to the interaction with dolomite and the subsequent water-rock interaction of the shallow reservoir.

Previous geophysical investigations[39] combined with the knowledge of the deep geology recognized the occurring of deep gaseous reservoirs that store deep-sourced fluids, such as CO_2 and He[26,31–33]. Improta et al., (2014)[39] indicated that volumes of pressurized rock are located between 8-12 km under the Apula Platform and are located within layers of Triassic dolostones and anhydrites. Considering the ratio of the mass of dolomite to the mass of gaseous CO_2 were ($m_{dolomite} \gg mCO_{2(gas)}$) with porosity between 0.1-0.01% and due to the high-density difference between calcite/dolomite and CO_2 (two orders of magnitude for a CO_2 at T> 100°C and P>3 atm) and considering the equations in Rozanski et al., (2001)[61] for mixing of reservoirs of different compounds, even in the presence of low residence times (i.e., short gas-rock interaction times) we can consider the result of the $\delta^{13}Cco_{2(g)}$ fractionation of CO_2 in equilibrium with dolomite in such a way as to fit the equation:

$$\varepsilon_{CO_2-dolomite} = \delta^{13}CCO_{2\,(gas)} - \delta^{13}C_{dolomite} \qquad (5)$$

In the range of depth of 7-13 km, approximatively the deep dry reservoir reported in Improta et al., (2014)[39] the crustal temperatures ranged between 190°C and 340°C[36]. Under these conditions, the value of $\varepsilon_{CO_2-dolomite}$ varies between -0.26 to +1.19 ‰, -1.33 to +4.13‰ and +2.39 to +4.27‰ according to Horita et al,. (2001)[62], Schauble et al., (2006)[63] and Deines et al., (2004)[64] respectively.

Considering the signature of Triassic dolomite $\delta^{13}C_{dolomite}$=3.45‰ (mean value, De Paola et al., 2011[65]), and solving for $\delta^{13}CCO_{2\,(gas)}$ in equation (5) we estimate that the gaseous CO_2 in the deep reservoir in equilibrium with host rocks, no matter what its nature is, due to decarbonation or magma/mantle degassing, is characterised by having $\delta\ ^{13}CCO_{2(deep)}$=+2.12 to +7.72 ‰ for a dolomite range that partially overlaps the marine carbonate signature rang (from -12‰ up to +10‰, Planavsky et al., 2014).

III. 4.2.3 CO_2-Water/Brine interactions

After interaction with dolomite within natural reservoirs in the Apulian Platform, the deep CO_2 migrates upward through an intricate pattern of active faults until reaching the shallow water-saturated fluid reservoirs in the carbonate lithology.

More in detail, the shallower CO_2 gas cap at about 1-3 km is characterized by the presence of brines[39]. In order to model the CO_2-water phase interaction, we have considered separately a low salinity water-saturated aquifer and a brine rich reservoir.

A carbonate-water system (an aquifer in carbonate rocks) exposed to an input of CO_2 is well described by following equation[61]:

$$\left(\frac{K_0K_1}{[H^+]} + 2\frac{K_0K_1K_2}{[H^+]^2}\right)P_{CO_2}^2\left(\frac{K_w}{[H^+]} - [H^+]\right)P_{CO_2} + 2\frac{K_{cal}[H^+]^2}{K_0K_1K_2} = 0 \qquad (6)$$

where the carbonate-water equilibrium constants are dependent on temperature, pH and P_{CO2}. The combination of these parameters establishes the abundance of each carbon specie and can be given in terms of H_2CO_3, according to the following equations[61]:

$$[H_2CO_3] = K_0P_{CO2} \quad (7)$$

$$[H_2CO_3^-] = \frac{K_1}{[H^+]}[H_2CO_3] \quad (8)$$

$$[CO_3^{2-}] = \frac{K_1K_2}{[H^+]^2}[H_2CO_3] \quad (9)$$

Where, the ionic product of water (K_w) comes from the equation by Dickson and Riley (1979)[66], the molar solubility K_0 (moi l^{-1} atm^{-1}) obtained by Dickoson et al., (2007)[67], the dissociation constant of the first and second dissociation of carbonic acid (K_1 and K_2, respectively) obtained by Dickson and Millero (1987)[68] and the stechiometric solubility constant of calcite obtained by Mucci (1983)[69].

Assuming (i) TDIC and HCO_3 to be entirely derived from CO_2 (gas) dissolution and CO_2(aq) conversion, respectively, and (ii) the attainment of isotopic equilibrium between gaseous and dissolved carbon species, the isotope mass balance can be used to define the $\delta^{13}C$ values of TDIC and CO_2(aq) resulting from CO_2(gas) dissolution, as follows:

$$\delta^{13}C_{TDIC} = \delta^{13}C_{CO2} + \varepsilon_{TDIC-CO2(g)} \qquad (10)$$

Were $\varepsilon_{TDIC-CO2(g)}$ was obtained by summing up the fractionation factors between each dissolved carbon species, dissolved carbon dioxide (CO_{2aq}), bicarbonate (HCO_3^-) and carbonate ions (CO_3^{2-}) and CO_2, weighted for their abundance with respect to total dissolved carbon, as follows[70,71]:

$$\varepsilon_{TDIC-CO2(g)} = \varepsilon_{HCO3-CO2(g)} \cdot X_{HCO3} + \varepsilon_{CO2(aq)-CO2(g)} \cdot X_{H2CO3} + \varepsilon_{CO_3^{2-}-CO2(g)} \cdot X_{CO3(2-)} \quad (11)$$

Where X represents the mole fraction. The enrichment factors between CO_2(gas) and HCO_3^- ($\varepsilon_{HCO_3^- - CO2(g)}$) and CO_2 gas and CO_2 dissolved ($\varepsilon_{CO2(d)-CO2(g)}$), are defined by Mook et al., (1974)[72], in the case of fresh water and, considering the interaction of deep gases with a non-ideal solution such as a brine, we followed Myrttinen et al. (2015)[73].

We apply this iteration of the water-rock-gas model to determine the best value of $\delta^{13}C_{TDIC}$ that can represent the deep source signature in the study area. Considering waters with a pH lower than 6 and temperatures close to those of the thermal waters in the area (48-50°C), we determined that the $\delta^{13}C_{TDIC}$ corresponding to the first interaction in shallow-water carbonate reservoir with deep CO_2, that has previously interacted with dolomite in the deep reservoir, varies between 2.21‰ and 7.81‰ in the case of low salinity waters (S=0‰) and between 3.62‰ and 9.23‰ in the case of brine (S=35‰). These values are markedly different from those negative value measured in the cool water and in the range as thermal and ipothermal.

III. 4.3 Secondary processes controlling the chemical and isotopic compositions of thermal springs and gas emissions

In the reconstruction of gas-rock-water interaction processes, we have taken into account a process which involves different matrices (gas, rocks, water or brine) at different conditions of depths (pressure) and temperatures.

III. 4.3.1 Aquifer CO_2-degassing

In order to evaluate if degassing of CO_2 from water could be a process that control the decrease of TDIC and the relative variability of the $\delta^{13}C_{TDIC}$ in the studied water when Cext>30 mmol/l, we modelled the effects of degassing on the isotopic signatures of $\delta^{13}C$ of TDIC ($\delta^{13}C_{TDIC}$) and extracted CO_2 ($\delta^{13}C_{CO2(g)}$) can be by a Rayleigh distillation equation using a Hoefs (2009)[74] modified equation:

$$\delta^{13}C_{TDIC} = (\delta^{13}C_{TDIC} + 10^3) \cdot F^{1/\alpha_{TDIC-CO2(g)}-1} - 10^3 \quad (12)$$

Where $\delta^{13}C_{TDIC}$ denotes the initial value of the isotopic composition of the TDIC, F the fraction of CO_2 remaining after degassing and $\alpha_{TDIC-CO2(g)}$ is derived from $\varepsilon_{TDIC-CO2(g)}$ reported in equation (9) as follows:

$$\alpha_{TDIC-CO2(g)} = \frac{\varepsilon_{TDIC-CO2(g)}}{10^3} + 1 \qquad (13)$$

As a consequence of equations (9) and (13), the fractionation factor $\alpha_{TDC-CO2(g)}$ is larger for higher pH values, due to the different fractionation factors between dissolved carbon species and CO_2.

We chose initial model values for CO_2 dissolution and subsequent outgassing so that the parameters would minimise the coefficient of determination (R^2) between model and measured values for thermal sites. So, in the case of salinity S=0‰ we found that the initial conditions, fit the value measured in our thermal site with an R^2=0.94, calculate using distance2curve[75] and rsquare MATLAB functions. In this case, the $\delta^{13}C_{TDIC}$=3.29‰, corresponding at $\delta^{13}C_{CO2(deep)}$=3.2‰, with a $\varepsilon_{TDIC-CO2(g)}$=0.09‰ calculated by eq. (9) (Fig. III. 5a)

In the case of salinity S=35‰, the theoretical curve does not directly fit the points, but the best result (R^2=0.3) is obtained with $\delta^{13}C_{CO2(deep)}$=2.12 and the $\delta^{13}C_{TDIC}$=3.62‰ ($\varepsilon_{TDIC-CO2(g)}$=1.5‰), see Fig. III. 5b.

The values $\delta^{13}C_{CO2(deep)}$ can obtained from gas-dolomite interaction a temperature between 224-184 °C (8.30-7.10 km depth) to which corresponding values of $\varepsilon_{CO_2-dolomite} = -0.25$‰ and -1.33‰, for S=0‰ and S=35‰ respectively, compatible with the top of deeper reservoir.

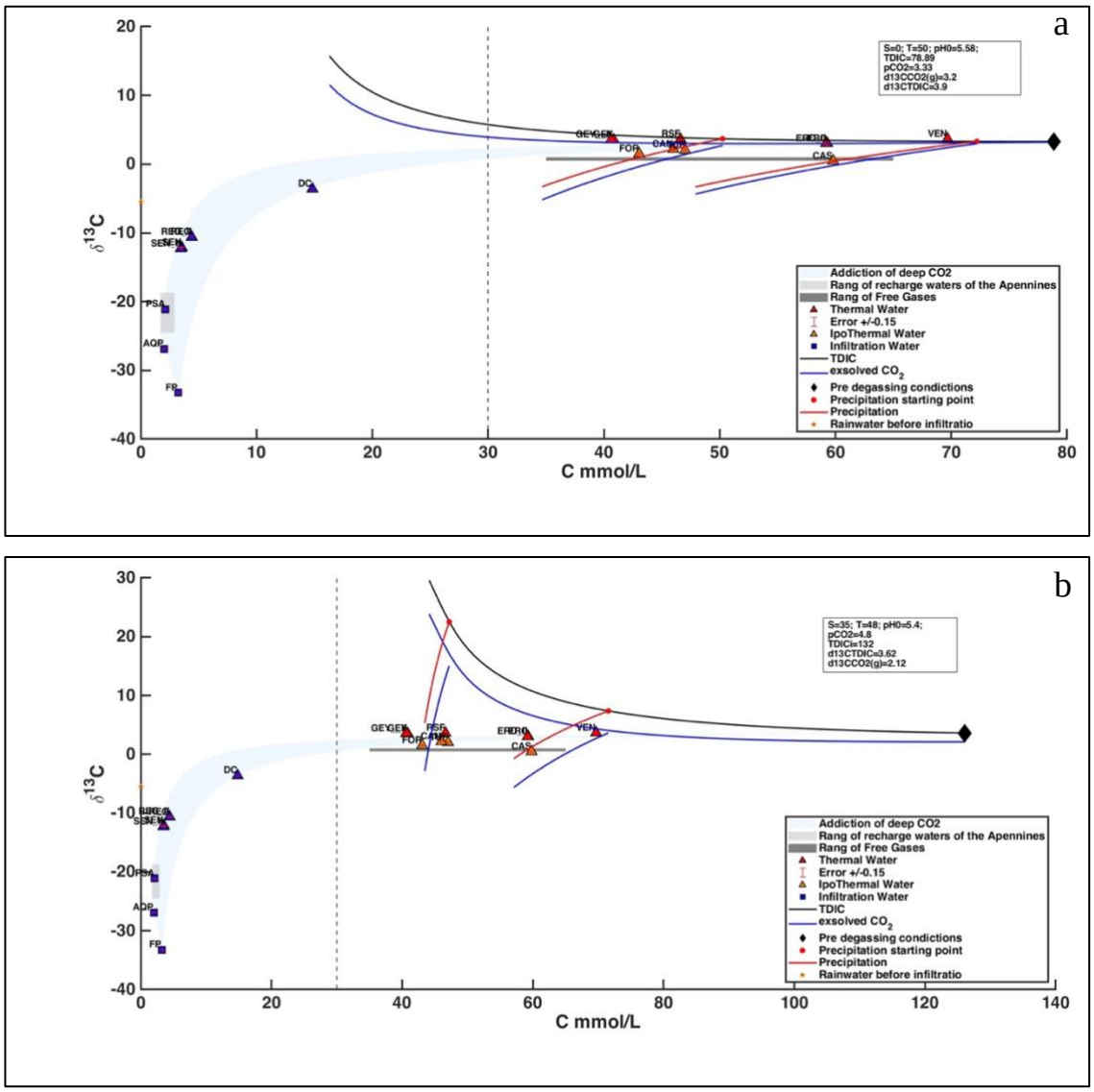

Figure III.5: C v. $\delta^{13}C$ diagram in brine-gas-rocks interaction. C v. $\delta^{13}C$ diagram in water-gas-rocks interaction. The theoretical field resulting from the addition of Cdeep with $\delta^{13}C_{TDIC}$=+3.29‰ for low salinity water (a) and 3.62‰ for brine (b), to infiltrating water is indicated in light blue. The dashed vertical line represents the Cext upper limit for the applicability of the no-sink assumption.

III. 4.3.2 Calcite precipitation effect

The isotopic fractionation caused by calcite precipitation occurring during water circulation under open-system conditions can be described as a Rayleigh-type fractionation process, as follows:

$$\delta^{13}C_{TDIC(res)} = \left(\delta^{13}C_{TDIC(init)} + 10^3\right) \cdot F'^{\alpha_{calcite-TDIC}-1} - 10^3 \quad (14)$$

Where $\delta^{13}C_{TDIC(init)}$ is the initial isotopic composition of TDIC in the hydrothermal fluid, $\delta^{13}C_{TDIC(res)}$ is the isotopic composition of the residual TDIC after calcite precipitation, F' is the fraction of residual TDIC and $\alpha_{calcite-TDIC}$ is the isotopic fractionation factor between calcite and TDIC computed, as follows[76] (Venturi et al., 2017):

$$\alpha_{calcite-TDIC} = [\varepsilon_{calcite-CO2(g)} - (X_{H2CO3} \cdot \varepsilon_{CO2(aq)-CO2(g)}) + (X_{HCO3} \cdot \varepsilon_{HCO3-CO2(g)})] \cdot 10^{-3} + 1 \quad (15)$$

The $\varepsilon_{CO2(aq)-CO2(g)}$ value was calculated as in Eq. (2), whereas $\varepsilon_{calcite-CO2(g)}$ were calculated using the equations proposed by Deines et al. (1974)[77], as follows:

$$\varepsilon_{calcite-CO2(g)} = \frac{1194000}{T^2} - 3.63 \quad (16)$$

By this process, it is possible to explain the $\delta^{13}C_{TDIC}$ values for the hypothermal sites, which show a trend that is consistent with the calcite precipitation curves starting at appropriate positions along the outgassing trend in the case of low salinity water (Fig. III. 5a). While, in the case of brine, all the hot water are the result of precipitation (Fig. III. 5a).

III. 4.3.3 Free gases interpretation

In order to reconstruct the behaviour of the dissolved carbon and its relationship with the degassing of CO_2 in the Contursi area, we looked at the interaction between deep-CO_2 and the local infiltration water according to a Rayleigh process in which the fraction of CO_2 exsolved from aquifer can be modelled using the following equation[74]:

$$\delta^{13}C_{CO2(res)} = \alpha_{TDIC-CO2(g)} \cdot (\delta^{13}C_{TDIC(init)} + 10^3) \cdot F'^{\alpha_{TDIC-CO2(g)}-1} - 10^3 \quad (17)$$

Where the $\alpha_{TDIC-CO2(g)}$is calculated following the equation (13) at T=50°C for S=0‰ and for S=35‰.

To examine the possibility that the $\delta^{13}C_{CO2(g)}$ values for free gas occurrences in the area are due to CO_2 degassing and contemporary calcite precipitation in the aquifer we have computed the values of $\delta^{13}C_{CO2}$ of residual $CO_{2(g)}$ ($\delta^{13}C_{CO2(res)}$) as a function of residual fraction F' using equation (17) and we find that values of $\delta^{13}C_{CO2(res)}$ in the range of CAS site are compatible with those found on the surface ($\delta^{13}C_{CO2}$=0.7‰ for SST and $\delta^{13}C_{CO2} = 0.86$‰ for OV1) this site is however far (about 4 km) from free gas sites. Alternatively, we can imagine that the latter derive from water similar to that of the FOR, CAN and TUF sites (about 2 km away) which have continued the degassing-precipitation process.

III. 4.3.4 Output of deeply derived CO_2

Table III. 4 are show the values of Ccarb and Cext calculated by equations (1) and Ceep, calculated following equation (3) assuming Cinf=3.23 mmol/l (i.e., the Cext value of FP site). In sites where the value of Cext is below the assumed Cinf value, we assume that the Cdeep is absent (or negligible) and Cext practically coincides with Cinf. Once all the terms of the carbon budget are determined, the total output of deep-CO_2 (QCO_2-deep) can be computed for any

carbon source for which the flow-rate is known. As a result, the total rate of deep-CO_2 in cold water is $Q_{CO2\text{-}deep,cold}$=4.8 10^8 mol/y; in ipothermal water $Q_{CO2\text{-}deep,ipo}$=8.91 10^8 mol/y and in thermal water $Q_{CO2\text{-}deep,ipo}$=1.86 10^8 mol/y. In total, for the dissolved sources the $Q_{CO2\text{-}deep,dis}$=1.56·10^9 mol/y. If we also take into account free sources such as San Sisto, $Q_{CO2\text{-}deep,free}$=4.82·10^8 mol/y (Italiano et al., 2000) the total output in the area becomes $Q_{CO2\text{-}tot}$ =2.04·10^9 mol/y. This value, even if underestimated due to the partial knowledge of data on flow rates and the influence of secondary processes, is comparable with total budget of mantle-derived CO_2 in active and quiescent volcanic systems in Italy and elsewhere (see Fig. III. 6).

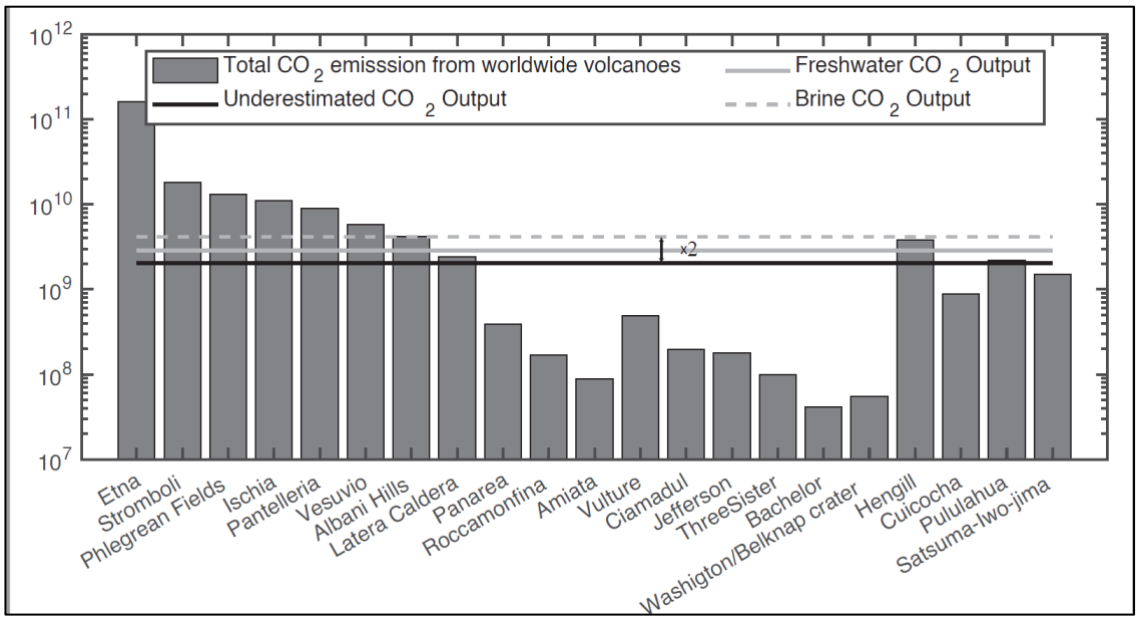

Figure III. 6: CO_2 Output. Assumptions that exclude secondary processes (black full line) can underestimate CO_2 outputs by up to twice as much. The total budget of mantle-derived CO_2 from worldwide volcanoes are reported reported for a comparison.

If we take secondary processes into the consideration, and assume a pre-degassing TDIC value of 78.89 mmol/l in case of freshwater (132 mmol/l in case of brine with S=35‰), the Q for hypothermals and thermals becomes 1.62 10^9 (2.71 10^9) mol/y and 2.81 10^8 (4.71 10^9) mol/y respectively, then $Q_{CO2\text{-}tot}$ became 2.86 10^9 (4.14 10^9) mol/y i.e. 40% (twice) more than the approximate value.

Therefore, the adoption of a more realistic geochemical model highlights how output can be much more intense than those estimated using simplified models, depending on how much weight the secondary processes that the fluids undergo on their way to the surface have.

	Sample Name	Sample ID	Q (L/s)	TDIC (mmol/L)	Ccarb (mmol/L)	Cext (mmol/L)	Cdeep (mmol/L)	QCDeep (mol/y)	QCDeep-Pre Degassing (mol/y)
Cold Waters	Acquara ponticchio	AQP	100	4.26	2.26	2.00			
	Piceglia Alta	PSA		3.92	1.80	2.12			
	fiumicello	FIU	40	3.46	1.70	1.76			
	S Oronzo	SRON	20	4.21	2.20	2.01			
	Senerchiella	SEN	2000	6.46	2.92	3.54	1.23	7.77E+07	
				6.37	2.92	3.46	1.15	7.25E+07	
	Magliana	MAG	10	4.85	2.50	2.35			
	Sorgente la regina (basso tanagro)	REG	5590	8.15	3.75	4.40	2.09	3.69E+08	
				8.16	3.75	4.41	2.10	3.71E+08	
	Acetosella	ACT	5	17.10	7.02	10.08	7.77	1.23E+06	
	DonCarlo	DC	50	21.84	7.01	14.83	12.52	1.98E+07	
	Fontana Prete	FP	0.1	6.76	3.53	3.23			
	CantaniMix	CAM	70	24.10	8.43	15.67	13.36	2.95E+07	
	Ferrata	FR	0.7	28.57	9.50	19.06	16.75	3.70E+05	
Ipothermal waters	Cantani solfurea	CAS	100	59.80		59.80	57.49	1.81E+08	2.80E+08
	Forlenza	FOR	500	43.05		43.05	40.74	6.43E+08	1.40E+09
	Tufaro	TUF		47.02		47.02	44.71		
	Cappetta Nuova	CAN		46.00		46.00	43.69		
	Cappetta Vecchia	CAV	50	44.68		44.68	42.37	6.69E+07	1.40E+08
Thermal waters	CapassoVenere	VEN		69.68		69.68	67.37		
	RosaPepe Fredda	RSF	60	46.61		46.61	44.30	8.39E+07	1.68E+08
	RosaPepe Calda	RSC	40	63.23		63.23	60.92	7.69E+07	1.12E+08
				71.04		71.04	68.73	8.68E+07	1.12E+08
	CapassoGeyser	GEY	13	40.84		40.84	38.53	1.58E+07	3.64E+07
				40.61		40.61	38.30	1.57E+07	3.64E+07
	CapassoErcole	ERC		59.29		59.29	56.98		
				59.19		59.19	56.88		

Table III.4: Output of Deep CO_2 in predeceasing and post degassing condition.

III. 5 REFERENCES

1. Italiano, F., Martinelli, G., Bonfanti, P. & Caracausi, A. Long-term (1997-2007) geochemical monitoring of gases from the Umbria-Marche region. *Tectonophysics* **476**, 282–296 (2009).
2. Italiano, F., Caracausi, A., Favara, R., Innocenzi, P. & Martinelli, G. Geochemical monitoring of cold waters during seismicity: Implications for earthquake-induced modification in shallow aquifers. *TAO* **16**, 709–729 (2005).
3. Caracausi, A. *et al.* Active geodynamics of the central Mediterranean Sea: Tensional tectonic evidences in western Sicily from mantle-derived helium. *Geophys. Res. Lett.* **32**, 1–5 (2005).
4. Caracausi, A. & Sulli, A. Outgassing of Mantle Volatiles in Compressional Tectonic Regime Away From Volcanism: The Role of Continental Delamination. *Geochem. Geophys. Geosyst.* **20**, 2007–2020 (2019).
5. Tamburello, G., Pondrelli, S., Chiodini, G. & Rouwet, D. Global-scale control of extensional tectonics on CO 2 earth degassing. *Nat. Commun.* **9**, 4608 (2018).
6. Chiodini, G. *et al.* Geochemical evidence for and characterization of CO2 rich gas sources in the epicentral area of the Abruzzo 2009 earthquakes. *Earth Planet. Sci. Lett.* **304**, 389–398 (2011).
7. Chiodini, G. *et al.* Carbon dioxide Earth degassing and seismogenesis in central and southern Italy. *Geophys. Res. Lett.* **31**, (2004).
8. Randazzo, P. *et al.* Active degassing of deeply sourced fluids in central Europe: New evidences from a geochemical study in Serbia. *Geochem. Geophys. Geosyst.* **22**, (2021).
9. Caracausi, A., Buttitta, D., Picozzi, M., Paternoster, M. & Stabile, T. A. Earthquakes control the impulsive nature of crustal helium degassing to the atmosphere. *Communications Earth & Environment* **3**, 1–8 (2022).
10. Curzi, M. *et al.* U-Pb age of the 2016 Amatrice earthquake causative fault (Mt. Gorzano, Italy) and paleo-fluid circulation during seismic cycles inferred from inter- and co-seismic calcite. *Tectonophysics* **819**, 229076 (2021).

11. Miller, S. a. *et al.* Aftershocks driven by a high-pressure CO2 source at depth. *Nature* **427**, 724–727 (2004).
12. Coppola, M. *et al.* Meso- to nano-scale evidence of fluid-assisted co-seismic slip along the normal Mt. Morrone Fault, Italy: Implications for earthquake hydrogeochemical precursors. *Earth Planet. Sci. Lett.* **568**, 117010 (2021).
13. Marchesini, B. *et al.* Chemical interaction driven by deep fluids in the damage zone of a seismogenic carbonate fault. *J. Struct. Geol.* **161**, 104668 (2022).
14. Krishnamurthy, P. G., DiCarlo, D. & Meckel, T. Geologic heterogeneity controls on trapping and migration of CO 2. *Geophys. Res. Lett.* **49**, (2022).
15. Nicoli, G., Borghini, A. & Ferrero, S. The carbon budget of crustal reworking during continental collision: Clues from nanorocks and fluid inclusions. *Chem. Geol.* **608**, 121025 (2022).
16. Groppo, C., Rolfo, F. & Frezzotti, M. L. CO2 outgassing during collisional orogeny is facilitated by the generation of immiscible fluids. *Communications Earth & Environment* **3**, 1–11 (2022).
17. Chiodini, G. *et al.* Correlation between tectonic CO_2 Earth degassing and seismicity is revealed by a 10-year record in the Apennines, Italy. *Science Advances* **6**, eabc2938 (2020).
18. Randazzo, P. *et al.* Active degassing of crustal CO2 in areas of tectonic collision: A case study from the Pollino and Calabria sectors (Southern Italy). *Front Earth Sci. Chin.* **10**, (2022).
19. Chiodini, G., Frondini, F., Cardellini, C., Parello, F. & Peruzzi, L. Rate of diffuse carbon dioxide Earth degassing estimated from carbon balance of regional aquifers: The case of central Apennine, Italy. *J. Geophys. Res.* **105**, 8423–8434 (2000).
20. Kipfer, R., Aeschbach-Hertig, W., Peeters, F. & Stute, M. Noble Gases in Lakes and Ground Waters. *Rev. Mineral. Geochem.* **47**, 615–700 (2002).
21. Aggarwal, P. K. *et al.* Continental degassing of 4He by surficial discharge of deep groundwater. *Nat. Geosci.* **8**, 35–39 (2015).
22. Karolyte, R. *et al.* Tracing the migration of mantle CO2 in gas fields and mineral water springs in south-east Australia using noble gas and stable isotopes. *Geochim. Cosmochim. Acta* **159**, 109–128 (2019).
23. Gilfillan, S. M. V. *et al.* Solubility trapping in formation water as dominant CO(2) sink in natural gas fields. *Nature* **458**, 614–618 (2009).

24. Barberio, M. D., Barbieri, M., Billi, A., Doglioni, C. & Petitta, M. Hydrogeochemical changes before and during the 2016 Amatrice-Norcia seismic sequence (central Italy). *Sci. Rep.* **7**, 11735 (2017).
25. Buttitta, D. *et al.* Continental degassing of helium in an active tectonic setting (northern Italy): the role of seismicity. *Sci. Rep.* **10**, 162 (2020).
26. Caracausi, A. & Paternoster, M. Radiogenic helium degassing and rock fracturing: A case study of the southern Apennines active tectonic region. *J. Geophys. Res. [Solid Earth]* **120**, 2200–2211 (2015).
27. Italiano, F., Martinelli, G. & Nuccio, P. M. Anomalies of mantle-derived helium during the 1997-1998 seismic swarm of Umbria-Marche, Italy. *Geophys. Res. Lett.* **28**, 839–842 (2001).
28. Piana Agostinetti, N., Giacomuzzi, G. & Chiarabba, C. Seismic swarms and diffuse fracturing within Triassic evaporites fed by deep degassing along the low-angle Alto Tiberina normal fault (central Apennines, Italy). *J. Geophys. Res. [Solid Earth]* **122**, 308–331 (2017).
29. D'Agostino, N. *et al.* Crustal deformation and seismicity modulated by groundwater recharge of Karst aquifers. *Geophys. Res. Lett.* **45**, 12,253-12,262 (2018).
30. Smeraglia, L. *et al.* Crustal-scale fluid circulation and co-seismic shallow comb-veining along the longest normal fault of the central Apennines, Italy. *Earth Planet. Sci. Lett.* **498**, 152–168 (2018).
31. Italiano, F., Martelli, M., Martinelli, G. & Nuccio, P. M. Geochemical evidence of melt intrusions along lithospheric faults of the Southern Apennines, Italy: Geodynamic and seismogenic implications. *J. Geophys. Res. [Solid Earth]* **105**, 13569–13578 (2000).
32. Caracausi, A., Martelli, M., Nuccio, P. M., Paternoster, M. & Stuart, F. M. Active degassing of mantle-derived fluid: A geochemical study along the Vulture line, southern Apennines (Italy). *J. Volcanol. Geotherm. Res.* **253**, 65–74 (2013).
33. Chiodini, G. *et al.* Non-volcanic CO2Earth degassing: Case of Mefite d'Ansanto (southern Apennines), Italy. *Geophys. Res. Lett.* **37**, (2010).
34. William Cavazza, François Roure, Wim Spakman, Gerard M. Stampfli, Peter A. Ziegler. *The TRANSMED Atlas. The Mediterranean Region from Crust to Mantle*. (Springer Berlin Heidelberg).
35. Patacca, E., Scandone, P. & Mazzotti, A. Constraints on the interpretation of the CROP-04 seismic line derived from Plio-Pleistocene foredeep and thrust-sheet-top

deposits (Southern Apennines, Italy). *Bollettino della Società Geologica Italiana), Special Issue* **7**, 241–256 (2007).

36. Boncio, P., Mancini, T., Lavecchia, G. & Selvaggi, G. Seismotectonics of strike–slip earthquakes within the deep crust of southern Italy: Geometry, kinematics, stress field and crustal rheology of the Potenza 1990 …. *Tectonophysics* (2007).
37. Ascione, A., Mazzoli, S., Petrosino, P. & Valente, E. A decoupled kinematic model for active normal faults: Insights from the 1980, MS = 6.9 Irpinia earthquake, southern Italy. *GSA Bulletin* **125**, 1239–1259 (2013).
38. Ghisetti, F. & Vezzani, L. Normal faulting, transcrustal permeability and seismogenesis in the Apennines (Italy). *Tectonophysics* **348**, 155–168 (2002).
39. Improta, L., De Gori, P. & Chiarabba, C. New insights into crustal structure, Cenozoic magmatism, CO2degassing, and seismogenesis in the southern Apennines and Irpinia region from local earthquake tomography: seismic tomography of Apennines. *J. Geophys. Res. [Solid Earth]* **119**, 8283–8311 (2014).
40. Pantosti, D. & Valensise, G. Source geometry and long term behavior of the 1980, Irpinia earthquake fault based on field geologic observations. *Ann. Geophys.* **36**, (1993).
41. Picozzi, M. *et al.* Spatiotemporal Evolution of Microseismicity Seismic Source Properties at the Irpinia Near-Fault Observatory, Southern Italy. *Bull. Seismol. Soc. Am.* **112**, 226–242 (2022).
42. De Landro, G. *et al.* Author Correction: Decade-long monitoring of seismic velocity changes at the Irpinia fault system (southern Italy) reveals pore pressure pulsations. *Sci. Rep.* **12**, 16039 (2022).
43. Amoroso, O., Ascione, A., Mazzoli, S., Virieux, J. & Zollo, A. Seismic imaging of a fluid storage in the actively extending Apennine mountain belt, southern Italy. *Geophys. Res. Lett.* **41**, 3802–3809 (2014).
44. Amoroso, O. *et al.* From velocity and attenuation tomography to rock physical modeling: Inferences on fluid-driven earthquake processes at the Irpinia fault system in southern Italy. *Geophys. Res. Lett.* **44**, 6752–6760 (2017).
45. Cocco, M. & Pacor, F. The rupture process of the 1980 Irpinia, Italy, earthquake from the inversion of strong motion waveforms. *Tectonophysics* **218**, 157–177 (1993).

46. Capasso, G. & Inguaggiato, S. A simple method for the determination of dissolved gases in natural waters. An application to thermal waters from Vulcano Island. *Appl. Geochem.* **13**, 631–642 (1998).
47. Sano, Y., Takahata, N. & Seno, T. Geographical Distribution of 3He/4He Ratios in the Chugoku District, Southwestern Japan. *Pure Appl. Geophys.* **163**, 745–757 (2006).
48. Darrah, T. H. *et al.* The evolution of Devonian hydrocarbon gases in shallow aquifers of the northern Appalachian Basin: Insights from integrating noble gas and hydrocarbon geochemistry. *Geochim. Cosmochim. Acta* **170**, 321–355 (2015).
49. Ballentine, C. J. & Sherwood Lollar, B. Regional groundwater focusing of nitrogen and noble gases into the Hugoton-Panhandle giant gas field, USA. *Geochim. Cosmochim. Acta* **66**, 2483–2497 (2002).
50. Sano, Y. & Wakita, H. Geographical distribution of 3He/4He ratios in Japan: Implications for arc tectonics and incipient magmatism. *J. Geophys. Res. [Solid Earth]* **90**, 8729–8741 (1985).
51. Darrah, T. H. *et al.* Gas chemistry of the Dallol region of the Danakil Depression in the Afar region of the northern-most East African Rift. *Chem. Geol.* **339**, 16–29 (2013).
52. Ozima, M. & Podosek, F. A. *Noble Gas Geochemistry*. (Cambridge University Press, 2002).
53. Mabry, J., Lan, T., Burnard, P. & Bernard, M. High-precision helium isotope measurements in air. *J. Anal. At. Spectrom.* **28**, 1903–1910 (2013).
54. Gautheron, C., Moreira, M. & Allègre, C. He, Ne and Ar composition of the European lithospheric mantle. *Chem. Geol.* **217**, 97–112 (2005).
55. Morrison, P. & Pine, J. Radiogenic origin of the helium isotopes in rock. *Ann. N. Y. Acad. Sci.* **62**, 71–92 (1955).
56. Halford, D. T. *et al.* High helium reservoirs in the four corners area of the Colorado Plateau, USA. *Chem. Geol.* 120790 (2022).
57. Marty, B. *et al.* An evaluation of the C/N ratio of the mantle from natural CO2-rich gas analysis: Geochemical and cosmochemical implications. *Earth Planet. Sci. Lett.* **551**, 116574 (2020).
58. Parkhurst, D. L., Thorstenson, D. C. & Plummer, N. *PHREEQE : a computer program for geochemical calculations*. http://pubs.er.usgs.gov/publication/wri8096 (1980) doi:10.3133/wri8096.

59. Chiodini, G. *et al.* Quantification of deep CO2 fluxes from Central Italy. Examples of carbon balance for regional aquifers and of soil diffuse degassing. *Chem. Geol.* **159**, 205–222 (1999).
60. Frondini, F. *et al.* Measuring and interpreting CO2 fluxes at regional scale: the case of the Apennines, Italy. *J. Geol. Soc. London* **176**, 408–416 (2019).
61. Rozanski, K., Froehlich, K. & Mook, W. G. *Environmental isotopes in the hydrological cycle: Principles and applications*. vol. I (Unesco, 2001).
62. Chacko, T., Cole, D. R. & Horita, J. Equilibrium oxygen, hydrogen and carbon isotope fractionation factors applicable to geologic systems. https://www.researchgate.net/publication/332250633 (2001) doi:10.2138/gsrmg.43.1.1.
63. Schauble, E. A., Ghosh, P. & Eiler, J. M. Preferential formation of 13C–18O bonds in carbonate minerals, estimated using first-principles lattice dynamics. *Geochim. Cosmochim. Acta* **70**, 2510–2529 (2006).
64. Deines, P. Carbon isotope effects in carbonate systems. *Geochim. Cosmochim. Acta* **68**, 2659–2679 (2004).
65. De Paola, N. *et al.* Fault lubrication and earthquake propagation in thermally unstable rocks. *Geology* **39**, 35–38 (2011).
66. Dickson, A. G. & Riley, J. P. The estimation of acid dissociation constants in seawater media from potentionmetric titrations with strong base. I. The ionic product of water — Kw. *Mar. Chem.* **7**, 89–99 (1979).
67. Dickson, A. G., Sabine, C. L. & Christian, J. R. *Guide to best practices for ocean CO2 measurements*. (North Pacific Marine Science Organization, 2007).
68. Dickson, A. G. & Millero, F. J. A comparison of the equilibrium constants for the dissociation of carbonic acid in seawater media. *Deep Sea Res. A* **34**, 1733–1743 (1987).
69. Mucci, A. The solubility of calcite and aragonite in seawater at various salinities, temperatures, and one atmosphere total pressure. *Am. J. Sci.* **283**, 780–799 (1983).
70. Capasso, G., Carapezza, M. L., Federico, C., Inguaggiato, S. & Rizzo, A. Geochemical monitoring of the 2002–2003 eruption at Stromboli volcano (Italy): precursory changes in the carbon and helium isotopic composition of fumarole gases and thermal waters. *Bull. Volcanol.* **68**, 118–134 (2005).

71. Grassa, F., Capasso, G., Favara, R. & Inguaggiato, S. Chemical and Isotopic Composition of Waters and Dissolved Gases in Some Thermal Springs of Sicily and Adjacent Volcanic Islands, Italy. *Pure Appl. Geophys.* **163**, 781–807 (2006).
72. Mook, W. G., Bommerson, J. C. & Staverman, W. H. Carbon isotope fractionation between dissolved bicarbonate and gaseous carbon dioxide. *Earth Planet. Sci. Lett.* **22**, 169–176 (1974).
73. Myrttinen, A., Becker, V., Mayer, B., van Geldern, R. & Barth, J. A. C. Determining in situ pH values of pressurised fluids using stable carbon isotope techniques. *Chem. Geol.* **391**, 1–6 (2015).
74. Hoefs, J. *Stable Isotope Geochemistry*. (Springer Science & Business Media, 2009).
75. D'Errico, J. distance2curve. *MATLAB Central File Exchange* (2022).
76. Venturi, S. *et al.* Fractionation processes affecting the stable carbon isotope signature of thermal waters from hydrothermal/volcanic systems: The examples of Campi Flegrei and Vulcano Island (southern Italy). *J. Volcanol. Geotherm. Res.* **345**, 46–57 (2017).
77. Deines, P., Langmuir, D. & Harmon, R. S. Stable carbon isotope ratios and the existence of a gas phase in the evolution of carbonate ground waters. *Geochim. Cosmochim. Acta* **38**, 1147–1164 (1974).

GENERAL CONCLUSION

We are learning new things about the interaction between tectonics, seismicity, and fluid flow through the crust thanks to the ability of modern geoscience to combine geological, geochemical, and geophysical studies in seismic zones. This multidisciplinary approach, has become essential when studying crustal fluids. These in fact, when are stored and transported through the crust, they mix and interact with gas, water, and rocks, changing their original chemical composition.

As shown in chapter I, the field of stress associated to the seismicity generated a release of ^{4}He from rock supporting the amount of ^{4}He that accumulated in the natural reservoirs since their formation (1.8–4.5 Ma). These results demonstrate that in tectonically active regions, the crustal ^{4}He degassing can episodically occur and powered as an advective process by seismogenetic processes. In fact, in the studied area the ^{4}He flux through the crust towards the atmosphere is higher than that due to a steady-state diffusive degassing and this excess can be due to the local seismicity. Considering the recognized link between rock deformation/fracturation and He degassing, the monitoring of the He flux in seismically active regions can potentially provide evidences of a modification of the field of stress due to the active tectonics, so the He can provides information to a better knowledge of the seismo-genetic processes at regional scale. However, our study shows that natural reservoirs accumulate deep sourced volatiles and the natural traps work as a sponge over time by absorbing the signal transferred towards the surface by the volatiles coming from deeper than the reservoirs, so these volatiles do not quickly reach Earth surface. These results well fit with the evidences that the increase of the activity from the mud volcanoes or vents because of earthquake is essentially post-seismic, in the sense that it occurs as a consequence of earthquakes and generally, no geochemical variations are recognized before. Finally, mud volcanoes are surely preferential sites for studying the relationships between fluids and seismicity, however for using He and other volatiles to investigate the genesis of earthquakes it is fundamental to have a model of fluids circulation and its storage into the crust together with an high frequency monitoring of the He that outgases at the surface. The seismogenesis is a dynamic process of ongoing rock deformation until to the fracturation, so even if fluids are directly involved in these processes nevertheless the effects of rock deformation can be also masked or reach the surface in delay.

The results reported in chapter II, indicate that the background seismicity during interseismic periods also controls the impulsive degassing of crustal ^4He. Therefore, coupling geochemical and geophysical long series of data, the crustal ^4He outputs can be used as an indicator of the expansion of the seismogenic process, thereby making it possible to assess the volumes of deformed rocks along the faults. Our study indicates that a high frequency He monitoring is fundamental to examine and calibrate regional models capable of describing the relationship between He degassing and seismogenic processes at depth. Therefore, as already highlighted in volcanic surveillance, our study emphasizes the need to use new, field deployable analytical solutions that can allow He data to be acquired (amounts and isotopic signature) with a frequency from weekly to daily. These new data could help to reconstruct the temporal evolution of natural processes such as volcanic eruption and earthquakes.

This Phd thesis highlights that a continuous, multidisciplinary, integrated monitoring approach that includes geochemical and geophysical observations can be the key to understanding the mechanisms underlying earthquake generation, and could facilitate to figure out premonitory rock deformation processes preceding the occurrence of a disastrous earthquake. Therefore, the novel results obtained in this study provide a new paradigm for studying the genesis of earthquakes and integrating multidisciplinary data for improving earthquake forecasts.

Finaly in the chapter III, using the catalogue of the ~2300 earthquakes that occurred during 2008–2019 in Irpinia fault zone (Caracausi et al 2022) and processing the data using Zmap7 tool in Matlab we may differentiate between shallow (2 - 4 km) and deeper (6 - 8 km) and more intense seismicity.

We notice how the most part (about the 20% of total seismicity) and most intense of seismic activity (up to M 4.4) is coincident with a top of dry pressurized reservoir in the brittle layer range, site of rock-CO_2 interaction, and large normal faulting earthquakes, like the 1980 M 6.9 Irpinia event, are driven by fluid amounts at the base of the active fault system (Improta et al 2014).

Shallow seismic activity constitutes about 10% of the total seismic activity, with intensities not exceeding M 3 and is coincident with the shallow-water carbonates reservoir where secondary precipitations and degassing process occur. Our study suggests that precipitation-based carbon sequestration is occurring right now, and that the process

is actively lubricating the fault and reducing powerful earthquakes in the creeping areas of the shallow seismogenic active faults.

In conclusion, an accurate study of rock-water-CO_2 interactions allows us to determine deep CO_2 of mantle origin as a possible source of the Contursi area manifestations (free and dissolved gases). Infact, due to the CO_2 dolomite/calcite-CO_2 mantellic fractionation, which, because of mass ratios in favour of dolomite/calcite even in the presence of short interaction times the CO_2 mantellic signature is completely or nearly masked by that of dolomite/carbonate. Later interaction of deep CO_2 with aqua or brine further modifies its signature, and through simple mixing and secondary processes of precipitation and degassing the system consequently evolves into the typical manifestations of the area, i.e., cold water, thermal and free gas.

The secondary effects of outgassing and/or precipitation can lead to an underestimation of the CO_2 fluxes outgassing from aquifers. This is a very important consequence for the CO_2 badget.

And last but not least, the secondary process occur in rocks-water-CO_2 interaction can act as powerful moderators of seismic activity by preventing the accumulation of gas and thus, the generation of overpressure